Exclusive π^- Electroproduction off the Neutron in Deuterium in the Resonance Region

by

Ye Tian

Bachelor of Science
Lanzhou University 2005

Master of Science
Lanzhou University 2008

Submitted in Partial Fulfillment of the Requirements

for the Degree of Doctor of Philosphy in

Physics

College of Arts and Sciences

University of South Carolina

2016

Accepted by:

Ralf Gothe, Major Professor

Yordanka Ilieva, Committee Member

Kijun Park, Committee Member

Matthias Schindler, Committee Member

Cheryl L. Addy, Vice Provost and Dean of the Graduate School

Dedication

To my grandparents Yonggen Tian and Baozhi Yin, as well as my parents Xiaogang Tian and Zhi Li.

Acknowledgments

First of all, I wish to express my sincere gratitude to my advisor, Prof. Ralf Gothe, without whose guidance this dissertation would never have been possible. He has always been extremely helpful and encouraging. His patience, motivation, and immense knowledge influenced every aspect of my PhD study. Beside, he always helped me to improve my English skills whenever he got a chance. I could not have imagined having a better advisor and mentor for my PhD study.

I would also like to thank the other members of my PhD committee, Yordanka Ilieva, Matthias Schindler, and Kijun Park, for their great help with my PhD research and job search. Also a special thanks goes to Viktor Mokeev, for offering a lot of advice on my research and help with my job search.

My sincere thanks also goes to my former and present peers and colleagues. Evan Phelps showed me how to use "ROOT" to analyze data and also helped me to debug my codes despite his busy schedule. Arjun Trivedi worked together with me along this amazing trip. His encouragement and help gave me a lot of strength. Gleb Fedotov guided me through the complex and confusing simulation, cooking and analysis related software. Zhiwen Zhao and Haiyun Lu helped me make a smooth transition at the beginning of my PhD study and offered me many useful information for my job search. Iuliia Skorodumina, Gary Hollis, Nick Tyler, and Chris McLauchlin carefully read an early draft of this dissertation and offered me a lot of helpful and constructive suggestions.

I would like to thank my parents Zhi Li and Xiaogang Tian, my grandparents, and my parents in-law for their strong backup and continuous support, especially for

taking care of my daughter Melody. I also want to thank my friends Tongtong Cao, Yajie Ni, Jing Li, Hongyue Duyang, Manlai Liang, and Shu Yan, for their friendship and support.

Last but not the least, I cannot express how grateful I am to my husband Honghai Xu for his continuous encouragement and unconditional support and help, without which I would not have completed my PhD study successfully.

Abstract

This dissertation focuses on extracting the exclusive $\gamma^* n(p) \rightarrow p\pi^-(p)$ reaction cross section from deuterium data. The existing $\gamma^* n \rightarrow p\pi^-$ event generator is modified to include the spectator (proton) information based on the CD-Bonn potential [28] to simulate the real data process. With this method, the exclusive quasi-free process is isolated successfully as demonstrated by the comparison of the spectator momentum distribution of the simulation with the missing momentum distribution of the data, and the kinematical final-state-interaction contribution factor R_{FSI} is extracted directly from the data according to the ratio between the exclusive quasi-free and full cross sections. The results of this dissertation are new the exclusive and quasi-free cross sections off neutrons bound in deuterium. Furthermore, the corresponding structure functions are extracted from those cross sections as well. The experiment was done in Hall B at the Thomas Jefferson National Laboratory (JLab) by using the CEBAF Large Acceptance Spectrometer (CLAS) detector, the "e1e" run data off a liquid deuterium target will provide these final results with a kinematic coverage for the hadronic invariant mass (W) up to 1.9 GeV and in the momentum transfer (Q^2) range of $0.4 - 1.0$ GeV/c^2.

Table of Contents

List of Tables

List of Figures

Chapter 1

Introduction and Overview

What's the origin of more than 98% of the visible mass - that's everything in the universe, we sense and see around us? Visible matter is everything made of atoms, which get their mass mainly from the atomic nucleus. The nuclei of atoms are composed of nucleons, namely protons and neutrons. The proton and neutron, each made of three valence quarks, are much more massive than the sum of their constituents. Where does all this "extra" mass come from? In order to answer this question, we have to understand how the quarks interact via the exchange of gluons, how quarks bind together via strong interaction, and how gluons interact with each other. The fundamental theory of the strong interaction is Quantum Chromodynamics (QCD), which is very successful at predicting reactions with large momentum transfer, Q^2, within the perturbative regime with current quarks and gauge gluons as the fundamental degrees of freedom. However when Q^2 drops down to the non-perturbative regime, there is a transition to completely different degrees of freedom, the dressed quarks and gluons as well as the mesons and nucleons, which prevents us from having a direct QCD description of the phenomena corresponding to hadronic physics, such as the structure of the nucleon and its excitations (N^*).

The most fundamental approach to resolve this difficulty is to develop accurate numerical simulations of QCD on to a four-dimensional Euclidean space-time lattice (LQCD) [35], which is the only way to rigorously test QCD at present. LQCD makes significant progress on calculating some basic properties of baryons, such as masses of ground states [43], as well as low lying exited states [45], however it faces several

challenging issues. Therefore, it is equally important to develop other complementary nonperturbative methods based on the QCD approach to interpret the real world properties, and the Dyson-Schwinger equations (DSEs) are such an approach. It is based on infinite tower of coupled integral equations [60], which is discussed later. Alternatively, hadron models with effective degrees of freedom have been constructed to interpret data, such as constituent quark models [20], MIT-bag models [36], and Nambu-Jona-Lasinio (NJL) models [41].

All these non-perturbative approaches need experimental data to test and improve their predictions. Therefore we need to accumulate sufficient and precise data on meson electroproduction reactions to pin down the distance-dependent structure of the nucleon and its excitations, in order to push the development of quark models and QCD-based calculations forward. Due to the short lifetimes of Ns^*, it is impossible to observe these excitation states directly. In the experiment, we can study Ns^* via products of their decays. There are a couple ways to study Ns^* production, i.e., electroproduction and photoproduction of pseudo-scalar or vector mesons. The electromagnetic vertex of the meson electroproduction is well described by Quantum Electrodynamics (QED), while the hadron scattering governed by the strong interaction is the only unknown part in the electroproduction process. Furthermore, the virtual photon exchange of the electroproduciton allows us to study hadronic properties at different Q^2 regimes, which is crucial in understanding of the internal dynamics of the strong interaction in the non-perturbative regime. In reactions of meson electroproduction off nucleons, we are interested in the resonance processes, in which a virtual photon excites the nucleon to its excitated state (N^*), with then decays to one meson or more and nucleon. Beside this, the non-resonance processes in this reaction are treated as background in the reaction models to extract the resonance information.

In addition, the vast majority of the available experimental data are meson elec-

troproduction off the proton in the hydrogen target. Hence flavor-dependent analyses of excited light-quark baryons are lacking experimental data off the neutron, which is due to the fact that there is no free neutron target. Deuterium becomes to be one of the best alternate targets for neutrons, whose nucleus consists of one proton and one neutron, because it is the simplest and most loosely bound system of neutron. However, due to the neutron being bound in the deuteron, a few effects must be studied in order to extract the neutron information, such as, Fermi motion, off-shell effects, and final state interactions (FSI). The goal of this work is to provide the exclusive and quasi-free $\gamma^* n(p) \to p\pi^-(p)$ reaction cross sections from deuterium target, as well as kinematical FSI contribution factor R_{FSI} that can be determined from the data itself. This thesis work concentrates on the study of the bound neutron resonance via meson electroproduction, which will improve our knowledge of the Q^2 evolution of the resonance states off the bound nucleon system and aid our understanding of the structure and interaction of hadrons.

1.1 QCD and Non-Perturbative Approaches

QCD

QCD describes the interaction between quarks and gluons, which we believe are the fundamental degrees of freedom that make up hadronic matter. Quarks are one type of fundamental particles, it means that they are not composed of any other particles. There are six known, electrically-charged, different-flavored quarks, which are listed in the Tab. 1.1. Each quark has its own antiquark.

Quarks interact with each other only through intermediate agents "gluons", which are the exchange particles that couple to the color charge in QCD. This is analogous to the electromagnetic interaction in which photons are exchanged between electrically charged particles. Similar to photons, gluons are massless, spin-1 particles. The

Table 1.1: Summary of quark properties.

Name	Symbol	Charge	Isospin (I_3)	Mass (MeV/c^2)
Up	u	$+2/3$	$+1/2$	2.3 ± 1.2
Down	d	$-1/3$	$-1/2$	4.8 ± 0.8
Charm	c	$+2/3$	0	1275 ± 25
Strange	s	$-1/3$	0	95 ± 5
Top	t	$+2/3$	0	173210 ± 510
Bottom	b	$-1/3$	0	4180 ± 30

gluons simultaneously carry color and anticolor charge. Since gluons are vectors in the adjoint representation of color gauge group SU(3), there are eight gluons. By their exchange the eight gluons mediate the interaction between particles carrying color charge, i.e., not only the quarks but also the gluons themselves. This is an important difference to QED, where the electromagnetic field quanta have no charge, and therefore cannot couple at lowest order with each other. The elementary processes of QCD include emission and absorption of gluons (Fig. 1.1(a)); production and annihilation of quark-antiquark pairs (Fig. 1.1(b)); and coupling three or four gluons to each other (Fig. 1.1(c) and (d)). QCD is a non-abelian gauge theory whose

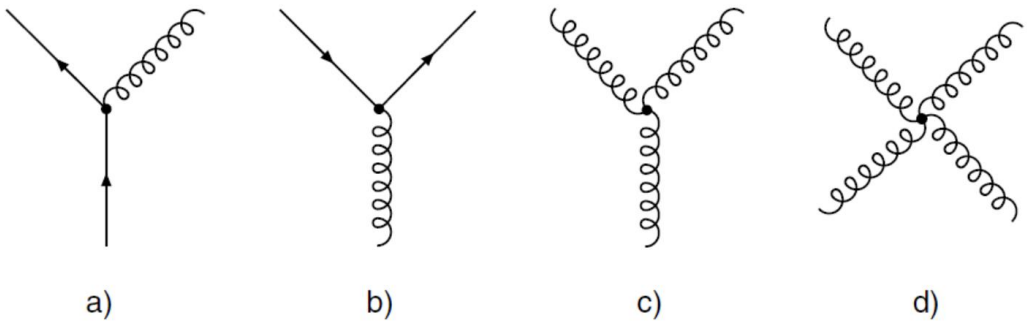

Figure 1.1: The fundamental interaction diagrams of QCD [56]: (a) emission of a gluon by a quark, (b) splitting of a gluon into a quark-antiquark pair, (c) and (d) self-coupling of gluons.

dynamics are governed by the Lagrangian [52], which is represented by

$$\mathcal{L}_{QCD} = \sum_q \bar{\psi}_{q,a}(i\gamma^\mu \partial_\mu \delta_{ab} - m_q \delta_{ab})\psi_{q,b} - \sum_q \bar{\psi}_{q,a} g_s \gamma^\mu t^C_{ab} A^C_\mu \psi_{q,b} - \frac{1}{4} F^A_{\mu\nu} F^{A\mu\nu}, \quad (1.1)$$

where γ^μ are the Dirac γ matrices. The $\psi_{q,a}$ are quark-field spinors for a quark of flavor q and mass m_q, with a color-index a ($a = 1$ to 3, quarks have three "colors"). A^C_μ correspond to the gluon fields, with C running from 1 to 8 (there are 8 kinds of gluons). Furthermore, t^C_{ab} ($t^C_{ab} \equiv \lambda^C_{ab}/2$) are eight 3×3 matrices that are the generators of the $SU(3)$ group. The field tensor $F^A_{\mu\nu}$ is given by

$$F^A_{\mu\nu} = \partial_\mu A^A_\nu - \partial_\nu A^A_\mu - g_s f_{ABC} A^B_\mu A^C_\nu, \tag{1.2}$$

where the f_{ABC} are the structure constants of the $SU(3)$ group, and g_s is the QCD coupling constant calculated by

$$\alpha_s(Q) = g_s^2/4\pi, \tag{1.3}$$

$$\alpha_s(Q) = \frac{2\pi}{\beta_0 ln(Q/\Lambda_{QCD})}, \tag{1.4}$$

$$\beta_0 = 11 - \frac{2}{3}n_f, \tag{1.5}$$

where n_f is the number of quark flavors that are involved in the process, and Λ_{QCD} is the fundamental cut-off parameter of QCD, whose value is experimentally determined as $\Lambda_{QCD} \sim 200$ MeV/c [56].

The first term in the Eq.(1.1) represents the part of the free quark fields, the second term corresponds to the quark-gluon interactions (Fig. 1.1(a) and (b)). The quark interacts with gluons is in a way similar to the electrons interacting with photons in QED. Gluons are physical degrees of freedom and therefore must carry energy and momentum themselves. Thus the third term in the Lagrangian is needed to describe gluon self-interactions. Since gluons carry color charges, their self-interactions are responsible for many of the unique and important features of QCD, such as asymptotic freedom, color confinement, and chiral symmetry breaking [50].

The second term in Eq. (1.5), $-\frac{2}{3}n_f$, comes from quark-antiquark pair screening. However, the first term, 11, has the opposite sign and comes from the non-linear

gluon-gluon vertices (Fig. 1.1). Thus the gluons self-coupling causes a color anti-screening effect.

Three important characteristic QCD features are listed as following

- Asymptotic freedom: From Eq. (1.4), this Q-dependence of the coupling strength corresponds to the dependence on separation. For very high Q values (very small distance), the interquark coupling decreases, vanishing asymptotically. In the limit $Q \to \infty$, quarks can be considered as "free", this is called asymptotic freedom.

- Confinement: In the very low energy domain (very large distance), the interquark coupling increases so strongly that it is impossible to detach individual quarks from hadrons (confinement) [56]. Although the confinement hypothesis has not been directly derived from QCD.

- Dynamical chiral symmetry breaking: Contrary to confinement, we are able to understand it better even though it is an other typical low-energy feature of QCD. Since in the low-energy domain of QCD, the proton is composed of three valence quarks: two up quarks with $m_u \sim 2.3$ MeV and one down quark with $m_d \sim 4.8$ MeV, only contributing about 9.4 MeV to the rest mass of the proton (938 MeV). It turns out that chiral symmetry is realized in this regime. The source of the bulk of the proton's mass is QDC binding energy, which arises from QDC dynamical chiral symmetry breaking [57], and an effective quark mass is generated [36].

Lattice QCD (LQCD)

LQCD is QCD solved on a discrete four dimensional Euclidean space-time lattice with spacing a, with quark fields placed on sites and gauge fields on links between sites. The spacing a plays the role of the ultraviolet regulator, rendering the quan-

tum field theory finite [52]. When $a \to 0$, the continuum theory is recovered. LQCD is defined by allowing the numerical evaluation of the path integral, which is based on a non-perturbation calculation. Progress in LQCD has required a combination of improvements in formulation, numerical techniques, and in computer technology, allowing these simulations to calculate correlation. The practical calculation results of LQCD come with both statistical and systematic errors due to the limitation of the efficiency of algorithms and the availability of computational resources. The statistical errors correspond to the use of Monte-Carlo integration, the systematic errors come from using non-zero values of a. Since LQCD is a regularization of QCD, the only tunable input parameters for lattice calculation are the strong coupling constant α_s and the quark masses for each flavor, which are determined using experimental inputs. In this way, if QCD is the correct theory of strong interactions, all predictions of LQCD have to agree with experimental data, and the nucleon and pion structure from lattice QCD simulations by using a physical pion mass is achieved [13].

Dyson-Schwinger Equations (DSE)

The DSEs are coupled infinitely tower integral equations, which are a general relationship between Green's functions in quantum field theories (QFT) [60]. Solving these equations provides a solution of QDC. The DSEs include the Bethe-Salpeter equation (BSE) which is a tool to calculate the properties of relativistic two-body scattering and bound states. For studies based on DSEs, it is unavoidable to deal with the infinite tower of coupled integral equations. For practical purposes, the current approach of DSEs truncates the tower at some point. This means that the tower of integral equations must be limited to some n, where n is the maximum number of legs on any Green's function included in the self-consistent solution of the equations [60]. An Ansatz can then be introduced for the omitted terms. There is hope to use the lattice gauge theory simulations to provide additional insight into the form

of these truncated functions. One approach of studying the non-preturbative properties of hadrons is the combination of DSEs and Bethe-Salpeter equations (BSE). There are some calculations related to this approach, which were performed upon truncating the (anti)quark-quark interaction to a single gluon exchange, so-called Rainbow-Ladder truncation [62]. Based on that, the details of recent studies on meson spectra have been published in Refs. [31] [32] [38]. Baryons have been studied in the quark-diquark approximation [63]. Current interest of DSEs and BSE combination approach is the inclusion of interaction mechanisms beyond the leading term [62], and in the extension to glueball [61] and tetraquark bound-states [37].

1.2 Single-Pion Electroproduction off the Moving Neutron

Single-pion electroproduction has been the main process in the study of the $N - N^*$ transition form factors of the lower mass nucleon resonances such as $P_{33}(1232)$, $P_{11}1440$, $D_{13}(1520)$, $S_{11}(1535)$, $S_{11}(1650)$, $F_{15}(1680)$, and $D_{33}(1700)$.

Data Status

The low-lying excited states of the proton have been studied in greater detail [19], there is still very little data available on neutron excitations. Because of the inherent difficulty in obtaining a free neutron target, a deuterium target is the best alternative. From the SAID database [4], the π^- electroproductions off neutrons in the deuterium are listed in the Tab. 1.2, in which, the ratio R_{π^-/π^+} was directly measured for most available data. Even though the differential cross sections were measured directly, they are only available for single or couple Q^2 values and in parts of the whole resonance range. We need to accumulate sufficient and precise data for the neutron, not only to study the isospin dependent structure of the nucleon and its excitations, but also to aid the development of QCD based calculations and models.

Table 1.2: Summary of the single pion electronproduction off bound neutron in the deuterium target with $R_{\pi^-/\pi^+} = \frac{d\sigma(\gamma_\nu+n\to\pi^-+p)}{d\sigma(\gamma_\nu+p\to\pi^++n)} = \frac{Rate(e+d\to e+\pi^-+p(p))}{Rate(e+d\to e+\pi^++n(n))}$.

Reaction	Observable	W value GeV	Q^2 value GeV^2	Lab/experiment
$en(p) \to e'\pi^-p(p)$ $ep(n) \to e'\pi^+n(n)$	R_{π^-/π^+}	2.15, 3.11	1.2, 4.0	Cornell/WSL [17]
$en(p) \to e'\pi^-p(p)$ $ep(n) \to e'\pi^+n(n)$	$d\sigma/d\Omega_\pi$	2.15, 2.65	1.2, 2.0	Cornell/WSL [18]
$en(p) \to e'\pi^-p(p)$ $ep(n) \to e'\pi^+n(n)$	R_{π^-/π^+}	1.28-1.71	0.5	NINA [64]
$en(p) \to e'\pi^-p(p)$ $ep(n) \to e'\pi^+n(n)$	R_{π^-/π^+}	1.3-1.7	1.0	NINA [49]
$ep(n) \to e'\pi^+n(n)$ $en(p) \to e'\pi^-p(p)$	R_{π^+/π^-}	1.16, 1.232	0.0856, 0.0656	ALS [34]
$en(p) \to e'p\pi^-(p)$	σ_L, σ_T	1.15, 1.6	0.4	JLab-HallA [33]
$en(p) \to e'p\pi^-(p)$	σ_L, σ_T	1.95, 2.45	0.6, 1.0, 1.6, 2.45	JLab-HallC [39]

The six simplest pion electroproduction reactions off the free proton, bound proton, and bound neutron targets are summarized as

$$\gamma^* + p \to \pi^0 + p, \tag{1.6}$$

$$\gamma^* + p \to \pi^+ + n, \tag{1.7}$$

$$\gamma^* + D(p) \to \pi^+ + n + n_s, \tag{1.8}$$

$$\gamma^* + D(p) \to \pi^0 + p + n_s, \tag{1.9}$$

$$\gamma^* + D(n) \to \pi^- + p + p_s, \ and \tag{1.10}$$

$$\gamma^* + D(n) \to \pi^0 + n + p_s. \tag{1.11}$$

All the listed single-pion reactions under the same experimental conditions are included in the "e1e" run, which took data with the CLAS detector at JLab from December 14th, 2002 to January 24th, 2003. The combined analysis of processes Eq. (1.6)- (1.10) will provide the best possible experimental information about the final state interactions and the off shell effects of the bound nucleon, which are crucial to extract the free neutron information. In this thesis, the process Eq. (1.10) is

analyzed, which includes both resonance and non-resonance process, to extract corresponding cross sections off the neutron in the deuterium target in the resonance region. The resonance process of interest Eq. (1.10) is shown in Fig. 1.2, where the electron emits a virtual photon (γ^*) exciting the neutron to one of its excitations (N^*), then the resonance decays to a π^- and a proton (p). The initial proton in the deuteron is treated as a spectator (P_s), which will be discussed in Chapter 3 that discusses how to isolate the quasi-free process.

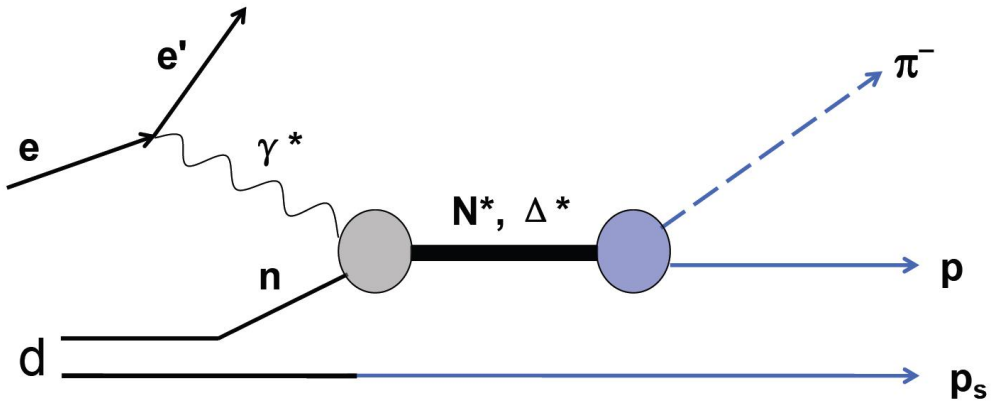

Figure 1.2: The resonance process of single-pion electroproduction off a neutron in deuterium. The initial proton in the deuteron is treated as the spectator, named as P_s.

Kinematic

Before we introduce the kinematics of the scattering from a bound neutron in a deuteron, we first consider the case of scattering from a free neutron that is at rest in the lab frame, then the chosen variables W_i and Q^2 are defined as:

$$W_i^{rest} = \sqrt{(q^\mu + n^\mu)^2} = \sqrt{(p^\mu + (\pi^-)^\mu)^2} = W_f^{rest}, \tag{1.12}$$

$$(Q^{rest})^2 = -(q^\mu)^2 = (e^\mu - e^{\mu'})^2 \, , \tag{1.13}$$

where q^μ presents the four momentum of the virtual photon. W_i^{rest} and $(Q^{rest})^2$ correspond to the invariant mass of the photon-nucleon system and the four-momentum

transfer of the virtual photon for this scattering respectively, which are determined in the leptonic interaction plane that is shown in Fig. 1.6 with the gray color. In addition, we also need to determine two body final state p^μ and $(\pi^-)^\mu$. In general, two final particles need to be described by $4 \times 2 = 8$ components of their four vector momentum. Indeed, with the knowledge that they are all on mass shell, it gives two restrictions ($E_j^2 - k_j^2 = m_j^2; j = 1, 2$). Furthermore, the energy momentum conservation laws impose four additional constraints for four momentum components of the final particles. So we only need two kinematics variables to determine the hadronic two body final state. Eventually, we end up with four variables to represent the $\gamma^* n(p) \to p\pi^-(p)$ cross section.

For the kinematics of the process Eq. (1.10) that is the scattering from a bound neutron in a deuteron, we have to consider the influence on the final cross sections of Fermi motion, off-shell effects, and the final state interaction, which are introduced next.

The Fermi Motion

In the process Eq. (1.10), where the initial neutron is moving around "quasi-freely" in the deuteron in the lab frame. By measuring all final particles $e^{'}$, p, and π^- exclusively, energy and momentum conservation imply that the sums of the four-momenta before and after the reaction are identical:

$$\begin{aligned} q^\mu + D^\mu &= (\pi^-)^\mu + p^\mu + p_s^\mu \ , \\ q^\mu + p_i^\mu + n^\mu &= (\pi^-)^\mu + p^\mu + p_s^\mu \ , \end{aligned} \tag{1.14}$$

where D^μ is the four-momentum of deuteron that is at rest in the lab frame, $D^\mu = (0, m_D)$. n^μ and p_i^μ correspond to the four-momentum of the neutron and the proton, respectively, that are moving and loosely bound in the deuteron in that frame. The outgoing missing proton p_s^μ, which is not directly measured, is reconstructed from the

Eq. (1.14) by

$$p_s^\mu = q^\mu + D^\mu - (\pi^-)^\mu - p^\mu, \tag{1.15}$$

and the momentum of this proton is calculated by

$$\vec{P}_s = \vec{q} - \vec{\pi^-} - \vec{p}. \tag{1.16}$$

Ignoring the off-shell effects at this moment, we focus on the motion first. In the quasi-free process of the reaction Eq. (1.10), where the initial proton is treated as a "spectator" that is totally unaffected by the interaction, thus $p_i^\mu = p_s^\mu$ in Eq. (1.14) (ignoring the off-shell effects). Then we can rewrite the Eq. (1.14) by

$$q^\mu + n^\mu = (\pi^-)^\mu + p^\mu \ , \tag{1.17}$$

and the initial neutron momentum is reconstructed by

$$\vec{n} = \vec{\pi^-} + \vec{p} - \vec{q}. \tag{1.18}$$

For the quasi-free process, by comparing Eq. 1.16 with Eq. 1.18, we get

$$\vec{P}_s = \vec{p_i} = -\vec{n}. \tag{1.19}$$

In contrast to the free neutron case, the neutron is now moving around with the Fermi momentum, which is reconstructed from Eq. (1.18) and graphed in Fig. 1.3. This motion causes changes in the kinematics compared to scattering off a neutron at rest in the lab frame. Thus, in order to define the proper electron scattering plane, we first boost e^μ, $(e^{'})^\mu$, p^μ, and $(\pi^-)^\mu$ from the lab frame into the neutron rest frame with the boost vector calculated from n^μ (Eq. (1.17)). In this frame, the variables W_i, W_f and Q^2 are calculated from Eq. (1.12) and Eq. (1.13), as well as the electron scattering plane is defined. Then W_f and Q^2 are selected to represent the scattering cross sections off the moving neutron in the deuteron. So for this work, the final reported cross sections are not influenced by the Fermi momentum of the initial neutron in the deuteron.

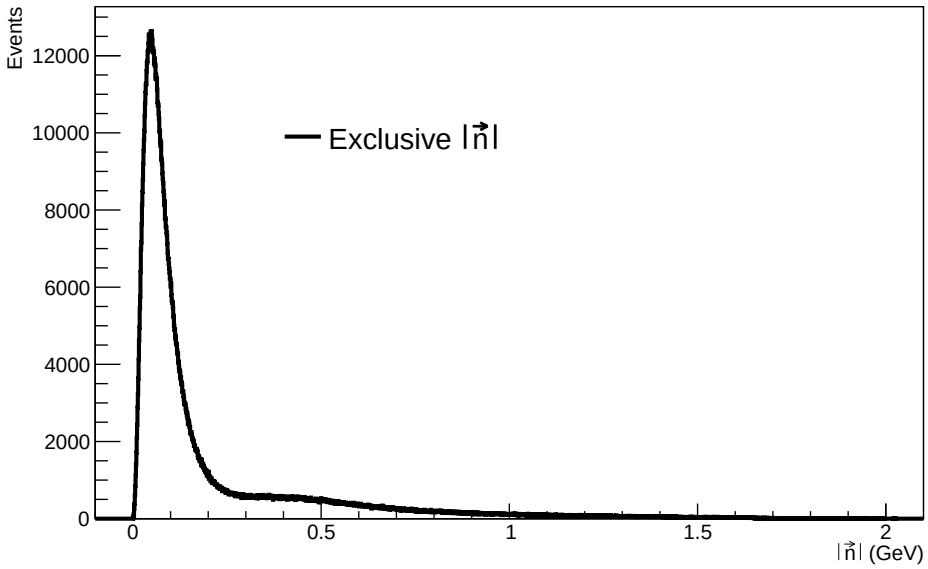

Figure 1.3: The momentum distribution of initial neutron in the exclusive $\gamma^* n\,(p) \to p\pi^-\,(p)$ process, which is moving in the deuteron in the lab frame.

Off-shell Effects

As mentioned previously, the bound neutron is also off-shell beside moving around in the deuteron. Even in the quasi-free process (isolating the quasi-free process is discussed in the Chapter 3), p_i^μ is not equal to p_s^μ due to the fact that the initial proton p_i is off-shell and outgoing "spectator" proton p_s is on-shell in the reaction Eq. (1.10). However the relation $\vec{p_i} = \vec{p_s} = -\vec{n}$ is not influence by the off-shell effects in the quasi-free process. So we can reconstruct the off-shell neutron four momentum by $n^\mu = (-\vec{P}_s, M_n)$ and $E_n = \sqrt{(-\vec{P}_s)^2 + (M_n)^2}$. So it is better to choose W_f, which is well defined and measured directly from p and π^-, rather than W_i, to present the final cross section. In the "spectator" situation, in order to conserve energy and momentum in the scattering process, we have set

$$M_n = m_n - 2\frac{k_n^2}{2m_n} - 2\text{MeV}, \tag{1.20}$$

reestablishing $W_i = W_f$. This can be seen in Fig. 1.4, where W_f is calculated by Eq. (1.12) and radiative corrected W_i is calculated by setting E_n with Eq. (1.20),

which are presented by the black and red lines separately, and their peaks match each other. For other possible M_n settings, we get shifted or smeared W_i distributions (radiative corrected) compared to W_f. The boost vector (from the lab frame to the CM frame) is calculated using the different W_i and W_f, then the influence of those different boosts on the final cross section can be quantified. The result shows that these effects on the final cross sections are marginal and are accounted for as a source of systematic uncertainties described in Chapter 4.

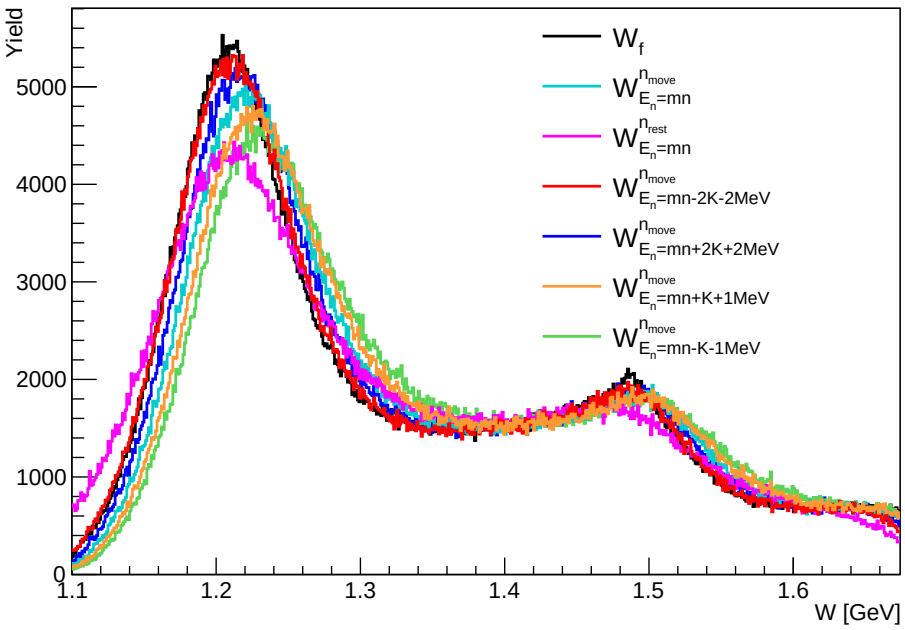

Figure 1.4: (Color online) The comparison of W distributions. Black line presents W_f, blue line shows W_i calculated by setting $n^\mu = (-\vec{P}_s, E_n)$ (E_n with Eq. (1.20)). The other colors present the W_i distribution by setting n_μ to $(-\vec{P}_s, m_n)$ (cyan), $(0, m_n)$ (magenta), $(-\vec{P}_s, m_n + 2\frac{k_n^2}{2m_n} + 2\text{MeV})$ (blue), $(-\vec{P}_s, m_n + \frac{k_n^2}{2m_n} + 1\text{MeV})$ (orange), and $(-\vec{P}_s, m_n - \frac{k_n^2}{2m_n} - 1\text{MeV})$ (green).

The Final State Interaction (FSI)

In the reaction process Eq. (1.10), which is shown in Fig. 1.5 (a), with a $|\vec{P}_s|< 200$ MeV cut, the quasi-free process is the dominant process (see Chapter 3). However in

the resonance process, it is possible to have final state interactions, such as pp re-scattering and $p\pi$ re-scattering shown in Fig. 1.5 (b) and (c) respectively. It corresponds to the situation in which the outgoing proton or π^- interacts with the spectator proton (P_s). Thus, the four momentum of the final state particles are changed due to these final state interactions. After isolating the quasi-free process, the kinematical FSI contribution factor R_{FSI} will be extracted from the data itself, and the details will be discussed in the Chapter 6. It is also possible to have other kinds of FSI, i.e. in the process Eq. (1.9) or (1.10), it is possible to have $\pi^0 + n_s \rightarrow \pi^- + p$ and $\pi^- + p_s \rightarrow \pi^0 + n$ final state interactions in these processes, which can increase or decrease the final state π^- and p production. If we want to quantify the contribution of this kind of FSI from the data itself, a combined analysis of pion electroproduction off the free proton, the bound proton, and the bound neutron in the "e1e" run is needed. In this thesis, this kind of final state interactions are not quantified from the data itself.

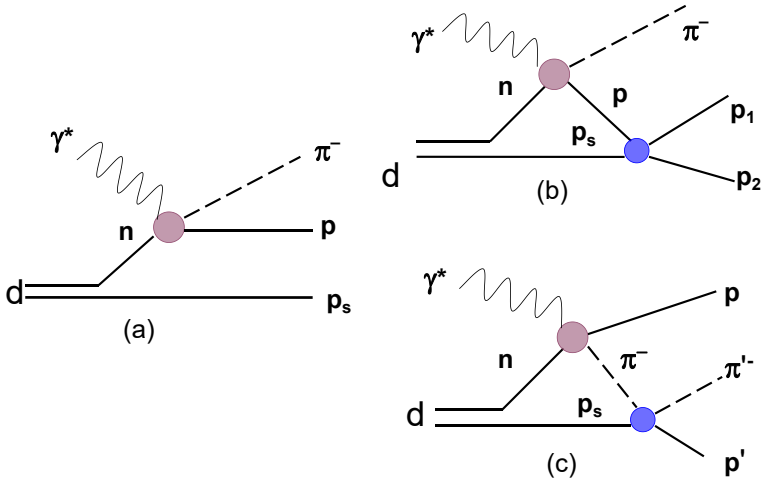

Figure 1.5: Kinematic sketch as in the text for the three leading terms in $\gamma^* + D \rightarrow \pi^- + p + p$ process (a) quasi-free, (b) pp re-scattering, and (c) pπ^- re-scattering. Diagrams (b) and (c) are two main sources of kinematical final state interactions.

Boosting of the Kinematic Variables

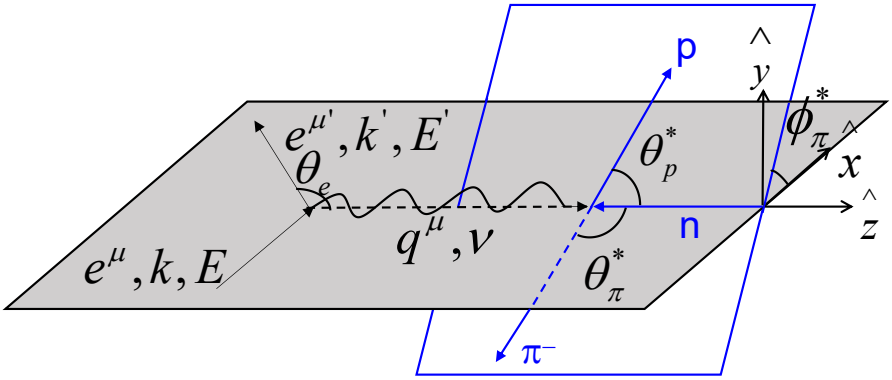

Figure 1.6: Kinematics of π^- electroproducton off a moving neutron. The leptonic neutron rest frame plane is formed by e^μ and $e^{\mu'}$, where k, E, k', and E' are corresponding momentum and energy of the incoming and outgoing electrons. q^μ is the virtual photon four momentum and ν is the transfered energy. The hadronic CM frame plane is determined by final particles p and π, here θ^*_p and θ^*_π are their polar angles and ϕ^*_π the azimuthal angle of π^-.

In order to get the correct variables to present the final cross sections of π^- electroproduction off the neutron in the deuterium target, we boost first all particles' four momenta from the lab frame (deuterium at rest) into the neutron at rest frame with the boost vector $\vec{\beta_1} = -\vec{n}/E_n$, where $\vec{n}$ and E_n are calculated from n^μ (Eq. (1.17)). Then the invariant mass W_f and the momentum transfer Q^2 are calculated by the Eq. (1.12) and (1.13) in this frame. In addition, by setting the coordinates in this frame, $\hat{z}_{nrest}$ parallel to the virtual photon direction and $\hat{y}_{nrest}$ perpendicular to the electron scattering plane, we ensure that $\hat{x}_{nrest}$ is staying in the electron scattering plane and is set to be $\hat{x}$ direction in the final coordinate system. Secondly, we directly boost all particles' four momenta from the lab frame into the CM frame with the boost vector $\vec{\beta_2} = -(\vec{p} + \vec{\pi^-})/(E_p + E_{\pi^-})$, then set the $\hat{z}_{CM}$ parallel to the virtual photon direction in this frame. Since the $\hat{z}_{nrest}$ is not as well defined due to off-shell

effects, it is better to set the final $\hat{z}$ parallel to $\hat{z}_{CM}$. The X and Y projections of the $\hat{z}_{nrest}$ in the CM frame are plotted against each other for final-state-interaction dominated events and quasi-free events, which are shown in Fig. 1.8 and 1.7, respectively. It turns out that the spread of these distributions around zero correspond to the angle difference between $\hat{z}_{nrest}$ and $\hat{z}_{CM}$, which are 5.4° for final-state-interaction dominated events in the exclusive process and $< 1°$ for quasi-free events. Although the final-state-interaction dominated events show significant spread, this coordinate choice is the best way to present the quasi-free results for the bound neutron data. The $\cos\theta^*_{\pi^-}$ and $\phi^*_{\pi^-}$ are calculated ultimately in the CM frame. In summary, the coordinates are set by:

$$\begin{aligned} &\hat{z} = \frac{\vec{q^*}}{|\vec{q^*}|}, \text{ CM frame} \\ &\hat{x} \text{ is in the } \vec{k}, \vec{k'} \text{ plane of the n rest frame and perpendicular to } \hat{z}, \text{and,} \\ &\hat{y} = \hat{z} \times \hat{x}, \end{aligned} \tag{1.21}$$

which are shown in Fig. 1.6.

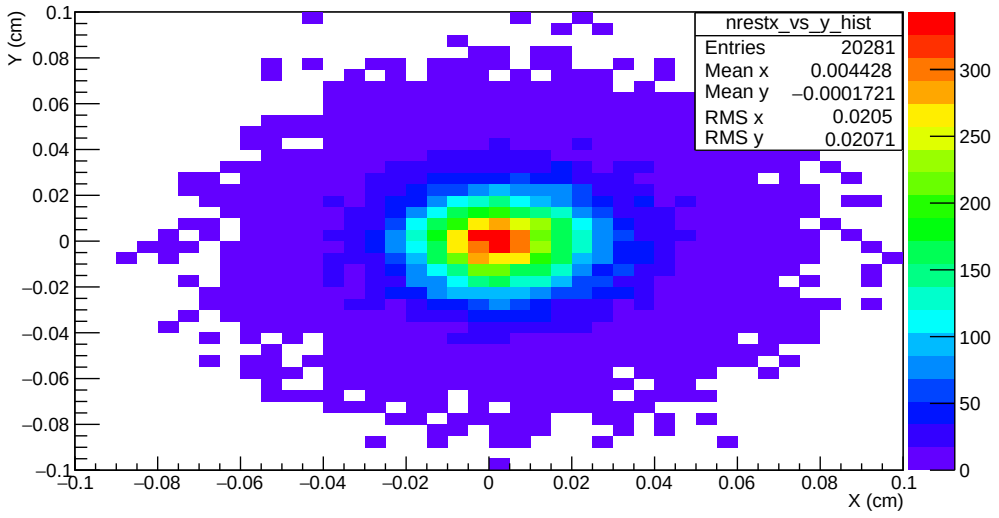

Figure 1.7: The X and Y projections of the $\hat{z}_{nrest}$ in the CM frame are plotted against each other for exclusive quasi-free events.

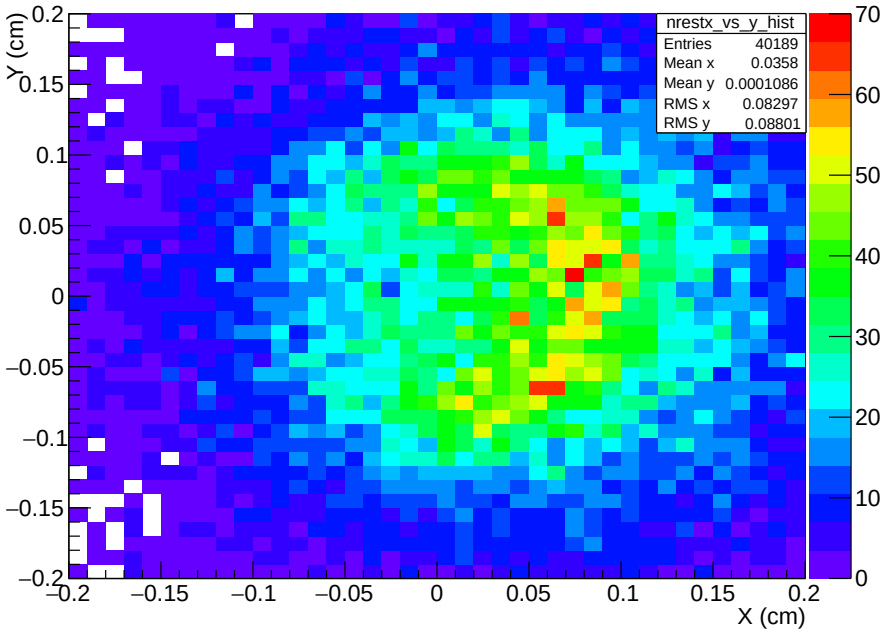

Figure 1.8: The X and Y projections of the $\hat{z}_{nrest}$ in the CM frame are plotted against each other for final-state-interaction dominated events.

Formalism

The cross section for the exclusive $\gamma^* n \rightarrow p\pi^-$ reaction with unpolarized electron beam and unpolarized free neutron target is given by

$$\frac{d^5\sigma}{dE' d\Omega^*_{\pi^-} d\Omega_{e'}} = \Gamma_v \left(E', \Omega_{e'}\right) \frac{d\sigma}{d\Omega^*_{\pi^-}}. \tag{1.22}$$

Where the virtual photon flux that depends on the matrix elements of the leptonic interaction is calculated by

$$\Gamma_v \left(E', \Omega_{e'}\right) = \frac{\alpha}{2\pi^2} \frac{E'}{E} \frac{K_\gamma}{(1-\epsilon)\, Q^2}. \tag{1.23}$$

Here $\alpha = 1/137$ represents the electromagnetic coupling constant, ϵ corresponds to the transverse polarization of the virtual photon,

$$\epsilon = \left(1 + 2\left(\frac{|\vec{q}|^2}{Q^2}\right) tan^2 \frac{\theta_e}{2}\right)^{-1}, \tag{1.24}$$

and the photon equivalent energy is calculated by

$$K_\gamma = \frac{W^2 - M_n^2}{2M_n}. \tag{1.25}$$

In these equations "$*$" denotes that the variable is calculated in the CM frame, all others are in the neutron at rest frame. Moreover, E is the initial coming electron energy, $E^{'}$ and θ_e are outgoing election energy and scattering angle. $\Omega_{e^{'}}$ and Ω_{π^-} correspond to the solid angles of outgoing electron and π^-. If we want to represent the cross sections in W and Q^2 bins, the Jacobian factor needs to be applied for the variables transformation $(E^{'}, \Omega_{e^{'}}) \rightarrow (W, Q^2)$

$$\frac{d^4\sigma}{dW\,dQ^2 d\Omega^*_{\pi^-}} = \frac{1}{J\left(W,Q^2\right)} \frac{d^4\sigma}{dE_{e^{'}} d\Omega^*_{\pi^-} d\Omega_{e^{'}}} = \frac{\Gamma_\upsilon\left(E_{e^{'}}, \Omega_{e^{'}}\right)}{J\left(W,Q^2\right)} \frac{d\sigma}{d\Omega^*_{\pi^-}} = \Gamma_\upsilon\left(W,Q^2\right) \frac{d\sigma}{d\Omega^*_{\pi^-}}. \tag{1.26}$$

The invariant mass W and virtual photon momentum transferred Q^2 are calculated by the following equations:

$$W = \sqrt{Q^2 + M_n^2 + 2M_n\left(E - E^{'}\right)}, \tag{1.27}$$

$$Q^2 \simeq 4EE^{'} sin^2\frac{\theta_e}{2} = 2EE^{'}\left(1 - \cos\theta_e\right)\ . \tag{1.28}$$

The Jacobian factor is defined by

$$\begin{aligned} J\left(W,Q^2\right) &= \begin{vmatrix} \frac{\partial W}{\partial E^{'}} & \frac{\partial W}{\partial \Omega_{e^{'}}} \\ \frac{\partial Q^2}{\partial E^{'}} & \frac{\partial Q^2}{\partial \Omega_{e^{'}}} \end{vmatrix} = \frac{1}{2\pi} \begin{vmatrix} \frac{\partial W}{\partial E^{'}} & \frac{\partial W}{\partial \cos\theta_{e^{'}}} \\ \frac{\partial Q^2}{\partial E^{'}} & \frac{\partial Q^2}{\partial \cos\theta_{e^{'}}} \end{vmatrix} \\ &= \frac{1}{2\pi} \begin{vmatrix} \frac{-E\left(1-\cos\theta_{e^{'}}\right)-M_n}{W} & \frac{EE^{'}}{W} \\ 2E\left(1-\cos\theta_{e^{'}}\right) & -2EE^{'} \end{vmatrix} \\ &= \frac{2E^2E^{'}\left(1-\cos\theta_{e^{'}}\right) + 2M_nEE^{'}}{W} - \frac{2E^2E^{'}\left(1-\cos\theta_{e^{'}}\right)}{W} \\ &= \frac{M_nEE^{'}}{\pi W} \end{aligned} \tag{1.29}$$

From Eq. (1.26) and (1.29) we can calculate the virtual photon flux, which depends on (W, Q^2) by

$$\begin{aligned} \Gamma_\upsilon\left(W,Q^2\right) = \frac{\Gamma_\upsilon\left(E^{'},\Omega_{e^{'}}\right)}{J\left(W,Q^2\right)} &= \frac{\pi W}{EE^{'}M_n}\left(\frac{\alpha}{2\pi^2}\frac{E^{'}}{E}\frac{K_\gamma}{\left(1-\epsilon\right)Q^2}\right) \\ &= \frac{\alpha}{4\pi}\frac{1}{E^2M_n^2}\frac{W\left(W^2-M_n^2\right)}{\left(1-\epsilon\right)Q^2}. \end{aligned} \tag{1.30}$$

Since $Q^2 = -q^\mu q_\mu = |\vec{q}|^2 - \nu^2$ and $Q^2 \simeq 4EE' sin^2 \frac{\theta_e}{2}$, ϵ also can be simplified as

$$\epsilon = \left(1 + 2\left(1 + \frac{\nu^2}{Q^2}\right) tan^2 \frac{\theta_e}{2}\right)^{-1} \simeq \left(1 + 2\frac{Q^2 + \nu^2}{4EE' - Q^2}\right)^{-1} \tag{1.31}$$

The hadronic differential cross section is calculated from the four fold differential cross section (Eq.(1.32)), which is extracted finally from the experimental yield.

$$\frac{d^4\sigma}{dW dQ^2 d\Omega^*_{\pi^-}} = \Gamma_\upsilon \left(W, Q^2\right) \frac{d\sigma}{d\Omega^*_{\pi^-}}. \tag{1.32}$$

$$\frac{d\sigma}{d\Omega^*_{\pi^-}} = \frac{1}{\Gamma_\upsilon \left(W, Q^2\right)} \frac{d^4\sigma}{dW dQ^2 d\Omega^*_{\pi^-}}. \tag{1.33}$$

For the exclusive $\gamma^* n(p) \to p\pi^-(p)$ reaction, we use the same equations to extract the hadronic differential cross section by ignoring the off-shell effects when calculating the virtual photon flux. From now on, W represents W_f, along with Q^2 that are calculated in the neutron rest frame. $\cos\theta^*_{\pi^-}$ and $\phi^*_{\pi^-}$ are calculated from the CM frame of p and π^- system.

1.3 Reaction Models

The direct outputs from experimental data, i.e. cross section and other observables, are not direct inputs for the non-perturbation theories. Therefore, one must develop reaction models for interpreting the data in terms of hadron structure calculations. There have been many approaches to develop those reaction models for investigating pion electroproduction reactions since 1957's first approach, developed by Chew, Goldberger, Low and Nambu (CGLN amplitudes) [21]. In order to investigate the data in the higher resonance region, where two pion and other mesons productions become dominant, isobar models [23] had been developed to extract the parameters of higher mass nucleon resonances. After this, models based on K-matrix effective Lagrangian [24] were developed to study the Δ excitation. Two very useful models, MAID developed in Mainz, Germany [25] and SAID developed at the George Washington University [16], were used to perform amplitude analyses and determine the

resonance parameters from the experimental data [19]. In this thesis, we will compare the final results to these two models.

MAID is coded based on the Unitary isobar model (UIM) [25] to extract the resonance parameters. The first MAID version (MAID98) was constructed with $P_{33}(1232)$, $P_{11}1440$, $D_{13}(1520)$, $S_{11}(1535)$, $S_{11}(1650)$, $F_{15}(1680)$, and $D_{33}(1700)$ resonances described in Breit-Wigner form and a non-resonant background constructed from Born terms and t-channel vector-meson contributions [25]. In this version, the energy dependent mixing of pseudovector (PV) and pseudoscalar (PS) πNN couplings were introduced in the Born terms to describe the right threshold and higher energy behavior. Then each partial wave was unitarized up to the two-pion threshold by using Watson's theorem [26]. The non-resonance background contributions in this version were non-unitarized and determined by using standard Born terms and vector-meson exchange. In the MAID2000 version, the non-resonance background contributions were unitarized for the multipoles up to F-waves according to the prescription of K-matrix theory. Furthermore, some selected data for pion photo- and electroproduction in the energy range up to $W = 1.6$ GeV were fitted [40]. Additionally, for MAID2003, $S_{31}(1620)$, $F_{35}(1905)$, $P_{13}1720$, $P_{31}(1910)$, $F_{37}(1950)$ and $D_{33}(1700)$ resonances were included for the first time. In contrast to previous versions, MAID2003 directly analyzed all the photo- and electroproduction data available since 1960, and made single energy and energy dependent fits independently [26]. For the most recent MAID2007 version, the Q^2 dependence of the Sachs form factors in the Born terms was replaced by a more recent parameterization, and Q^2 evolutions of e.m. form factors as well as realistic pion and axial form factors have been introduced [26].

The SAID model [16] uses K-matrix formalism to determine pion photoproduction multipoles. The electroproduction analysis is similarly anchored to the $Q^2 = 0$ photoproduction results, with additional phenomenological factors intended to account for the Q^2 variation.

Most of the data points fit by these models come from proton measurements. A very small fraction of the data comes from deuterium target experiments, in which the ratio of π^- production to π^+ production is measured, as is listed in the Tab. 1.2.

1.4 Summary

From the above discussions, it is clear that in the absence of fundamental QCD solution in the nucleon and resonance regions, a sufficiently complete electroexcitation database must be established to pin down the distance-dependent baryon structure and to aid in the development of a QCD-based strong interaction theory. The following chapter will introduce the most complete and advanced experimental facility to measuring meson electroproduction in the resonance region.

Chapter 2

Experimental Facility

The data presented here was measured in Hall B at the Thomas Jefferson National Accelerator Facility (TJNAF), also known as Jefferson Laboratory or JLab, in Newport News, Virginia, USA.

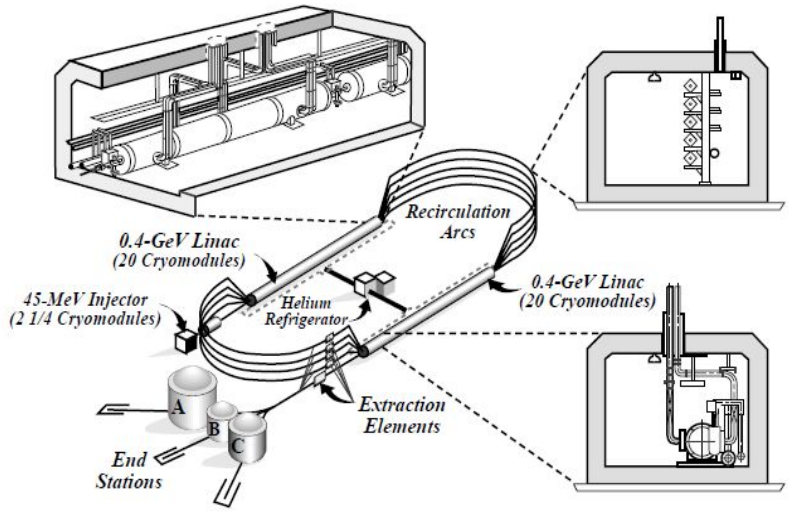

Figure 2.1: Schematic diagram of the CEBAF accelerator shows the injector (serves as a source of electrons), linear accelerators (LINAC), recirculation arcs and three experimental halls.

2.1 Continuous Electron Beam Accelerator Facility (CEBAF)

The schematics of the CEBAF accelerator, which provides an electron beam from the accelerator to three end stations (Hall A, B, and C) simultaneously is shown in Fig. 2.1. A 45 MeV electron beam is delivered to the accelerator by a superconduct-

ing RF injector, then accelerated through two identical linear accelerators (LINACs) connected by two arc stations. As the electron beam is recirculated up to five successive orbits, its energy increases to a maximum of 6 GeV. Because of the 1.497GHz RF structure of the linac cavities, the electron beam bunches are separated by 2 ns intervals in each experimental hall.

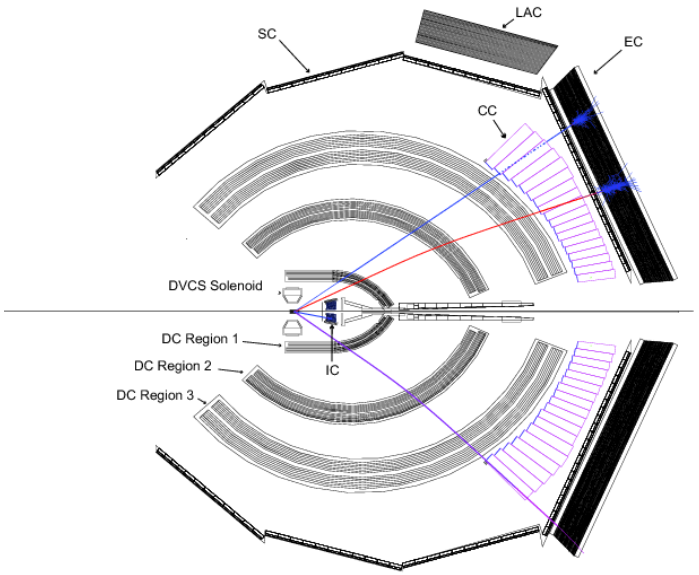

Figure 2.2: (Color online) Schematic view of the CLAS detector, EC–electromagnetic calorimeter, CC–Cherenkov counter, SC–scintillation counter, DC–Drift Chambers. The tracks correspond, from top to bottom, to a photon (blue curve), an electron (red curve) curving toward the beam line, and a proton (purple curve) curving away from the beam line.

2.2 CEBAF Large Acceptance Spectrometer (CLAS)

In Hall B, the major part of the physics program is based on the CLAS (see Fig. 2.2) detector. It is designed to allow operation with both electron and photon beams while providing azimuthal acceptance coverage of almost 2π, the polar acceptance ranges from 8° to 140° for charged particles, and 8° to 45° for neutral particles [46]. The CLAS magnet coils naturally separate the detector into six identical and independent sectors (see Fig. 2.3). Each of the CLAS sectors is equipped with an identical set

of detectors: three layers of drift chambers (DC) for charged particle tracking and momentum reconstruction, Cherenkov counters (CC) for electron identification and triggering, scintillation counters (SC) for time of flight measurements and charged particle identification, and electromagnetic calorimeters (EC) for electron identification and triggering. Each of these components will be discussed in detail in the following sections.

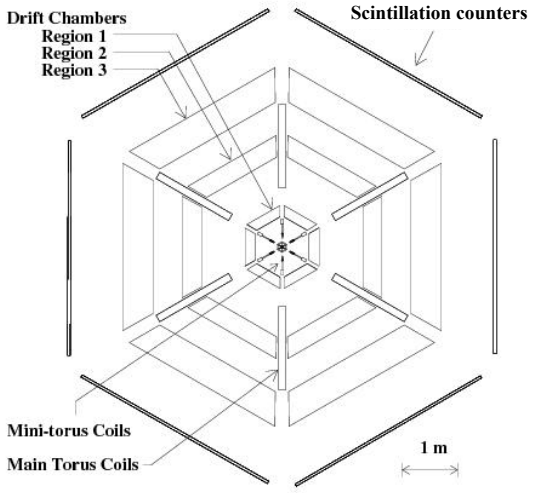

Figure 2.3: The azimuthal view of the CLAS with six independent sectors. The corresponding magnetic field configuration is shown in Figure 2.4b

2.3 Superconducting Toroidal Magnet

The magnet used in CLAS is made of six superconducting coils, which are placed in a way to generate an azimuthally symmetric field (see Fig. 2.4b) of up to 2 Tesla at the maximum coil current of 3860 A [46]. The toroidal magnet is an essential component of the CLAS detector. The charged particles are bent by the magnetic field which is generated by the torus current. The field generated between a torus coil pair is shown in Fig. 2.4a. The curvature of charged particles' trajectory in the magnetic

field is used to reconstruct their momenta from the drift chamber information. Here charged particles deflect inward or outward from the beam line depending on both their charge and the direction of the magnetic field. The orientation of the magnetic field can be reversed by reversing the torus current. For example, the torus current of the CLAS "e1e" run, which is the data set analyzed for the results presented here, is positive. Thus, it bends negatively charged particles inward and positively charged particles outward from the beam line.

2.4 Drift Chambers

The CLAS toroidal magnet bends charged particles inward or outward from the beam axis but leaves the azimuthal angle essentially unchanged. Since a particle that leaves the target and enters a sector then stays within that sector, 18 separate drift chambers were built to track these charged particles and are located at three radial locations in sector. These radial locations are referred to as "Regions" [47]. The "Region One" chambers ($R1$) surround the target in an area of low magnetic field, the "Region Two" chambers ($R2$) are somewhat larger and are situated between the magnet coils in the area of high field near the point of maximum track sagitta, and the "Region Three" chambers ($R3$) are the largest devices, radially located outside of the magnet coils. These relative positions are shown in Fig. 2.2 and Fig. 2.3.

2.5 Cherenkov Detector

The Cherenkov Counter (CC) [14] installed in the CLAS detector is aimed to separate scattered electrons from negative pions when they are not relativistic. The design of the Cherenkov detector aims at maximizing the coverage in each sector (see Fig. 2.6) up to the polar angle (θ) of 45°. This is done by covering as much of the available space as possible with mirrors. In Fig. 2.6, each sector is divided into 18 regions of θ (known as 18 *segments*), and each θ segment is divided into two modules. The optics

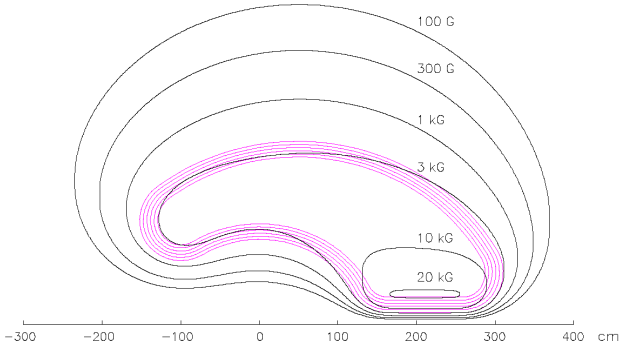

(a)

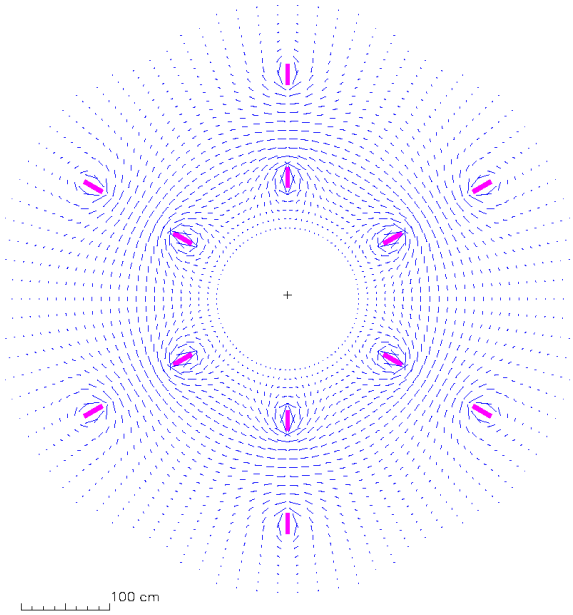

(b)

Figure 2.4: (a) Contours of constant absolute magnetic field for the CLAS toroid in the mid-plane between two coils. The projection of the coils onto the mid-plane is shown for reference (b) Magnetic field vectors for the CLAS toroid transverse to the beam in a plane centered on the target. The length of each line segment is proportional to the field strength at that point. The six coils are seen in cross section [46].

of each module is designed to focus the Cherenkov light into a Winston collector cone leading into a PMT (seen Fig. 2.5), located in the shadow of the torus coils, so that the PMTs do not introduce additional holes in the geometrical acceptance of the detector. A charged particle emits electromagnetic radiation (named as Cherenkov radiation) while traveling through a dielectric medium at a speed exceeding the velocity of light in that medium. Since the velocity threshold of Cherenkov light emission is $\beta = 1/n$, where n is the refraction index of the medium, then the corresponding energy threshold for charged particles is calculated by

$$E = \frac{m}{\sqrt{(1-\beta^2)}} = \frac{nm}{\sqrt{(n^2-1)}}, \tag{2.1}$$

where n is the refraction index of the medium, m is the particle mass, and β represents the velocity of the particle. For CLAS, perfluorobutane(C_4F_{10}) was chosen as the radiator gas for the CC to produce Cherenkov radiation due to its high index of refraction ($n = 1.00153$), which results in a high photon yield and low velocity threshold. So the threshold energy of electrons is about 9 MeV (calculated from Eq. (2.1)). However the negative pions, misidentified as electrons, do not emit the Cherenkov radiation until their momentum exceeds 2.5 GeV.

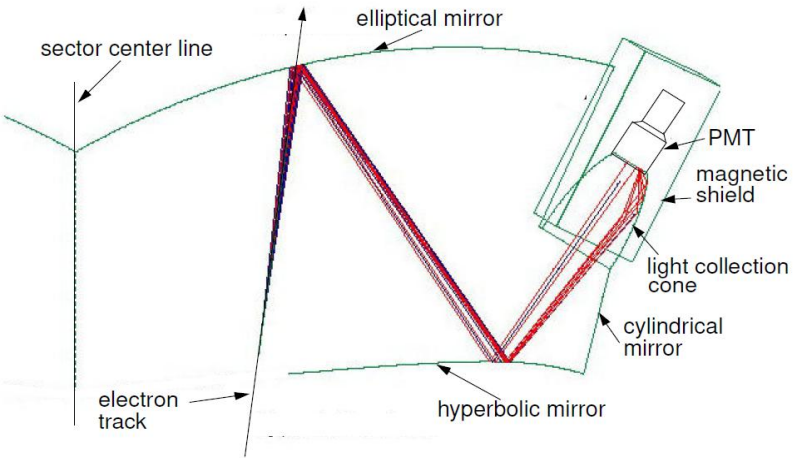

Figure 2.5: Optical arrangement of one of the 216 optical modules of the CLAS Cherenkov detector, showing the optical and light collection components.

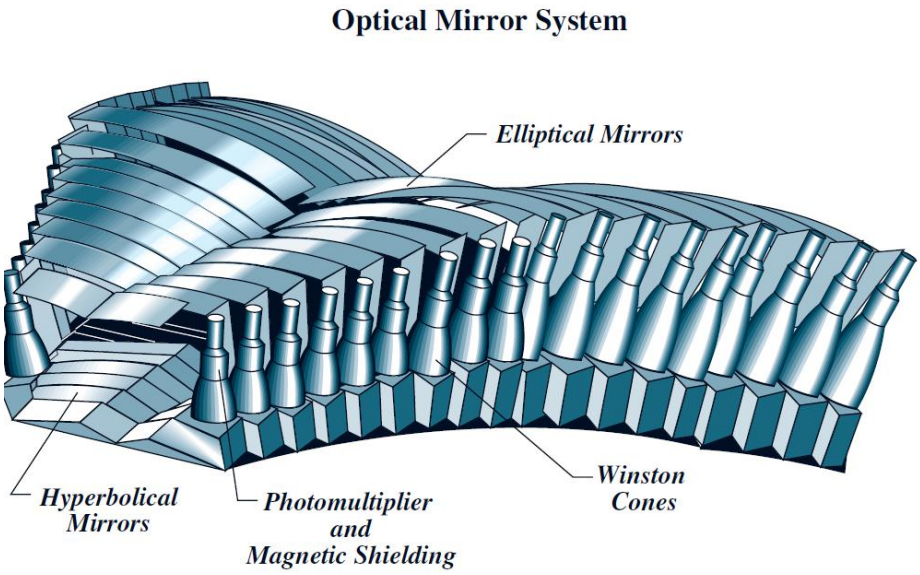

Figure 2.6: A schematic diagram of the CC detector in one of the six sectors.

2.6 Scintillation Counters (SC)

The requirements for the SC system [29] include excellent time resolution for particle identification, good segmentation for flexible triggering, and prescaling. The SC system, along with the DC, is used for charged particle identification. It measures the flight time and track length of particles from the target to one of the scintillator bars, which are used for charged hadron identification that is discussed in Chapter 3.

The system specifications call for a time resolution of $\sigma = 120$ ps at the smallest angles and 250 ps at the angle above 90°. A schematic view of an SC system in one sector of CLAS is shown in Fig. 2.7. Each SC system consists of 57 Bicron BC-408 scintillator paddles mounted in four panels covering the polar angular range between 8° and 142° and the entire active range in the azimuthal angle ϕ. The length of the scintillator paddles varies from 30 cm to 450 cm with a thickness of 5.08 cm. To ease the fabrication, assembly, and testing of a large number of counters, two scintillator widths were chosen to build the system. 15-cm-wide scintillators and 2-inch PMTs were selected for the forward-angle system due to space constraints. For the large-angle system, 22-cm wide scintillators coupled to bent and twisted light guides and

2-inch PMTs were selected. The last 18 scintillator paddles are paired into nine logical counters. This grouping results in the system having a total of 48 logical counters per sector.

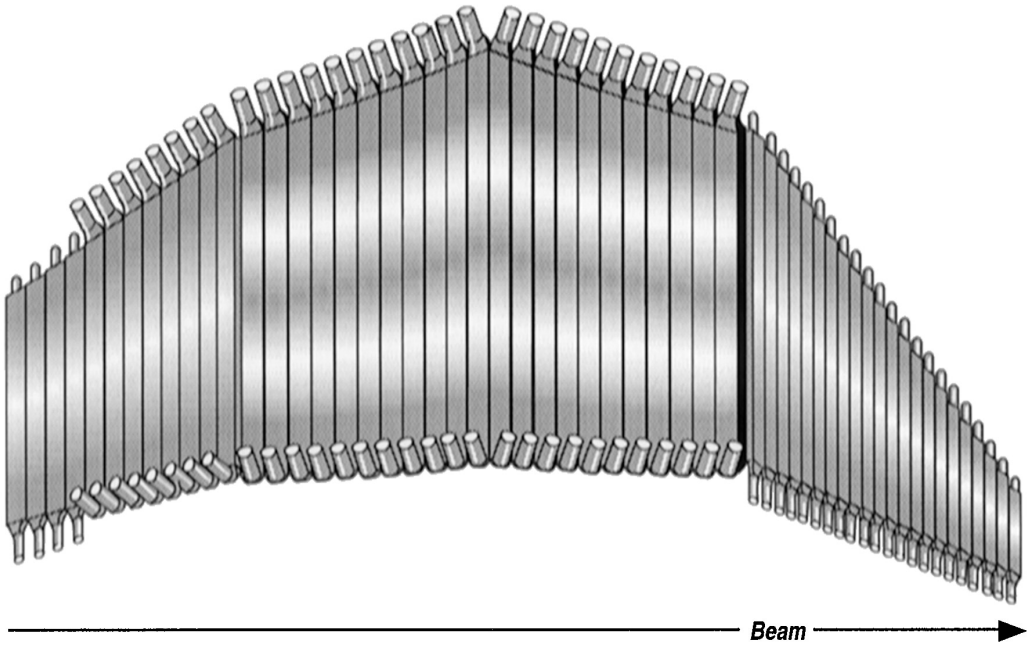

Figure 2.7: A schematic diagram of the SC system in one sector of CLAS. The scintillation counters are arranged in four panels perpendicular to the beam line. Each sector has 57 scintillator paddles with two light guides and two PMTs at the ends of each paddle.

2.7 Electromagnetic Calorimeter

The forward electromagnetic calorimeter (EC) is composed of 39 layers of scintillator alternated with lead sheets and covers $8^\circ < \theta < 45^\circ$ in each sector region [15]. For the purpose of readout, each scintillator layer is made of 36 strips parallel to one side of the triangle, with the orientation of the strips hence rotated by 120° in each successive layer (see Fig. 2.8). Thus there are three orientations or views (labeled U, V, and W), each containing 13 layers, which provide stereo information on the location of energy deposition. Each view is further subdivided into an inner (5 layers) and outer

(8 layers) stack with the optical signal summed within a stack and sent to a PMT. The EC of CLAS performs the following tasks:

- triggering and detection of electrons,
- discrimination of electrons and pions, especially at higher momentum nearing 2.5 GeV,
- detection of photons at energies above 200 MeV for π^0 and η reconstruction from 2γ decay events, and
- detection of neutrons and separation from photons by using EC timing information.

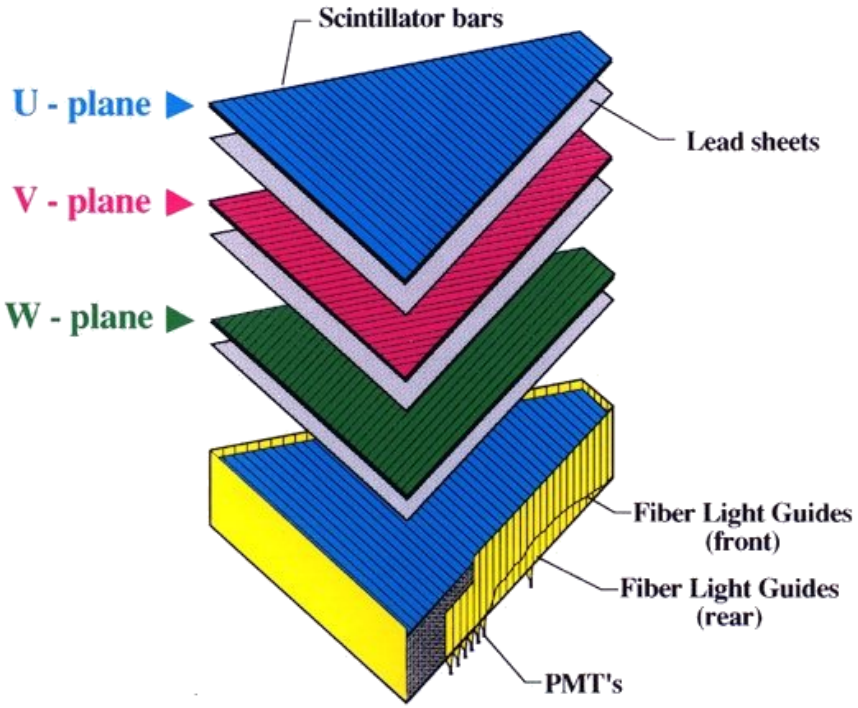

Figure 2.8: Expanded view of one of the six CLAS electromagnetic calorimeter modules.

2.8 Triggering and Data Acquisition

Each CLAS sub-detector has its own electronics to collect all signals. However, a signal does not have to originate from a real physics event, it can be accidental signal, which is caused by cosmic rays or electronic noise. So setting up the detector trigger system helps to select interesting good physics events. Once the trigger system gives a signal, the data acquisition system (DAQ) collects the signals from all sub-detectors and records them into the storage space. Those signals are called "raw" data.

2.9 Experiment Condition

Each CLAS experiment is named as a specific run. For example, the CLAS e1e experiment is called the "e1e" run. Here a run or a run period represents more than one physical experiment. The "e1e" run lasted 20 beam days at an electron beam energy of 2.039 GeV, with a 2-cm unpolarized liquid hydrogen or deuterium as target (see Fig. 2.9) at the beginning of 2003. The target has a conical shape with a diameter varying from 0.4 to 0.6 cm. Data were taken with a +2250 A torus current and +6000 A minitorus current for the main CLAS torus magnets.

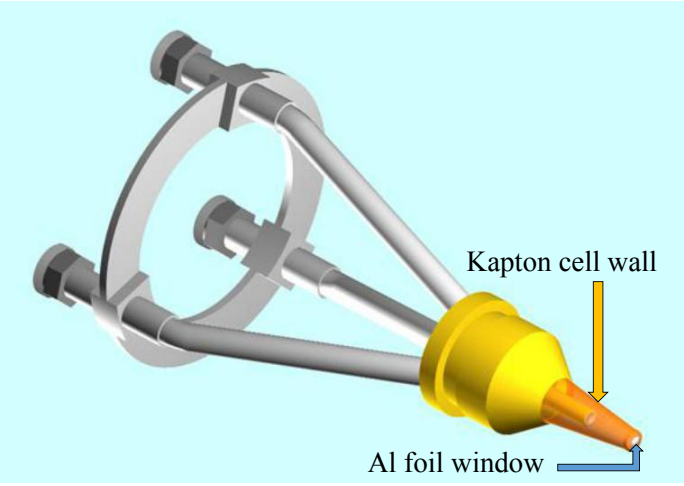

Figure 2.9: A schematic diagram of "e1e" target.

Chapter 3

Data Analysis

In this analysis, the deuterium target data from the "e1e" run is analyzed. The data processing, particle identification, corrections, fiducial cuts, event selection, and kinematical final state interaction correction will be addressed in the following sections.

3.1 Data Processing

The data taken in CLAS is grouped into runs. Here a run is related to a continuous data taking period. An experiment operator usually ends a run once it reaches a certain number of events (135MB for an "e1e" run) recorded by the data acquisition system (DAQ) or when something goes wrong during the data taking process. In this way, a run data set is split further into reasonable pieces (called run files), which can be easily isolated from any software and hardware data taking problem. The "e1e" run period of the liquid deuterium (LD_2) target is subdivided into 94 run and 1985 run files related to the electron beam condition, from which we want to carry out the analysis. Besides these, there are 4 empty target run files, which are taking data without LD_2. The information of the empty target runs is needed to carry out the background subtraction process, details of which are introduced in the Chapter 5.

The raw data files are "cooked" with the CLAS reconstruction and analysis program (RECSIS) to extract information about the detector response and convert the raw detector data into momenta, vertices, times, and particle information, i.e. charge and particle ID. In more detail, the "RECSIS" program is in charge of the following tasks:

- geometrical matching of each DC track to the corresponding hits in the other detectors (i.e. CC, SC, and EC),
- identifying the trigger particle (i.e. electron),
- calculating time information (i.e. trigger time, particle times),
- identifying other particles corresponding to their tracks (i.e. p, π^-), and
- building an event and writing it to the output file (BOS files).

Basically, we choose and optimize which banks need to be saved in the BOS files to record outgoing particle information by setting the "tcl" file [5]. Here, in this thesis, we use the EVNT, DCPB, CCPB, SCPB, and ECPB BOS bank information [6] to carry out the data analysis. Usually, the processed data is converted in different formats including these BOS banks. In this analysis, the output file with "ntuple" format is used because of its ROOT friendly structure.

3.2 Quality Check

In order to reduce the influence of unstable run conditions (due to beam, target, detector, etc.), it is better to check the run quality first. For the LD_2 target run period, we have 1985 run files that need to be checked. The live time is the total time when the DAQ is actually recording events. We plot the ratio of exclusive events to the live-time corrected charge (measured in the Faraday cup) in Fig. 3.1a, then fit it by the Gaussian function, which is shown in red, to get the corresponding fit parameters μ and σ. Then the $\mu - 3\sigma < ratio < \mu + 3\sigma$ cuts shown as two blue lines in Fig. 3.1a are applied to all files, and only the selected "golden" files between the two blue lines in Fig. 3.1b are used for the following data analysis, which are also listed in the reference [7].

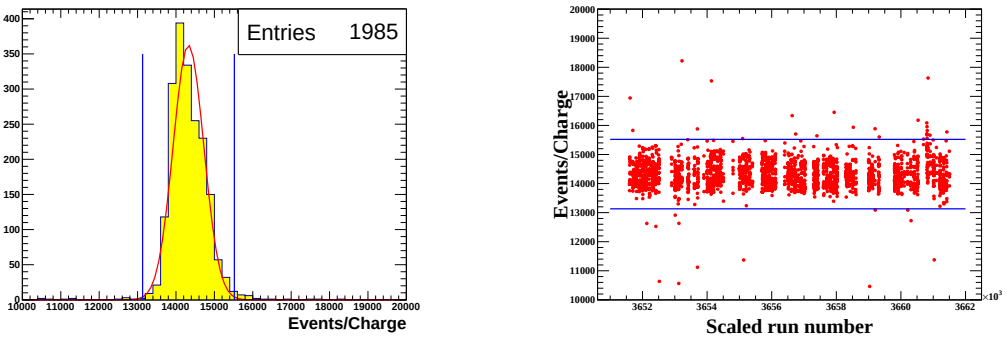

(a) (b)

Figure 3.1: (a) shows the exclusive number of events normalized to the live-time corrected charge for each file, and (b) shows it versus the scaled run number. Here the red curve shows Gaussian fit function, and two blue lines show the 3σ upper/lower cut limits.

3.3 Electron Identification

The EVNT bank IDs (electron ID: 11, proton ID: 2212, and π^- ID: -211), which mark particles based on their basic information and some initial cuts performed during the "cooking" process, are on the cross section level not reliable enough to be used for particle identification. Thus we need to build effective cuts, which can be applied on candidate particles to finalize their particle identity. Here the purpose of cutting on electron candidates is to reduce electronic noise, accidental events, and the negative pion contamination as much as possible without losing good electron candidates. We define an electron candidate by satisfying the following requirements

- First negatively charged track: electron detection triggers the DAQ system to record data from all the sub-detectors of CLAS.
- (DC_{stat}, EC_{stat}, SC_{stat}, and CC_{stat}) bits > 0 [6]: electron should geometrically match each DC track to the corresponding hits in the other detectors.
- *stat* bit > 0 [6]: the trajectory of a electron passes the time-based tracking.

The purpose and details of each electron identification cut will be discussed below.

Minimum Momentum Cut

The forward EC is one of the main trigger components in electroproduction experiments with CLAS. A threshold can be set to require a minimum energy for the trigger. A study of the inclusive cross section at various beam energies with CLAS [27] results in a low momentum cut p_{min} depending on the calorimeter low total threshold (in millivolt) of the trigger discriminator. In that study the safe electron p_{min} is obtained from

$$p_{min}(in\ \text{MeV}) = 214 + 2.47 \times EC_{threshold}(\text{in mV}), \tag{3.1}$$

where, for the "e1e" run, the $EC_{threshold}$ = 100 mV and p_{min} = 461 MeV. So $p_{electron} > 461$ MeV cut is applied on electron candidates at first.

θ_{CC} versus Segment Cut

The requirement of the negative DC track with the corresponding signal in the CC is not good enough to select real electron candidates. Therefore, the θ_{CC} cut is applied to help. Since the torus magnetic field bends the electrons toward the beam line and CC segments are placed radially according to the CLAS polar angle (see Fig. 2.2), it is convenient to use θ_{CC} (see Fig. 3.2) rather than the θ angle at the vertex. There should be an one to one correspondence between θ_{CC} and CC segment number for real electron tracks, while background and accidental noise should not show such correlation. Basically, we can calculate θ_{CC} in Fig. 3.2 from

$$\theta_{CC} = arcos(\frac{\mid \vec{p_z} \mid}{\mid \vec{p} \mid}). \tag{3.2}$$

Here the CC plane equation is $Ax + By + Cz + D = 0$, with $A = -0.000784$, $B = 0$, $C = -0.00168$, $D = 1$, and $\vec{S} = (A,\ B,\ C)$ (see CLAS note [53]). In Fig. 3.2, we can calculate $\vec{P} = \vec{P_0} + t\vec{n}$, where $t = \frac{h}{\cos\alpha}$, and $\cos\alpha = \frac{(\vec{n}\cdot\vec{S})}{|\vec{S}|}$. Then the θ_{CC} distribution of each CC segment is fit by a Gaussian distribution (see Fig. 3.3a), and the corresponding fitting parameters μ and σ are obtained. Then μ, $\mu+3\sigma$, and $\mu-4\sigma$

are plotted in Fig. 3.3b as black stars, which are fit by a second degree polynomial functions. The cuts:

$$\theta_{CC_\mu} - 4\sigma < \theta_{CC} < \theta_{CC_\mu} + 3\sigma, \tag{3.3}$$

accounting for the distribution not being completely symmetric around the mean, are applied to both experimental data and simulation.

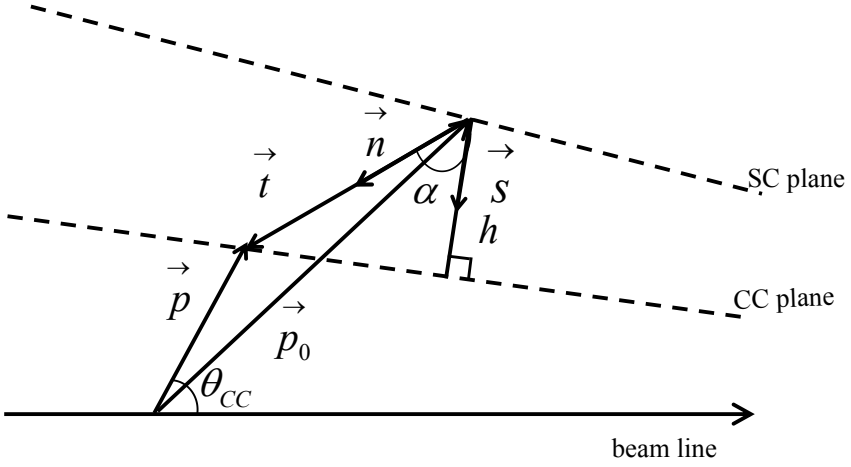

Figure 3.2: Schematic diagram for the θ_{CC} reconstruction. Here $\vec{p_0}$ is the intersection of the track with the SC plane (read from DCPB bank (x_sc, y_sc, z_sc)), $\vec{n}$ is the normalized direction of the track from the SC plane (read from DCPB bank(cx_sc, cy_sc, cz_sc)), and $\vec{p}$ is the unbent track to the CC plane.

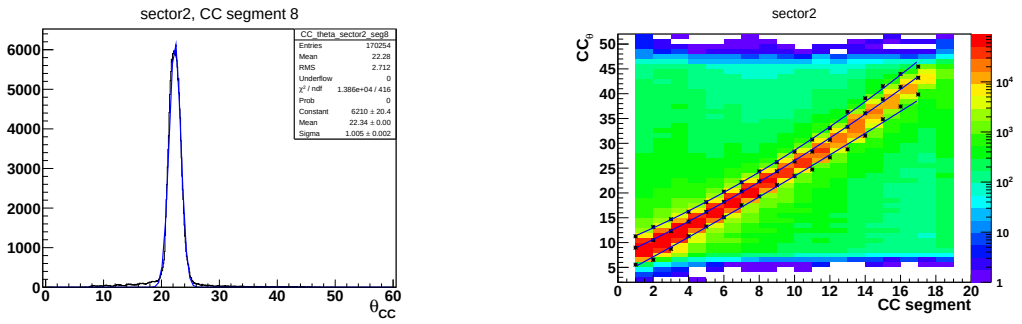

(a) (b)

Figure 3.3: (a) Example θ_{CC} distribution of the 8th CC segment in sector 2, where the blue curve shows the Gaussian fit function, and the fitting parameters μ and σ are shown in the statistic box. (b) The θ_{CC} versus segment number in sector 2 is plotted, where μ, $\mu + 3\sigma$, and $\mu - 4\sigma$ are marked as black stars and fit by a second degree polynomial functions, which are shown as blue curves.

The Cut on Number of Photo-electrons

The Cherenkov detector is designed to separate negative pions from electrons. In the CC, the momentum threshold for electrons and pions are $\sim$ 9 MeV/c and $\sim$ 2.5 GeV/c, respectively. The CC's ADC signal is converted to a number of photo-electrons (N_{phe}) and multiplied by 10 ($N_{phe} \times 10$ caused by the reconstruction code). In order to better eliminate negative pions and background noise, a $N_{phe} \times 10 > 30$ cut is applied on electron candidates. For example, in Fig. 3.4, the green area under the Poisson fit function (from Eq. (3.5) marked as red curve) corresponds to safe electron candidates, and the small peak at $N_{phe} \times 10 \sim 20$ contains not only background and negative pions, but also good electron candidates with low CC efficiency hits. With the extrapolation of the fitted Poisson function we can quantify those lost candidates by the calculated red area, which can be recovered by applying the correction factor ($N_{phe_{correct}}$) as a weight for each accepted event. The weight factor $N_{phe_{correct}}$ is calculated by

$$N_{phe_{correct}} = \frac{green\ area}{red\ area + green\ area} = \frac{\int_{30}^{450} f(x)dx}{\int_{0}^{30} f(x)dx + \int_{30}^{450} f(x)dx}, \tag{3.4}$$

where $f(x)$ is the fitted Poisson function (see red curves Fig. 3.4) defined as

$$f(x) = p_0 \frac{p_1^{(\frac{x}{p_2})} e^{-p_1}}{\Gamma(\frac{x}{p_2} + 1)}, \tag{3.5}$$

where p_0, p_1, and p_2 are free fit parameters. Then the green and red area are calculated by integrating the fitted Poisson function (Eq. 3.4). The correction factor is calculated from the $N_{phe} \times 10$ distribution of left/right PMT in each CC segment per sector. After applying the $N_{phe} \times 10 > 30$ cut, the weight of events is set to be $N_{phe_{correct}}$ rather than 1, and the final cross sections are calculated from those weighted events.

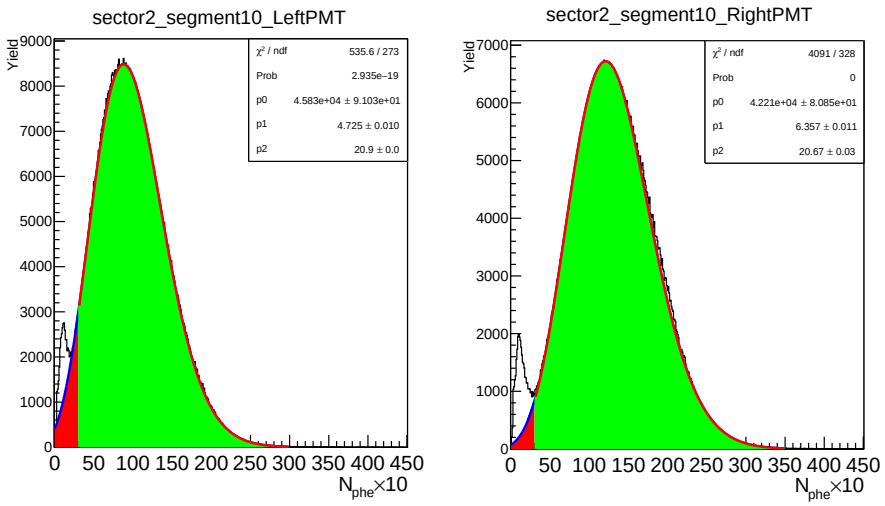

Figure 3.4: Example $N_{phe} \times 10$ distributions of left and right PMTs in the CC 10th segment of sector 2 plotted separately and fit by the Poisson function Eq. (3.5) marked as red curve.

Sampling Fraction Cut

When high momentum pions exceed the Cherenkov radiation threshold, the separation of electrons and negative pions becomes impossible by the CC. Thus the EC is used for separating the electrons from the fast moving pions. Pions and electrons have different mechanisms of primary energy deposition in the EC. Electrons deposit their energy mainly by bremsstrahlung and pair production and subsequent showering reactions. This energy deposition mechanism is momentum dependent. Meanwhile, pions lose most of their energy due to the ionization, which is here practically independent of their momentum. Actually, the incident charged particles can interact with the lead atoms of the EC detector when they are moving through, so the EC can only measure a fraction of their energy. The fraction is called a sample fraction (SF) $\frac{E_{total}}{p}$, which is the ratio of the total energy deposited in the EC to the momentum. For e^-/π^- separation, all electron candidates are divided into eight momentum (p) bins, and in each of them, the $\frac{E_{total}}{p}$ is plotted and fit with Gaussian function (see Fig. 3.5a). Then the corresponding fit parameters μ, $\mu + 3\sigma$, and $\mu - 3\sigma$ are plotted on Fig. 3.5b as black stars, which are fit by a third degree polynomial functions. The

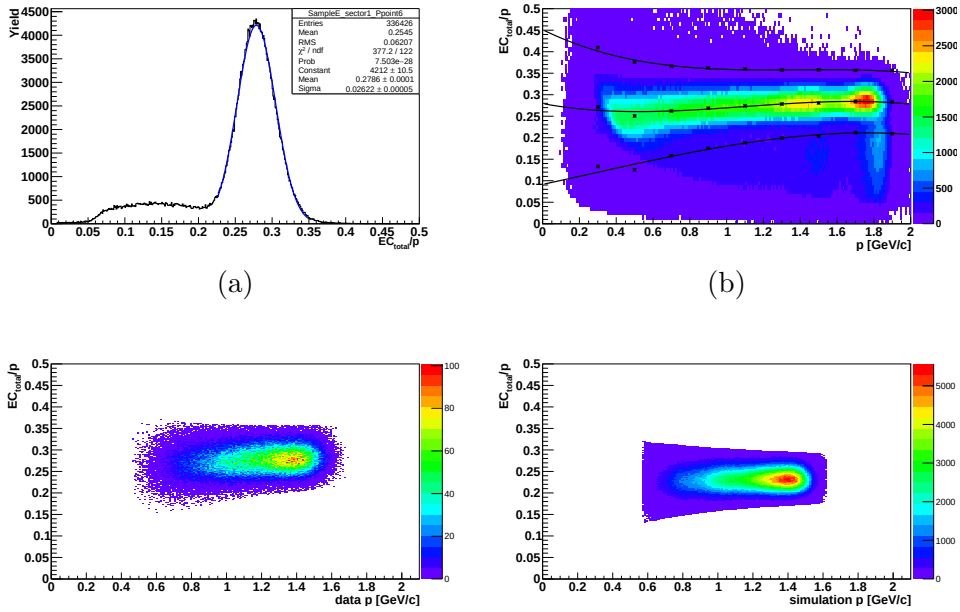

Figure 3.5: (a) An example of an E_{total}/p distribution is fit with a Gaussian function (blue line). (b) E_{total}/p versus p distribution, where the black lines show the upper/lower E_{total}/p cut limits. (c) E_{total}/p versus p distribution after all experimental data event selections. (d) E_{total}/p versus p distribution after all simulation event selections.

cuts,

$$(\frac{E_{total}}{p_e})_\mu - 3\sigma < \frac{E_{total}}{p_e} < (\frac{E_{total}}{p_e})_\mu + 3\sigma, \tag{3.6}$$

are applied to the data. An example E_{total}/p distribution of the survival data is shown in Fig. 3.5c. Since the sampling-fraction distributions of simulated reconstructed events are shifted compared to the data, modified cuts are built by the same method as for the data and applied to the simulated reconstructed events. An example distribution from the simulated events that survive the cut is given in Fig. 3.5d.

3.4 Pion Identification

Similar to the electrons, pions are affected by the geometrical and efficiency effects of different sub-detectors of CLAS. A pion candidate should satisfy initial requirements as follow:

- coincidence with one and only one good electron,
- not the first negatively charged track,
- (DC_{stat}, SC_{stat}) bits > 0 [6]: the pion candidates must have signal from DC and SC, and
- *stat* bit > 0 [6]: like for the electron, the trajectory of a pion should pass the time-based tracking.

Pion ΔT Cut

The time difference ΔT_i between the time calculated by the speed and track length of the pion candidates and the actual measured SC time t_i^{sc} should peak at zero for pions. This time difference is given by

$$\Delta T_i = \frac{l_i^{sc}}{\beta_i c} - t_i^{sc} + t_0 \sim 0, \tag{3.7}$$

where $\beta_i = \frac{v_i}{c}$ is the speed of the pion candidate calculated from the momentum and the assumed mass m_i of the pion by

$$\beta_i = \sqrt{\frac{p_i^2}{m_i^2 c^2 + p_i^2}}, \tag{3.8}$$

and t_0 is the start time of each reconstructed event

$$t_0 = t_e^{sc} - \frac{l_e^{sc}}{c}. \tag{3.9}$$

Here t_e^{sc} is the electron time measured from SC, l_e^{sc} is the path length of the electron track from the vertex to the SC hit, and c is the speed of light. Then t_0 is used as the reference time for all remaining tracks in that event. The calculated ΔT_i for each pion candidate is plotted in different momentum bins for each sector, as seen in the example in Fig. 3.6a for the 0.4 GeV/c $< p_\pi <$ 0.6 GeV/c bin in sector 3, and then fit by a Gaussian function to get the parameters μ and σ of the peak. After applying

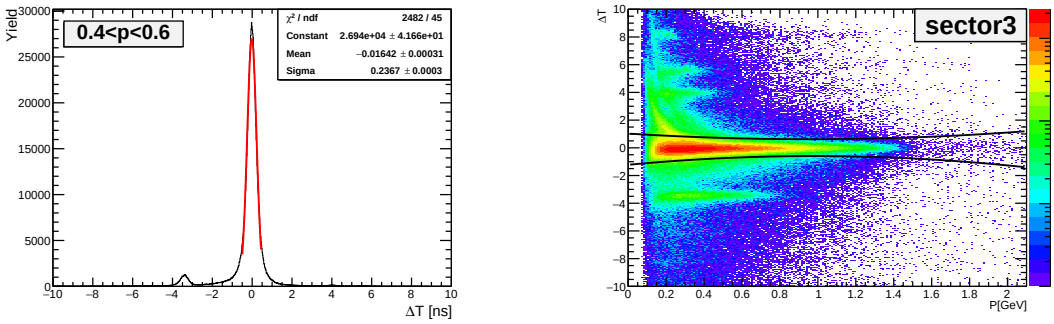

(a) (b)

Figure 3.6: (a)Pion ΔT distribution with fitted Gaussian function (red curve) at 0.4 GeV/c $< p_\pi <$ 0.6 GeV/c for sector 3. (b)Pion ΔT versus p_π distribution with upper/lower ΔT cut limits for sector 3.

the same method for all covered momentum bins, we get two fitted polynomial curves for $\mu - 3\sigma$ and $\mu + 3\sigma$, which are shown in Fig. 3.6b in an example. Next the cuts,

$$(\Delta T_{\pi^-})_\mu - 3\sigma < \Delta T_{\pi^-} < (\Delta T_{\pi^-})_\mu + 3\sigma, \tag{3.10}$$

will be applied on the initial pion candidates for each detector sector individually. However, in this way, we will lose some good pion candidates that are shown in side band peaks in Fig. 3.6b, due to improper time reconstruction. In order to correct these side band events, we plot the ΔT distribution for each counter in the SC system per sector to check the side band problem. Figure 3.7a shows an example of a side band peaking at -3.90 ns and the main zero peak shifted to -0.05 ns as well as the Gaussian functions fitted for both peaks to get the corresponding fitting parameters μ_1 and μ_2. Then two shifts,

$$\Delta T = \Delta T - \mu_1(-3.90 \text{ ns}), \text{ for } \Delta T < -2 \text{ ns and} \tag{3.11}$$

$$\Delta T = \Delta T - \mu_2(-0.05 \text{ ns}), \text{ for } \Delta T > -2 \text{ ns}, \tag{3.12}$$

are applied to correct for the improper time reconstruction. After the correction, Fig. 3.7b shows the results. Since the last 18 scintillation paddles of the SC system are paired into 9 logical counters, it is more likely to have ΔT side bands in the last

9 logical counters per sector, as seen in the examples of the ΔT distribution without and with ΔT shifts for counters from 40 to 48 in sector 3 in Fig. 3.8 and Fig. 3.9 individually. The ΔT shift of each counter per sector are listed in Tab. A.3 and Tab. A.4 of the Appendix A.

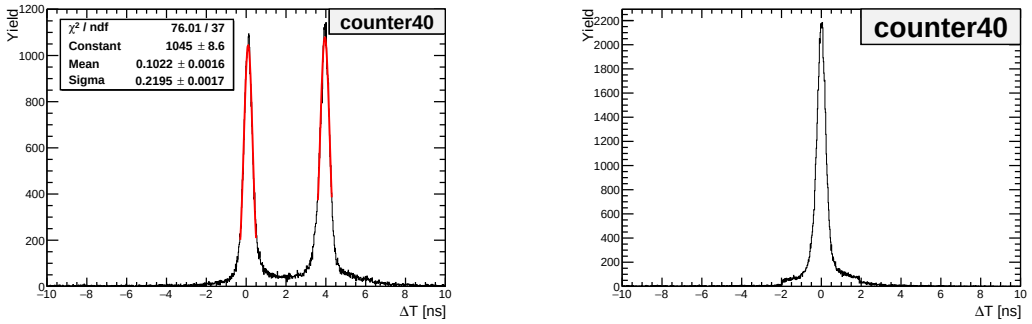

(a) (b)

Figure 3.7: (a) The pion ΔT distribution in counter 40 of sector 3 shows two peaks at 0.1 ns and 3.9 ns (side band peaks), which are fit by two Gaussian functions (red curves) to get the shift parameters. (b) The same ΔT distribution with ΔT shift correction.

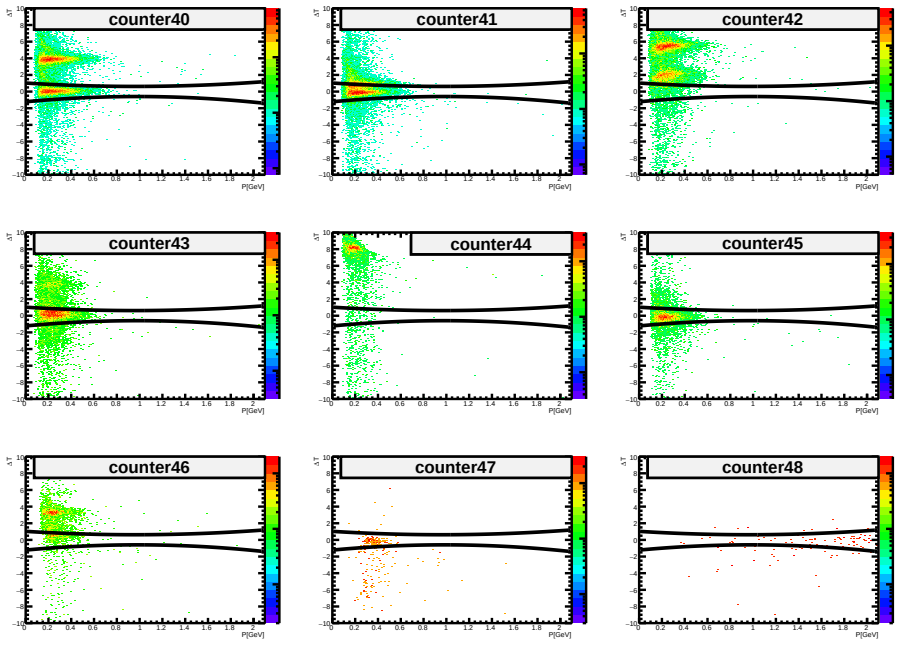

Figure 3.8: The pion ΔT versus p_π distribution with upper/lower ΔT cut limits from counter 40 to 48 of sector 3.

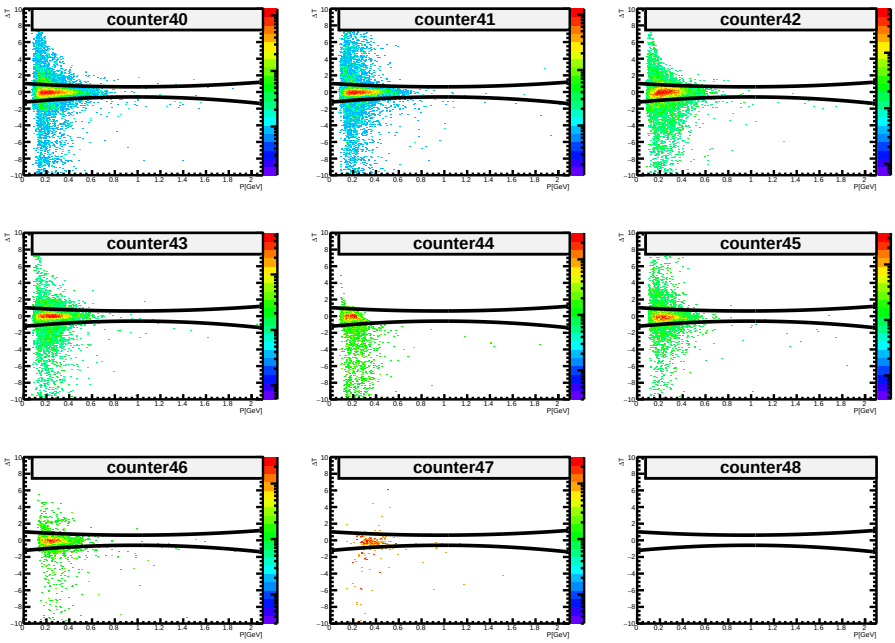

Figure 3.9: The pion ΔT versus p_π distribution with upper/lower ΔT cut limits from counter 40 to 48 of sector 3 after the ΔT shift correction.

3.5 Proton Identification

Similar to the pions, a proton candidate should satisfy initial requirements as follows:

- coincidence with one and only one good electron,
- not the first positively charged track,
- (DC_{stat}, SC_{stat}) bits > 0 [6]: the proton candidates must have signals from both the DC and the SC, and
- *stat* bit > 0 [6]: like the electron, the trajectory of a proton should pass the time-based tracking.

Proton ΔT Cut

For the proton ΔT calculation, the Eq. (3.7) and (3.8) are used by substituting i for proton candidates. Then, in a similar way as for pions, proton ΔT upper/lower cut

limits are carried out from the ΔT fit method in individual proton momentum bins by

$$(\Delta T_{proton})_{\mu} - 3\sigma < \Delta T_{proton} < (\Delta T_{proton})_{\mu} + 3\sigma, \tag{3.13}$$

and an example is shown in Fig. 3.10a and Fig. 3.10b. Since improper time reconstruction is independent of particle type, ΔT shift correction parameters for protons are the same as pions.

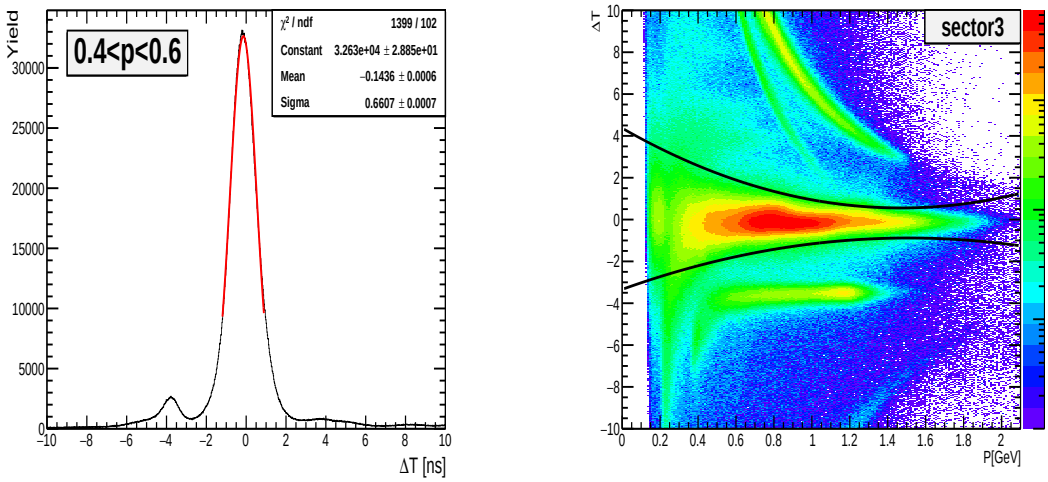

(a) (b)

Figure 3.10: (a) Proton ΔT distribution with Gaussian fit function (red curve) at 0.4 GeV/c $< p_{\pi} <$ 0.6 GeV/c for sector 3. (b) Proton ΔT versus p_{proton} distribution with upper/lower ΔT cut limits for sector 3.

The example plots, which show that the ΔT shift correction parameters for pions also work well for protons, are presented in Fig. 3.11 and 3.12, which are ΔT versus p_{proton} distributions without and with a ΔT shift (same as pions). Since protons are bent outward from the beam line, it is easy to use proton's ΔT distribution to test the higher counter number problem. Here, Fig. 3.11 shows that the counter 48 has collected unreasonable amount of events for unknown reason. After the whole checking process, all events from the counters 48 of all sectors and the counter 17 of sector 5 are deleted.

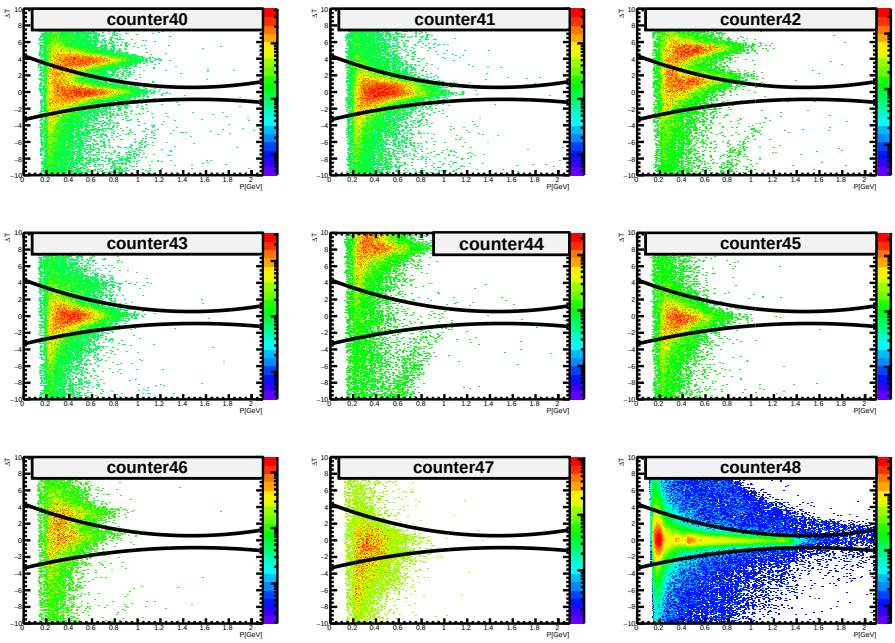

Figure 3.11: The proton ΔT versus p_π distribution with upper/lower ΔT cut limits from counter 40 to 48 of sector 3.

3.6 Kinematic Corrections

Due to our incomplete knowledge of the actual CLAS detector geometry and magnetic field distribution, which is not reproduced precisely in the simulation process, a momentum correction of electrons needs to be carried out for experimental data only. In addition, relativistic charged particles other than electrons lose a measurable part of their energy by traveling through the target and detector materials due to ionization. Hence, the reconstructed momentum is lower than the initial momentum of these particles right at the vertex of the reaction. This effect has much more influence on the heavy charged particles, which are the low energy protons in the $\pi^- p$ channel, and can lead to mis-determination of kinematic quantities such as missing mass and missing momentum. This effect is also reproduced in the simulation process also. Therefore, the energy loss correction needs to be applied to the reconstructed proton momentum for both experimental reconstructed data and simulation events.

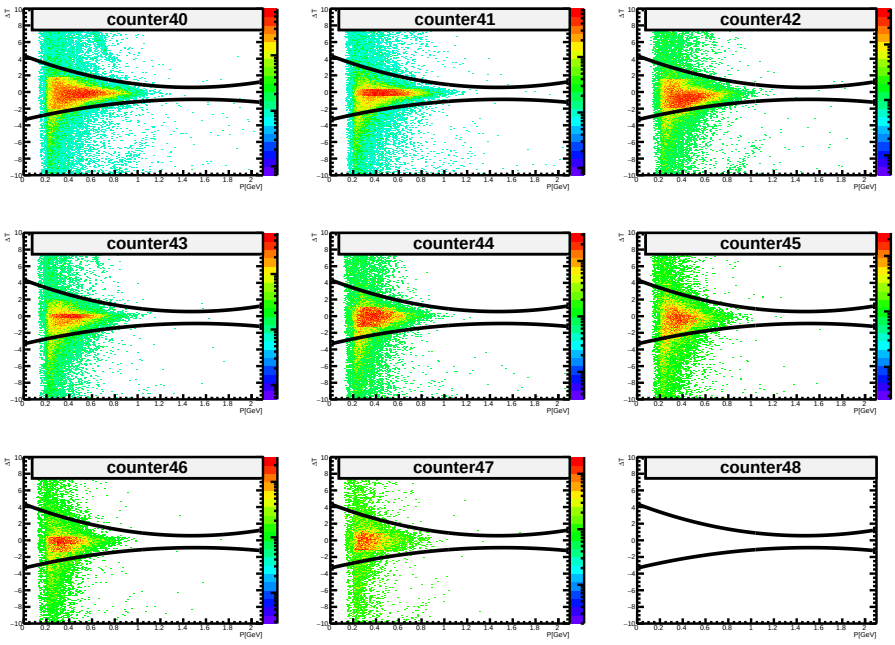

Figure 3.12: The proton ΔT versus p_π distribution with upper/lower ΔT cut limits for counter 40 to 48 of sector 3 after the ΔT shift correction.

Electron Momentum Correction

For the electron momentum correction, we used elastic events from the "e1e" run with a proton target. As described in reference [55], the electron momentum correction method includes two parts, electron polar angle and momentum magnitude corrections, which are both developed for each sector individually. An example missing mass squared distribution for the "spectator" proton is shown in Fig. 3.16. The comparison between the black (no correction) and blue (with electron momentum correction) lines shows that the electron momentum correction shifts the missing mass peak towards its expected value. But it is not enough, we have to carry out the proton energy loss correction, which is introduced next.

Proton Energy Loss Correction

Original generated protons with momenta from 0 to 2 GeV and uniform polar and azimuthal angles are passed through the GSIM and RECSIS reconstruction processes

with all detector materials switched on. The momentum differences between gen-

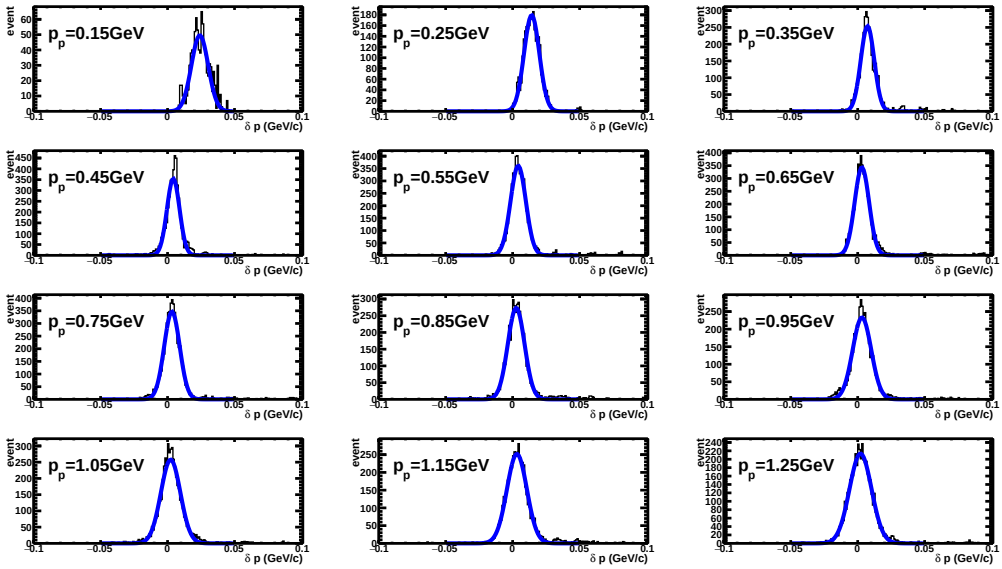

Figure 3.13: The differences between generated and reconstructed protons are presented by the black distributions for different p_p at $\theta_p = 15°$. The blue lines indicate the Gaussian fits.

erated and reconstructed protons (δp) are shown in Fig. 3.13, where as the ratio between the Gaussian fit peak position (in Fig. 3.13) and the corresponding reconstructed momentum value as a function of the reconstructed proton momentum is plotted in Fig. 3.14. By fitting the black circles in Fig. 3.14, the dependence of the momentum correction factor on the reconstructed momentum can be identified clearly. Furthermore, the dependence of these fit parameters on corresponding θ_p is also shown in Fig. 3.15. Finally, the energy loss correction factor (δp) is given by

$$\delta p = par[0] + par[1]p + par[2]/p, \tag{3.14}$$

where par[0], par[1], and par[2] are the fit parameters that depend on θ_p. They are defined by

$$\begin{aligned} par[0] &= c_0 + c_1\theta_p - c_2, \\ par[1] &= c_3 - c_4\theta_p + c_5(\theta_p)^2, \\ par[2] &= c_6 - c_7\theta_p + c_8(\theta_p)^2, \end{aligned} \tag{3.15}$$

where the parameters c_i $(i = 0, 1, 2, 3, 4, 5, 6, 7, 8)$ are listed in Tab. A.5 of the Appendix A.

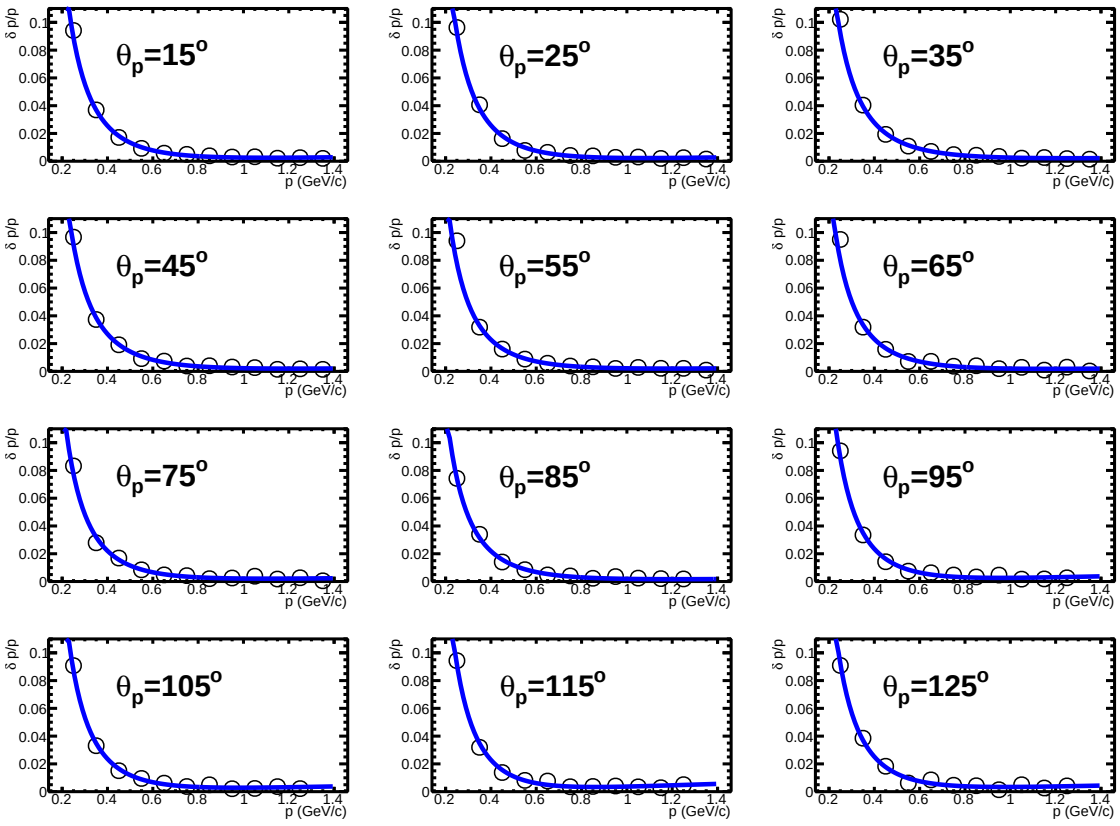

Figure 3.14: The ratio between Gaussian fit peak positions (in Fig. 3.13) and corresponding reconstructed momentum values, $\delta p/p$, plotted against the reconstructed proton momentum (p) is presented by the black circles, and the blue lines show the corresponding fit functions.

After electron momentum and proton energy loss corrections, the Gaussian-fitted missing mass squared distributions of spectator proton $((q^\mu + D^\mu - (\pi^-)^\mu - p^\mu)^2)$ without any kinematic correction, with only electron momentum correction, and with both corrections are plotted for each sector to check the quality of kinematic corrections, and typical examples are shown in Fig. 3.16. Then the corresponding fitted Gaussian means are obtained from these distributions to calculate $\mu^2_{mism_{spector}} = \mu^2$. Figure 3.17 shows that the values of $\mu^2_{mism_{spector}}$ with both electron and proton momentum corrections are closer to 0.88 GeV^2 (squared proton rest mass value) for all

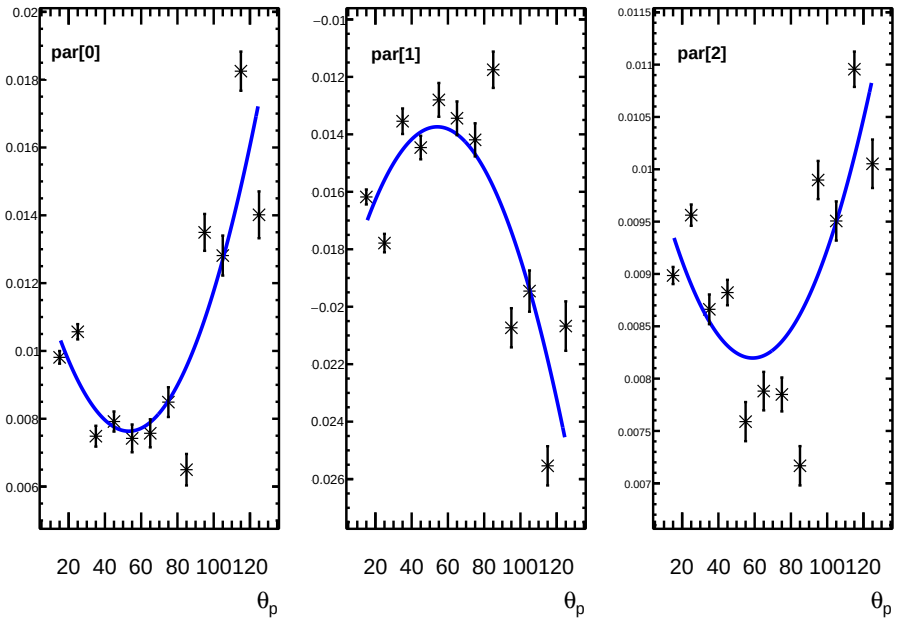

Figure 3.15: Fit parameters of $\delta p/p$ versus (p) distributions plotted against the reconstructed proton θ is presented by the black points, and the blue lines show the corresponding fit functions. Here par[0], par[1], and par[2] correspond to the fit parameters in Eq. (3.14).

sectors.

3.7 Electron Fiducial Cuts

The purpose of the fiducial cuts is to select maximally covered phase space regions with stable detector efficiencies, which are reproduced well in simulation. Due to the complex and different properties of the CLAS sub-detectors, the following fiducial cuts are introduced and applied to both experiment and simulation reconstructed data.

EC Coordinate U, V, and W Fiducial Cut

When an electron hits the forward EC, it is expected to deposit energy proportional to its momentum. However, there is a chance that the shower produced by the electron

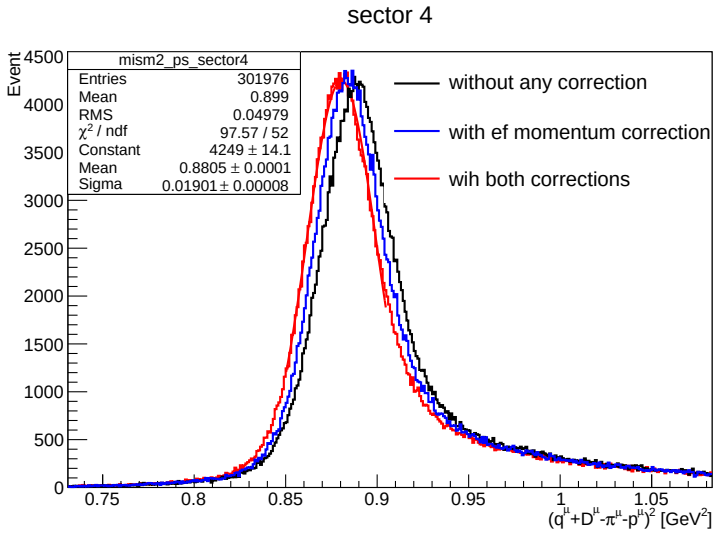

Figure 3.16: The example missing mass squared distributions of the spectator without any kinematic corrections (black line), with only electron momentum corrections (blue line), and with both electron momentum and proton energy loss corrections (red line) are plotted for sector 4, where the fit parameters in the statistics legend box correspond to the red-line Gaussian function fit.

will not be fully deposited in the calorimeter due to hitting it on the edge of the calorimeter. To avoid this kind of effect, we first cut out the edge of the U, V and W coordinate planes (see Fig. 2.8) of EC. The cut limits 40 cm $< U <$ 400 cm, $V <$ 370 cm, and $W <$ 405 cm are illustrated in Fig. 3.18. There is a chance that the condition of the EC is changed for some particular region. In order to avoid that, we check U, V, and W distributions for each sector. Additionally it turned out that there is a hole in the V distribution of sector 3 (see Fig. 3.19). The hole is cut out by demanding $V <$ 305 cm and $V >$ 321 cm.

ϕ_e versus θ_e Cut

Since the fiducial cut in the ϕ_e versus θ_e plane depends on the momentum of electrons (p_e), we plot the ϕ_e distribution for each θ_e and p_e interval per sector, which is expected to be a flat distribution (see green regions in Fig. 3.21) because the cross section is ϕ_e independent. The empirical shape of this kind of fiducial cut is carried

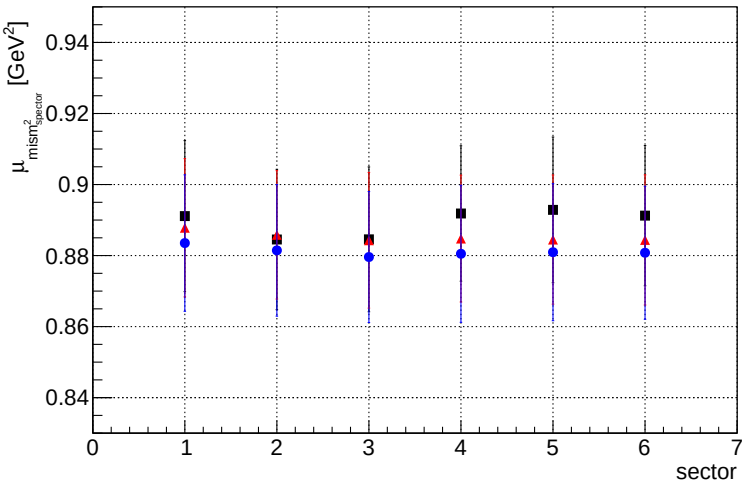

Figure 3.17: The $\mu^2_{mism_{spector}}$ versus detector sectors without any kinematic corrections (black squares), with only electron momentum corrections (red triangles), and with both electron momentum and proton energy loss corrections (blue dots).

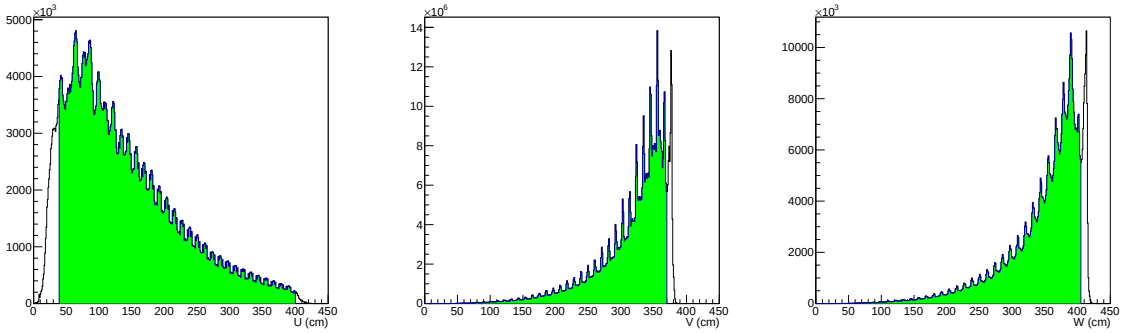

Figure 3.18: The U, V, and W coordinate distributions in the electromagnetic calorimeter. The green area represents the selected events after the cuts.

out in [30] for the "e1e" run and is formulated as

$$\Delta\phi_e = 37.14 sin((\theta_e - \theta_{min})\frac{\pi}{180^\circ})^{p_1+\frac{p_2}{\theta_e}+\frac{1500.0}{\theta_e^2}}, \tag{3.16}$$

where $\Delta\phi_e$ represents the portion of the azimuthal angle ϕ_e accepted by the electron fiducial cut for all possible corresponding kinematic variables θ_e and p_e. Here θ_{min} is the acceptable minimum polar angle θ_e, which is calculated by

$$\theta_{min} = 12.0 + \frac{17.0}{p_e + 0.14}. \tag{3.17}$$

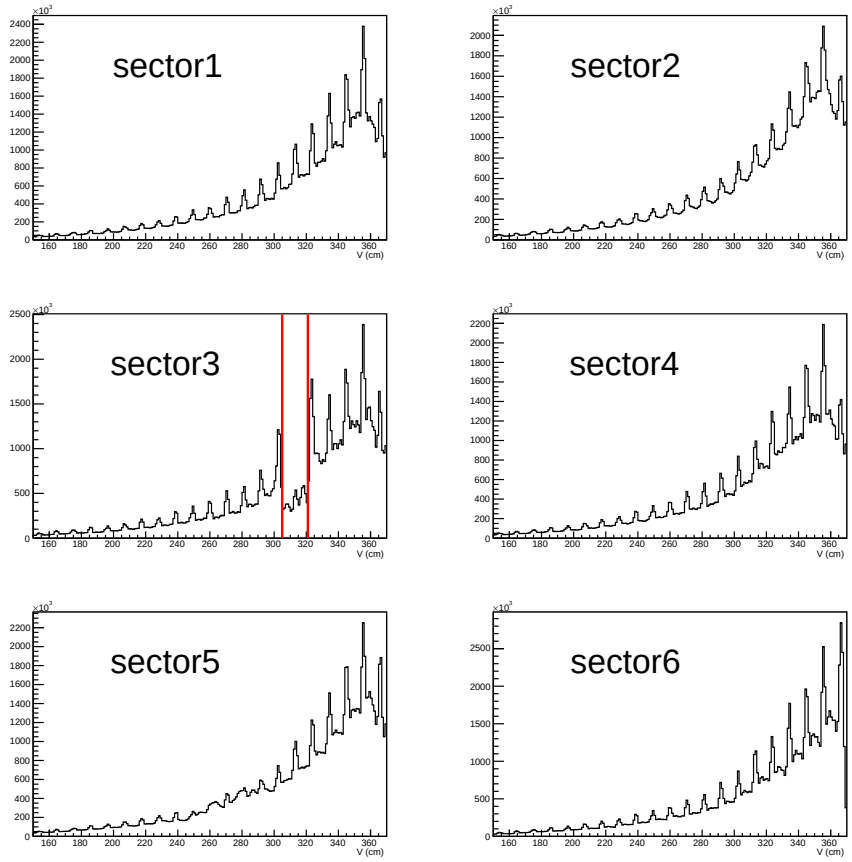

Figure 3.19: The V coordinate distribution in the electromagnetic calorimeter. Red lines represent the hole cut limits.

Furthermore, $p_1 = 0.705 + 1.1p_e$ and $p_2 = -63.1 + 30.0p_e$ are two momentum related parameters. Finally, the accepted regions are $\theta_{min} < \theta_e < 50^\circ$ and $(sector - 1)60^\circ - \Delta\phi_e < \phi_e^{sector} < (sector - 1)60^\circ + \Delta\phi_e$, which are the same for experiment and simulation reconstructed data and are shown inside the blue lines of Fig. 3.20 for examples.

The Electron Polar Angle (θ) versus Momentum (p) Cut

As seen in Fig. 3.20, there are low efficiency regions (mainly caused by the dead wires of DC and bad counters of SC) in the sectors 2, 3, and 5, which should be removed by the "cooking" process and correctly translated to the simulation. However, this is not

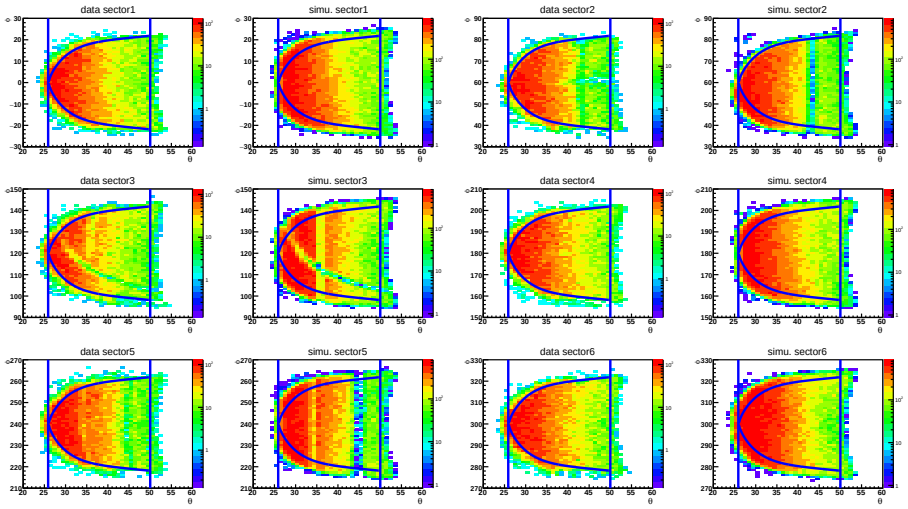

Figure 3.20: θ_e versus ϕ_e distributions of electrons are plotted for six sectors for experiment (left) and simulation (right) reconstructed data each side by side within the 0.8 GeV $< |\vec{p}_e| <$ 1.0 GeV momentum interval. The blue lines show the fiducial cut boundaries for electrons.

always the case, sometimes the simulation reconstructed events are not reproducing those low efficiency regions, and this will cause problems in calculating the correct acceptance of the detector. So, we remove detector low efficiency regions based on the θ versus p distribution for each final particle in each sector separately. In Fig. 3.22, the middle black paired lines show boundaries of the removed regions in each sector for electrons, which are applied simultaneously to experiment and simulation reconstructed data.

3.8 Pion Fiducial Cuts

The purpose of pion fiducial cuts is very similar to that of electron fiducial cuts. Since we do not fully understand some of the low efficiency regions of the sub-detectors, we cannot fully incorporate these effects in the simulation procedure. The solution is to cut out those regions exactly in the same way for both experiment and simulation reconstructed data. The following fiducial cuts are carried out for pions.

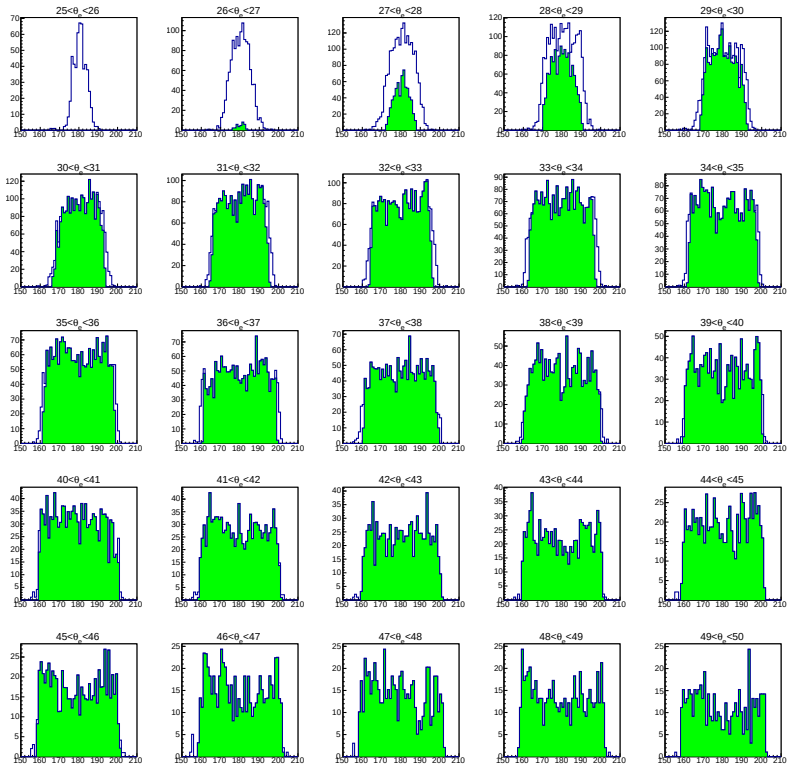

Figure 3.21: Example ϕ_e distributions of electrons in sector 4 for data with 0.8 GeV $< |\vec{p}_e| <$ 1.0 GeV before (blue) and after (green) fiducial cuts.

The Pion ϕ versus θ Cut

For pions, we also need to cut out the boundary regions of the detector. We initially plot their ϕ versus θ distributions in different p_{π^-} momentum bins in each sector as seen in the examples in Fig. 3.24. Then we project these distributions on to the ϕ axis for each θ bin, as shown in Fig. 3.23a. The data is fit by a "trapezoid + constant background" function (red curve), which is defined [51] by

$$f = \begin{cases} P_5 & , \ \phi < P_2, \\ (P_4 - P_5)\frac{\phi - P_2}{P_0 - P_2} + P_5 & , \ P_2 \leq \phi < P_0, \\ P_4 & , \ P0 \leq \phi \leq P_1, \\ (P_4 - P_6)\frac{\phi - P_3}{P_1 - P_3} + P_6 & , \ P1 < \phi \leq P_3, \text{ and} \\ P_6 & , \ \phi > P_3, \end{cases} \tag{3.18}$$

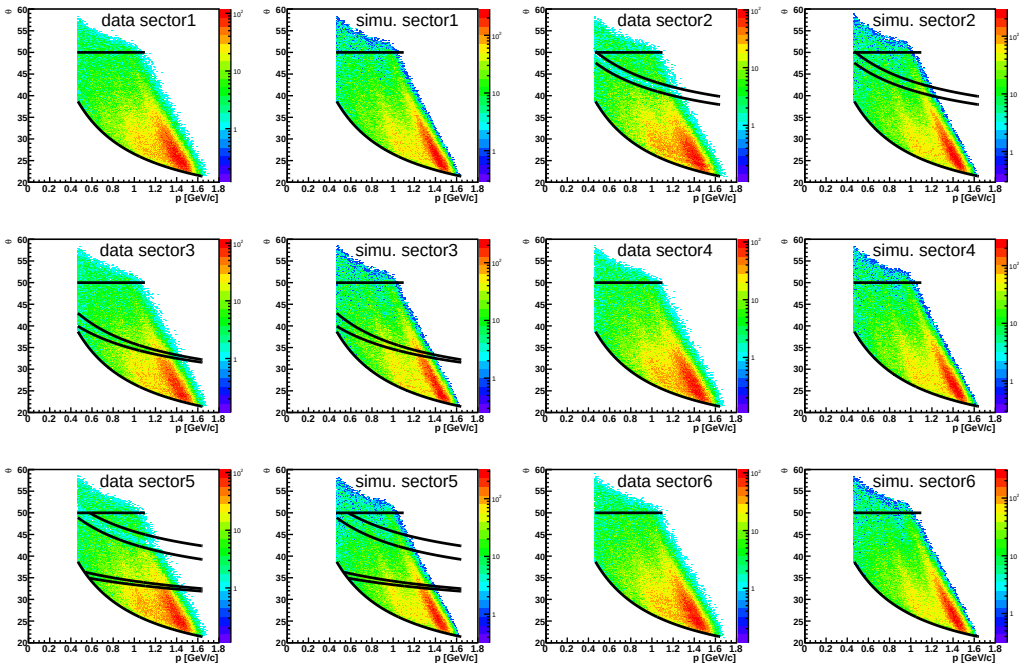

Figure 3.22: θ_e versus p distributions of electrons in all six sectors are compared for experiment (left) and simulation (right) reconstructed data simultaneously each side by side. The top and bottom black lines show the θ_e cut boundaries, and the middle paired black lines show removed regions, which are reflected in Fig. 3.20 by the low event-rate bands.

where all parameters are shown in Fig. 3.23a, and the plateau region of the trapezoid between parameters P_0 and P_1 is accepted by the fiducial cut. Every sector with each momentum and θ bin has its own plateau ϕ region, and the corresponding fit parameters P_0 and P_1 are plotted as boundaries of the θ versus ϕ distribution (see Fig. 3.23b) and fit by modified exponential functions

$$\begin{aligned} \phi_{\pi^-}^{max} &= C_{0max}(1 - e^{-C_1(\theta+C_2)}) + (\text{sector} - 1) * 60, \text{ and} \\ \phi_{\pi^-}^{min} &= C_{0min}(1 + e^{-C_1(\theta+C_2)}) + (\text{sector} - 1) * 60, \end{aligned} \tag{3.19}$$

where C_1 is a constant fit parameter, however C_{0max}, C_{0min}, and C_2 are π^- momentum (p_{π^-}) dependent parameters. In each $\Delta p_{\pi^-} = 0.2$ GeV interval, the corresponding C_{0max}, C_{0min}, and C_2 are obtained, then the C_{0max}, C_{0min}, and C_2 versus p_{π^-} plots

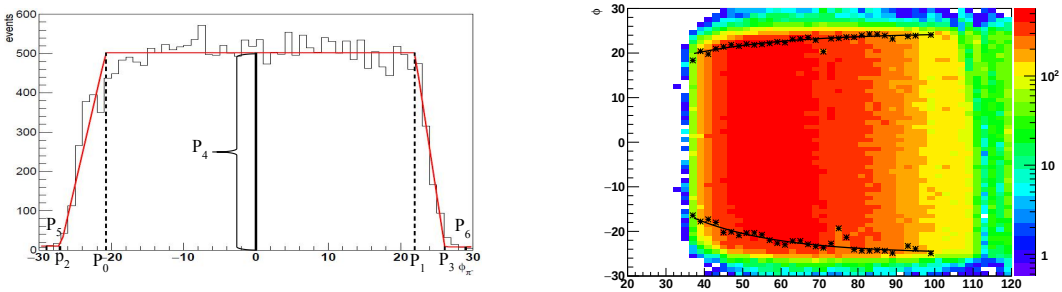

(a) (b)

Figure 3.23: (a) Typical example ϕ distribution of pions from the 0.2 GeV $< |\vec{p}_{\pi^-}| <$ 0.4 GeV and 28° $< \theta_{\pi^-} <$ 30° intervals in sector 1, which are fit by the function (Eq. (3.18)) shown by the red line, where the corresponding fit parameters P_4, P_5, and P_6 are heights of the corresponding plateau regions of the trapezoid function and P_0, P_1, P_2, and P_3 are corresponding ϕ values of the inflection points. (b) Example ϕ versus θ distribution for pions in sector 1 within the same momentum interval. Corresponding fit parameters P_0 and P_1 of each θ bin are marked as stars and fit by the function (Eq. (3.19)) shown by the back line.

are created and fit by

$$C_{0max;\,0min;\,2}(p_{\pi^-}) = par[0] + par[1]P_{\pi^-} + \frac{par[2]}{p_{\pi^-}}, \tag{3.20}$$

where the corresponding fit parameters $par[0]$, $par[1]$, and $par[2]$, along with C_1, are all listed in Tab. A.6 of the Appendix A. $\phi_{\pi^-}^{max}$ and $\phi_{\pi^-}^{min}$ for sector 1 are plotted as two blue curves on the ϕ versus θ distributions in different p_{π^-} intervals, which are shown in Fig. 3.24. Finally, in order to check if those fiducial cuts work properly for both experiment and simulation reconstructed data, they are plotted on example ϕ versus θ distributions side by side for sector 1 in Fig. 3.25. Besides applying $\phi_{\pi^-}^{min} < \phi_{\pi^-} < \phi_{\pi^-}^{max}$ on experiment and simulation reconstructed data, $\theta > \theta_{min}^{\pi^-}$ cuts are also applied. $\theta_{min}^{\pi^-}$ is found empirically from θ versus p distributions in Fig. 3.26 by

$$\theta_{min}^{\pi^-} = 11.09 + \frac{8.0}{0.472p_{\pi^-} + 0.117}, \tag{3.21}$$

which is represented by the black vertical lines in Fig. 3.25.

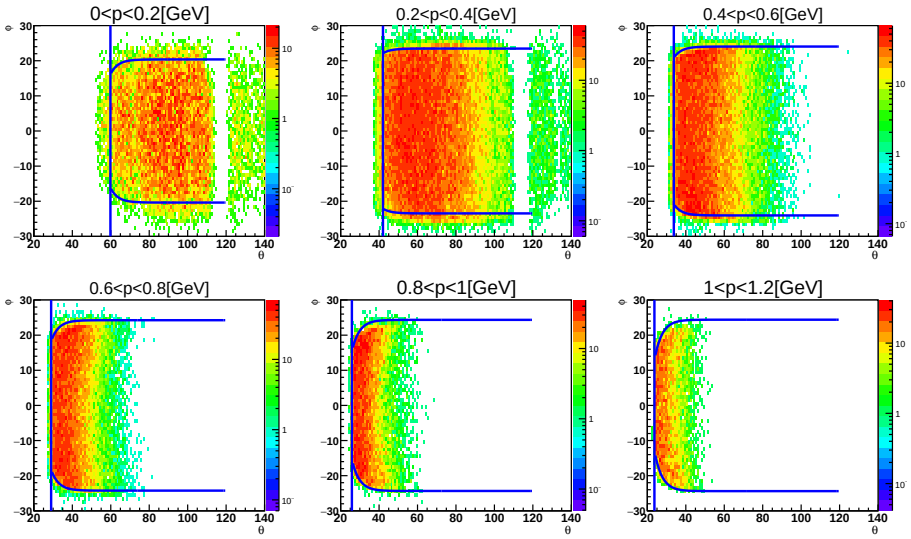

Figure 3.24: Example ϕ versus θ distributions of pions after event selection in sector 1 for 0.2 GeV $< p_{\pi^-} <$ 1.2 GeV within 0.2 GeV increasing steps, and the fiducial cuts (blue lines) are plotted here for sector 1.

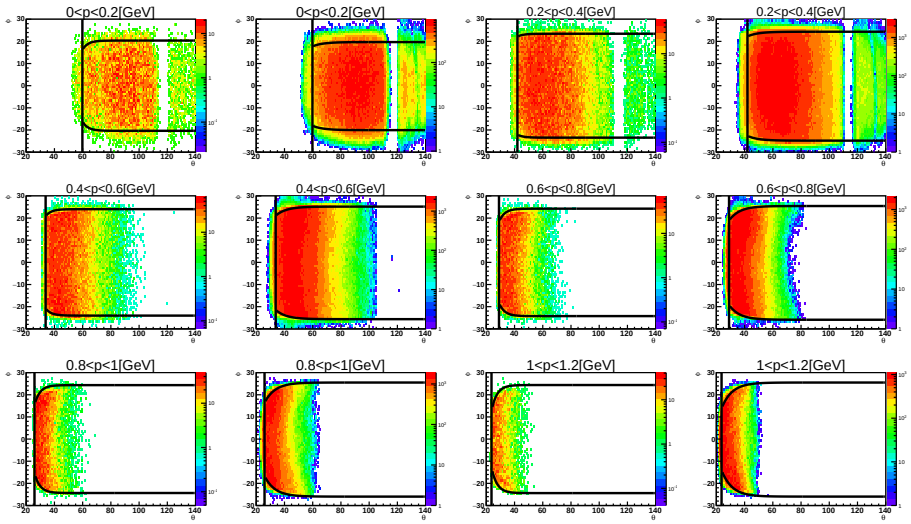

Figure 3.25: ϕ versus θ distributions of pions in different p_{π^-} bins after event selection are plotted for sector 1 for experiment (left) and simulation (right) reconstructed data each side by side. The black lines represent the fiducial-cut boundaries.

The Pion Polar Angle (θ) versus Momentum (p) Cut

Like in case of electrons, we have to remove low-efficient regions of the detector for pions by applying cuts on θ versus p distributions, which are shown in Fig. 3.26 by paired black lines for both experiment and simulation reconstructed data. For pions,

the low efficient regions for all sectors only show up in experiment reconstructed data rather than in the simulation reconstructed data, nevertheless they are cut out for both experiment and simulation reconstructed data. The cut functions are found empirically by

$$\theta = \begin{cases} C_0 + \frac{C_1}{C_2(p+C_3)+C_4} & \text{, sector 1, 3, 4, 5, and 6} \\ C_0 + \frac{C_1}{C_2 p+C_3} & \text{, sector 2,} \end{cases} \tag{3.22}$$

where all parameters are listed in Tab. A.1 of the Appendix A.

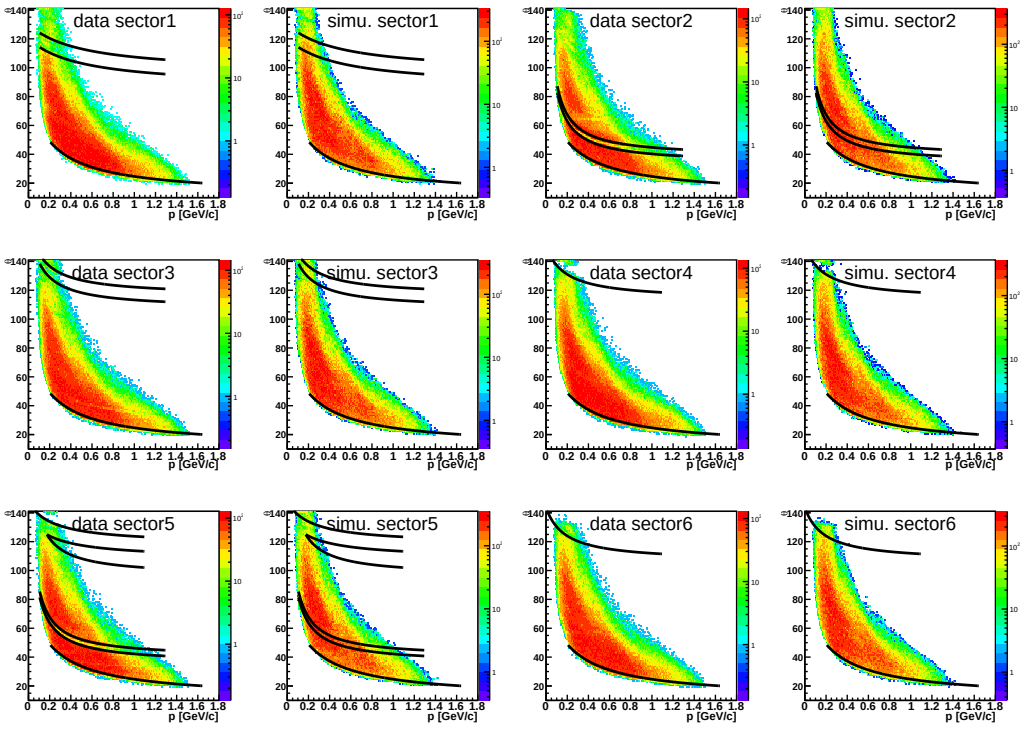

Figure 3.26: θ versus p distributions of pions in six sectors are compared for experiment (left) and simulation (right) reconstructed data each side by side. The middle paired black lines show the removed regions, which are reflected in Fig. 3.25 by the vertical low event-rate bands, and the bottom black lines represent $\theta > \theta^{\pi^-}_{min}$ cuts .

3.9 Proton Fiducial Cuts

For the proton fiducial cut, we follow the same procedure as for other particles to only accept stable efficiency regions of the detector. We apply the following cuts on

both experimental data and simulation.

The Proton ϕ versus θ Cut

We plot the proton ϕ versus θ distributions in different momentum bins for each sector, see examples in Fig. 3.28. A typical projected ϕ distribution for the $28° < \theta_{proton} < 30°$ bin is shown in Fig. 3.27a, which is fit by the function Eq. (3.18) to get the corresponding fit parameters P_0 and P_1. They are marked as stars in Fig. 3.27b and are fit by the functions ϕ^{max}_{proton} and ϕ^{min}_{proton} given by Eq. (3.23) to establish the fiducial-cut boundaries for protons. The fit parameters are momentum independent but different for different sectors (see this behavior in Fig. 3.28). All parameters are listed in Tab. A.7 in the Appendix A.

$$\begin{aligned} \phi^{max}_{proton} &= P_0(1 - e^{-P_1(\theta+P_2)}) + (\text{sector} - 1) * 60 \\ \phi^{min}_{proton} &= P_0(1 + e^{-P_1(\theta+P_2)}) + (\text{sector} - 1) * 60 \end{aligned} \tag{3.23}$$

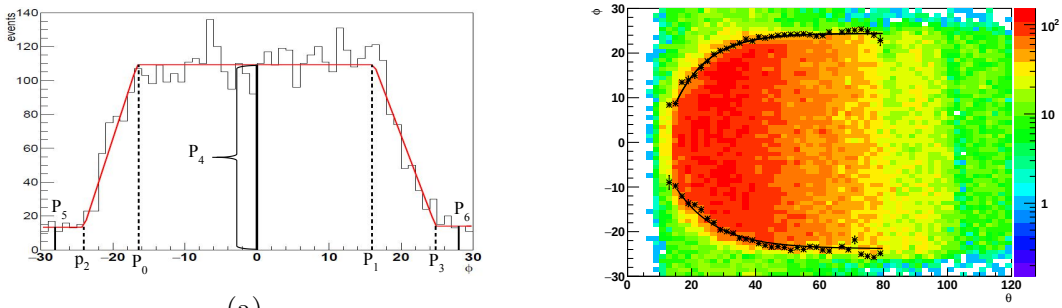

(a) (b)

Figure 3.27: (a) Typical example for a ϕ distribution of protons from the 0.2 GeV $< |\vec{p}_{proton}| <$ 0.4 GeV and $28° < \theta_{proton} < 30°$ intervals in sector 1, which is fit by the function Eq. (3.18) and plotted as the red line. The corresponding fit parameters P_4, P_5, and P_6 are heights of the corresponding plateau regions of the trapezoid function, and P_0, P_1, P_2, and P_3 are the corresponding ϕ values of the inflection points. (b) The ϕ versus θ distribution of protons for sector 1 within the same momentum interval. Corresponding fit parameters P_0 and P_1 of each θ bin are marked as stars, fit by the function Eq. (3.19), and shown by the black lines.

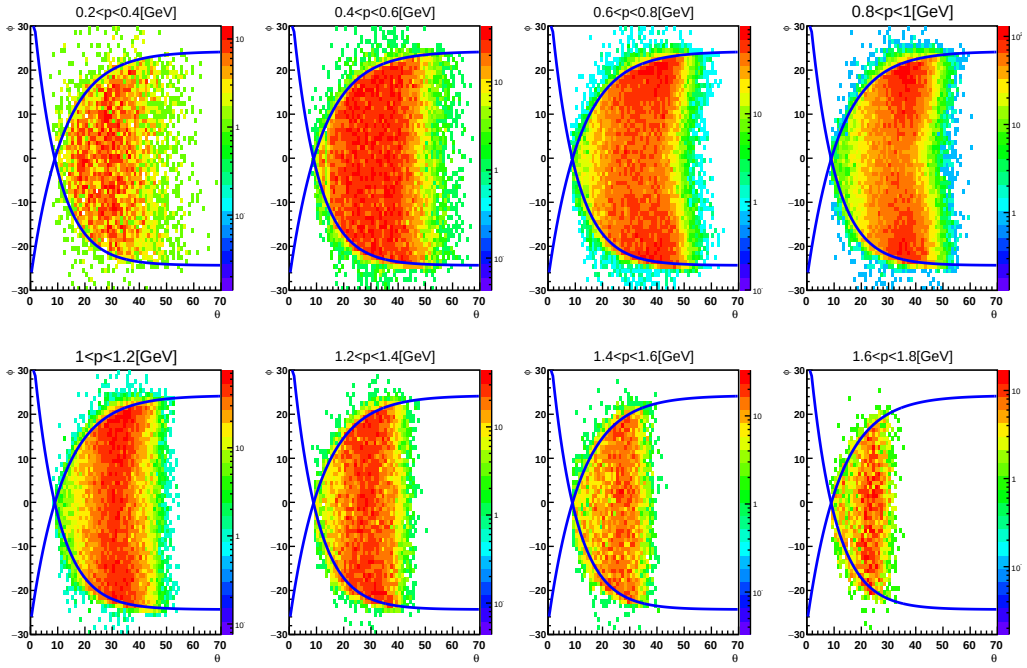

Figure 3.28: Example ϕ versus θ distributions for protons in sector 1 for 0.2 GeV $< p_{proton} <$ 1.8 GeV within 0.2 GeV increasing steps and the fiducial cuts (blue lines) for sector 1.

In Fig. 3.29, the proton fiducial-cut boundaries ϕ^{max}_{proton} and ϕ^{min}_{proton} are plotted as ϕ versus θ distributions for experiment and simulation reconstructed data to conclude that they include all the stable efficiency regions for both.

The Proton Polar Angle (θ) versus Momentum (p) Cut

For protons, we only cut out the low efficient regions of sector 2 and 5, which are visible in Fig. 3.30, where the cut functions are found empirically by

$$\theta = \begin{cases} C_0 p^3 + C_1 p^2 + C_2 p + C_3 & , \text{ sector 2} \\ C_0 (p + C_1)^{C_2} + C_3 & , \text{ sector} 5 - 1 \\ C_0 (p + C_4)^3 + C_1 (p + C_4)^2 + C_2 * (p + C_4) + C_3 & , \text{ sector} 5 - 2, \end{cases} \tag{3.24}$$

and for which all fit parameters are listed in Tab. A.2 in the Appendix A.

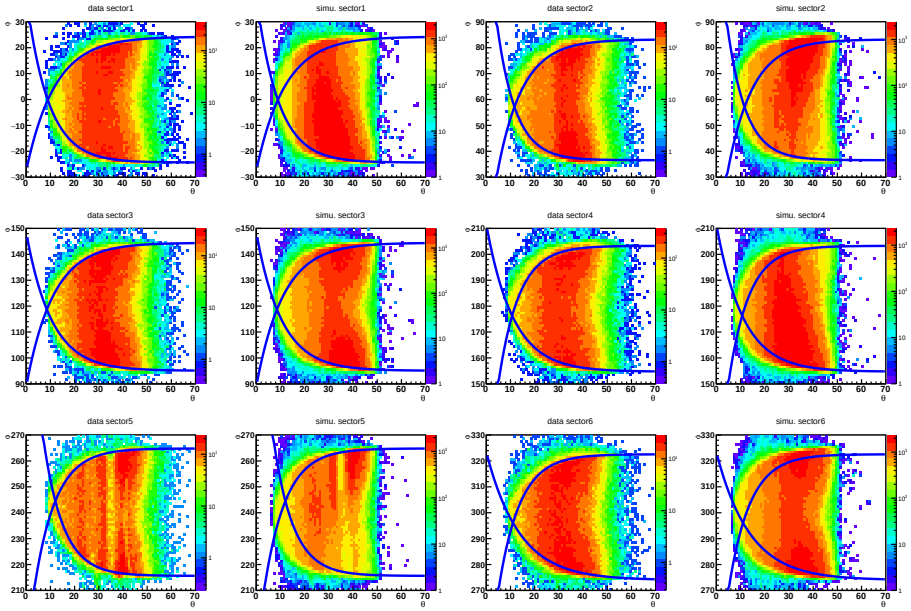

Figure 3.29: ϕ versus θ distributions of protons plotted for six sectors for experimental experiment (left) and simulation (right) reconstructed data each side by side. The blue lines represent fiducial-cut boundaries.

3.10 Event Selection

With the saved information of all but one final state particles ($e^{'}$, π^{-}, and p) and the deuteron (D) at rest in the lab frame, we finally select and analyze events for the reaction $\gamma^{*}n\,(p) \rightarrow p\pi^{-}\,(p)$ by applying the following cuts.

Exclusive Events Selection

For events that have reconstructed four momenta for $e^{'}$, π^{-}, and p, we calculate the missing "spectator" mass squared M_s^2, which is determined by

$$M_s^2 = (P_e^{\mu} - P_{e'}^{\mu} + P_D^{\mu} - P_{\pi^-}^{\mu} - P_p^{\mu})^2, \tag{3.25}$$

where P_e^{μ}, $P_{e'}^{\mu}$, P_D^{μ}, $P_{\pi^-}^{\mu}$, and P_p^{μ} are the four momenta of the corresponding particles. In order to select the exclusive process $\gamma^{*}n\,(p) \rightarrow p\pi^{-}\,(p)$, we apply the 0.811 GeV^2 $< M_s^2 <$ 0.955 GeV^2 missing mass cut to isolate the "spectator" proton peak (see

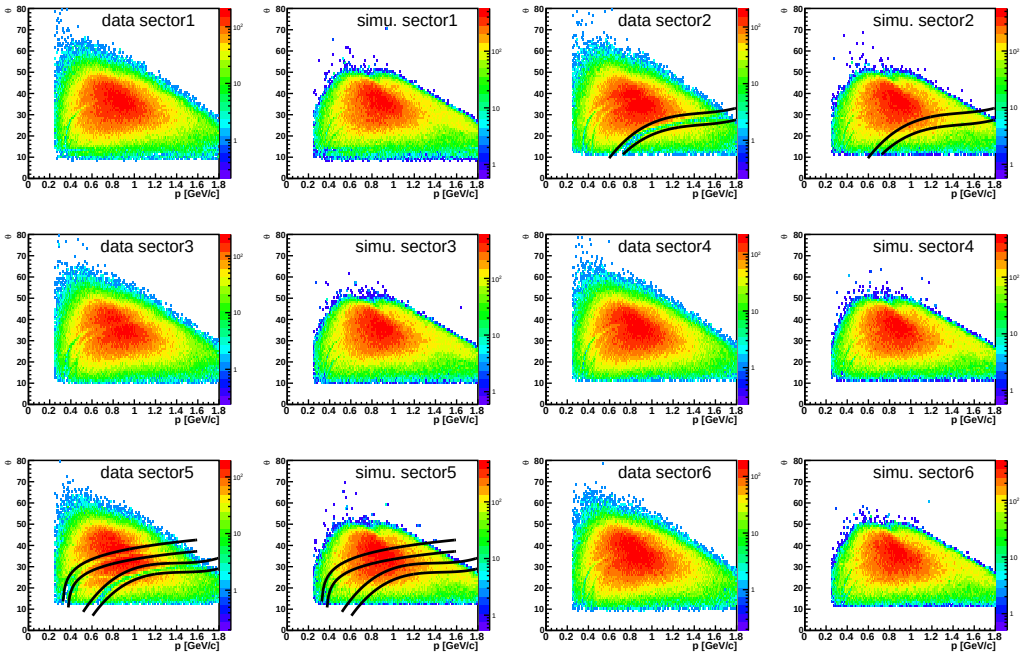

Figure 3.30: θ versus p distributions of protons in all six sectors are compared for experimental (left) and simulation (right) reconstructed data each side by side. The middle paired black lines show the removed regions, which are reflected in Fig. 3.29 by the vertical low event-rate bands.

Fig. 3.31), which should be around the proton rest mass squared (~ 0.88 GeV^2).

Quasi-free Exclusive Events Selection

Based on the exclusive events, we apply an additional cut on the missing momentum of the "spectator" ($|\vec{p_s}|$) for both experiment and simulation reconstructed data, which is shown in Fig. 3.33a. $|\vec{P}_s|$ is calculated by

$$|\vec{P}_s| = | \vec{P}_e - \vec{P_e}' - \vec{P_{\pi^-}} - \vec{P}_p | \ . \tag{3.26}$$

The zoomed in Fig. 3.33b focuses on the low "spectator" momentum distribution (black line) for experimental data and the detector-reconstructed Monte Carlo (MC) simulated proton Fermi momentum distribution with the CD-Bonn potential (blue line) [28]. The comparison between the two curves reveals that the quasi-free process is absolutely dominant in the $|\vec{P}_s| < 200$ MeV region. When $|\vec{P}_s| > 200$ MeV, the final

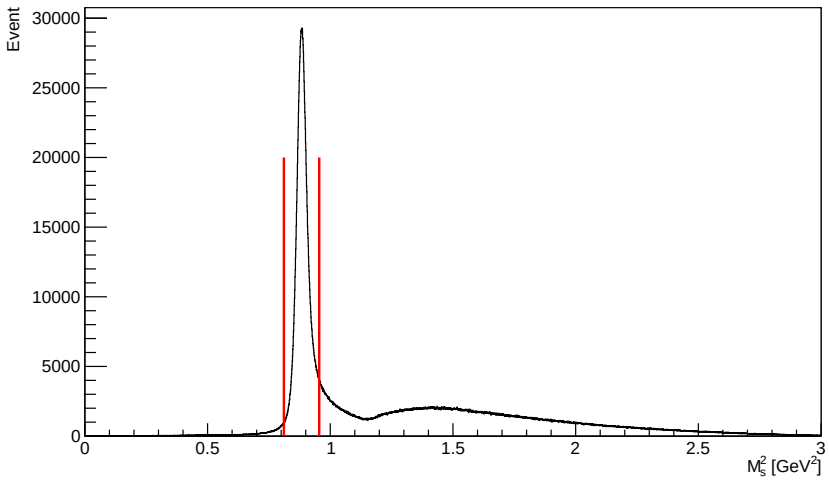

Figure 3.31: The M_s^2 distribution with the two cut limits represented by the red lines illustrates the exclusive event selection process.

state interaction becomes first measurable and then even dominant. Since the $|\vec{P}_s|$ distribution of experimental data is right underneath the simulated Fermi momentum distribution (blue line) up to 200 MeV, we can successfully isolate the quasi-free process by applying this cut, and the assummed "spectator" becomes a true spectator proton. Meanwhile, we also cut away some good quasi-free events with this cut. Here "r" denotes the factor to correct good quasi-free events outside the $|\vec{P}_s|<$ 200 MeV cut. In order to calculate "r", the $|\vec{P}_s|<$ 200 MeV cut is applied to simulated events to get the $|\vec{P}_s|$ distribution for each kinematic bin. Then the factor r is calculated from the simulation reconstructed data by

$$r(W, Q^2, \cos\theta^*_{\pi^-}, \phi^*_{\pi^-}) = \frac{N^{simu-|\vec{P}_s|<200\,\mathrm{MeV}}(W, Q^2, \cos\theta^*_{\pi^-}, \phi^*_{\pi^-})}{N^{simu-qf}(W, Q^2, \cos\theta^*_{\pi^-}, \phi^*_{\pi^-})} = \frac{green}{green + red}, \tag{3.27}$$

where $N^{simu-qf}$ represents simulated exclusive quasi-free yields in each kinematic bin and $N^{simu-|\vec{P}_s|<200\,\mathrm{MeV}}$ corresponds to the simulation yields in each kinematic bin after applying $|\vec{P}_s|<$ 200 MeV cut. The green and red areas are shown in the Fig 3.32 to represent the integral of $|\vec{P}_s|$ distribution below and above the 200 MeV cut individually. Based on the good agreement of the $|\vec{P}_s|$ distribution below 200 MeV

between the experimental data and simulation in Fig. 3.32, the $r(W, Q^2, \cos\theta^*_{\pi^-}, \phi^*_{\pi^-})$ should be the best estimated correction factor for those good quasi-free events lost by the cut.

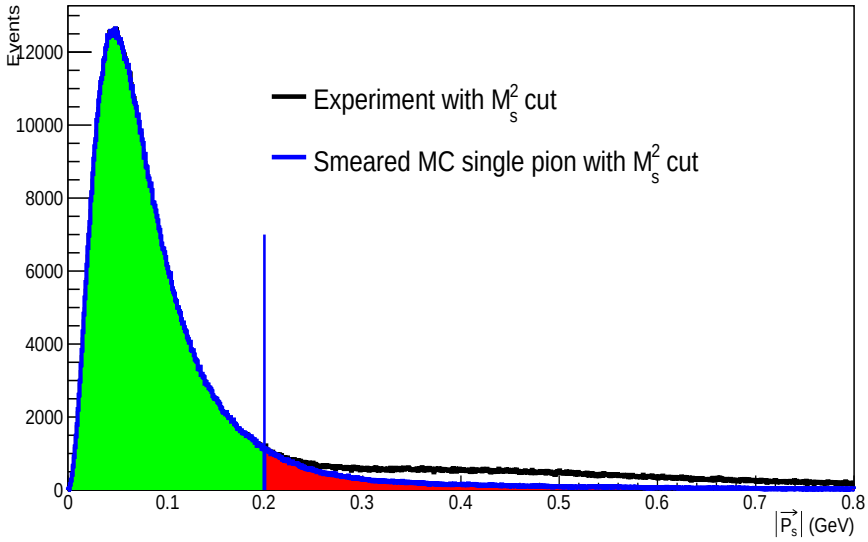

Figure 3.32: (Color online) The $|\vec{P}_s|$ distribution of experimental data (black line) and simulation (blue line) where "green" and "red" filled areas represent the integral of the blue distribution from 0 MeV to 200 MeV and above 200 MeV, respectively.

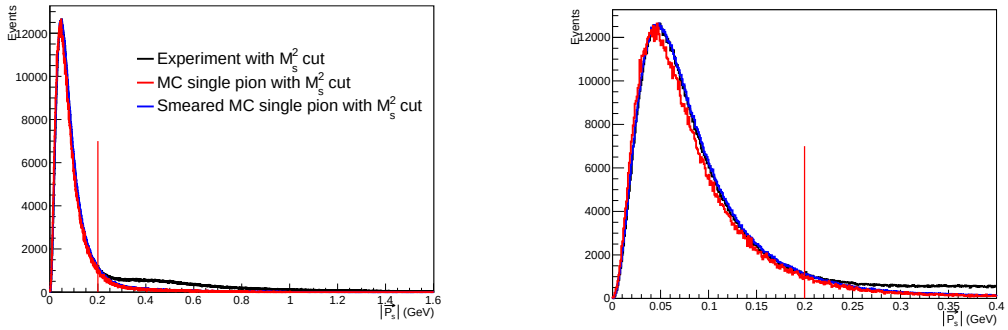

(a) (b)

Figure 3.33: (a)(Color online) The black line represents the missing momentum distribution ($|\vec{P}_s|$) of the unmeasured proton from experimental data. Based on the CD-Bonn potential [28], the Monte Carlo simulated scaled proton momentum distribution leads to the red line and the detector-smeared simulated scaled distribution to the blue line.(b) The zoomed plot of (a) to investigates this comparison clearly.

Chapter 4

Simulation

4.1 Introduction

In order to extract the cross sections for the reaction of interest, we need to have a good understanding of the detector behavior to get precision and accurate estimate of detector efficiency and acceptance. In this way, by correcting the obtained yield for the detector acceptance we can estimate the truly produced reaction yield. So, to obtain the detector acceptance we have to utilize a simulation process as laid out in the flowchart of Fig. 4.1. The details of each simulation step will be discussed in the following sections.

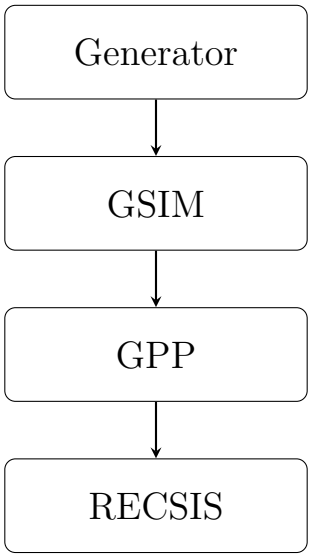

Figure 4.1: Flowchart showing the main steps of the detector and reaction simulation process. $\gamma^* n(p) \rightarrow p\pi^-(p)$ events are generated by a realistic event generator, passed through GSIM [1] and GPP [2], and cooked by RECSIS [3].

4.2 Event Generator

In this analysis, the electromagnetic multipole table [8] of the MAID2000 model [25] is used as an input for the event generator. $en \to e'p\pi^-$ events with radiative effects, according to the prescription of Mo and Tsai [48], are generated by a modified version of the available "*aao_rad*" software package (cvs co *aoo_rad* [9]). Based on the original "*aao_rad*" package, for each generated $en \to e'p\pi^-$ event, the initial neutron mass is set to the neutron rest mass and an additional proton is added as the output particle. This proton is generated based on the Fermi momentum from the CD-Bonn potential [28] and the rest proton mass. In this way, the generated proton is not change kinematics in the scattering process and behaves like a spectator (p_s). It is, along with e', p, and π^-, reconstructed through the full simulation procedure, which is the same as the reconstruction procedure applied to the experimental data. After adding the "spectator" proton in the event generator, the simulated physics process is the same as the exclusive quasi-free process of the experimental data.

Besides the MAID2000 version, there are MAID98, MAID2003, and MAID2007 versions [26] also available in the "*aao_rad*" package. In order to determine which version describes the experimental data best, we compare the $W(W = W_f)$ and Q^2 distributions of the quasi-free exclusive events between different MAID versions and the data, as shown in Fig. 4.2a and Fig. 4.2b. The comparison of these W distributions shows that the MAID2000 version yields resonance peak positions that are closest to the data. The MAID2007 is the latest version, but the second resonance peak of that version is shifted relative to the experimental data. About 8 billion events were generated to cover the entire kinematic range listed in the Tab. 5.1 and a little bit beyond the range to account for resolution and bin migration effects for a total of 8640 kinematic bins.

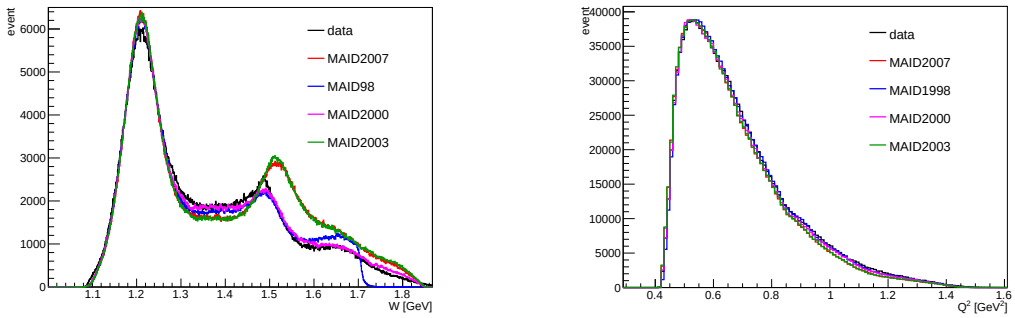

(a) (b)

Figure 4.2: (a) W distributions of exclusive quasi-free events of experimental data (black) and the corresponding simulated distribution for the MAID98 (blue), MAID2000 (magenta), MAID2003 (green), and MAID2007 (red) versions. (b) Q^2 distributions for the experimental events and the corresponding simulatied events of (a).

4.3 GSIM

After generating the physics events of interest, the propagation of the final state particles through the CLAS detector is simulated. The available simulation package based on GEANT 3 libraries (developed at CERN) of the CLAS collaboration, GSIM [1], propagates each of the particles through all CLAS detector components from the vertex produced by the event generator and provides the detector response in terms of raw signals (TDC and ADC) as does the actual CLAS detector. The GSIM-specific format-free read ("ffread card" [10]) is used as the configuration file of GSIM to configure which modules will be used in the simulation, which includes the following information for its command line option [5]:

- energy cut-off in GEANT for various particles in various parts of the detector,
- geometry of the detector,
- magnetic field of the detector,
- target material and geometry, and

- beam position.

The configuration file of GSIM listed in the reference [5] is used and adapted for this work only.

4.4 GPP

Although the GSIM simulation package includes all of the detector geometry and properties, it still overestimates the resolution of the drift chambers and SC system. So the GSIM Post Processor (GPP [2]) program is used to better match the resolution between experimental and simulation data, i.e. better agreement on the ΔT, M_s^2, and $|\vec{P}_s|$ distributions of experimental and simulation data, which influence the results on the event selection level. There are two quantities to be adjusted in the GPP process. One is the DC smearing factor, which influences the tracking resolution, and the other is the SC smearing factor that adjusts timing resolution. Since experimental conditions may change by run, for the "e1e" run, we have to find a new set of corresponding GPP smearing constants. For GPP parameter setting, we need to determine the run number (R), the DC smearing scale factor for regions 1, 2, and 3 (a, b, and c), and the SC smearing scale factor (f). R should be set to any run number belonging to the "e1e" run experimental data set in order to access the correct calibration constants in the calibration database. Assuming DC regions 1, 2, and 3 had identical resolutions, the same value is set for a, b, and c. We generated about 2 million electron-neutron exclusive quasi-free $p\pi$ interaction events for each $a = b = c$ and f combination to pass through the flowchart in Fig. 4.1. The quantity t_0 (Eq. (3.9)) is measured to set the start time of each reconstructed event, which is used to calculate ΔT for the hadron identification. So we can use it to determine the right value of f. For the simulation events, we set $a = b = c = 2.5$ initially, which is consistent with the "e1e" hydrogen target analysis [2]. Then by gradually changing the "f" values one obtains the Gaussian fitted σ values of the corresponding

t_0 distributions. In Fig. 6.11, these σ values are presented by black points, which are fit by a linear function. In this way, we get $f = 0.9$ to match best the fitted σ value of the experimental data. In Fig. 6.10, the Gaussian fitted parameters σ show that the t_0 distribution of experimental data and simulation have the same timing resolution by setting GPP parameters $a = b = c = 2.5$ and $f = 0.9$.

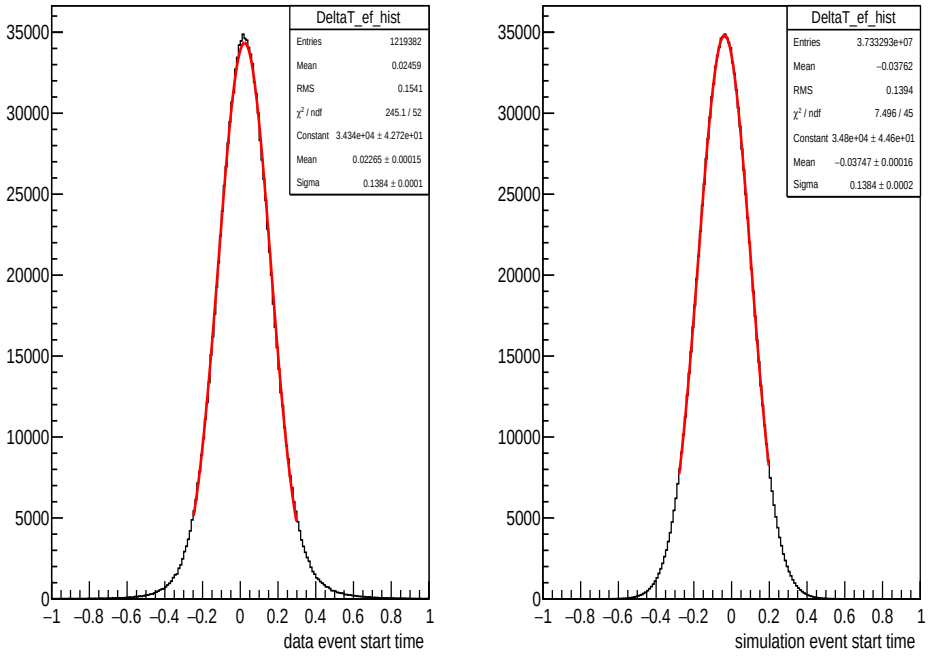

Figure 4.3: Event start time (t_0) distributions of the exclusive quasi-free events for experimental data (left) and simulation with smearing factor f=0.9 (right) are fit by Gaussian functions (red curves). The corresponding fit parameters are listed in the statistic boxes, respectively.

The discrepancy between experiment and simulation reconstructed data of the "spectator" missing mass (M_s^2) distribution, which can later influence our results, reflects the difference in the drift chamber resolution between experiment and simulation reconstructed data. Similar to the SC smearing factor determination, we fixed the parameter $f = 0.9$ and changed $a = b = c$ parameters gradually for the simulation events. In Fig. 4.5, the Gaussian fitted σ values of M_s^2 distributions corresponding to different $a = b = c$ values are plotted as black points and are fit by a linear function.

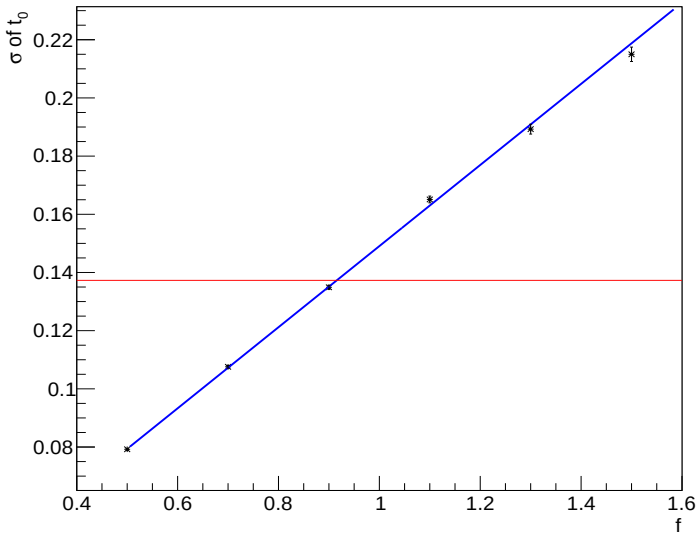

Figure 4.4: The σ of t_0 versus f from the simulation events are fit by a linear function (blue), and the red line corresponds to the the σ of t_0 from the measured exclusive quasi-free events. The f value corresponding to the cross point is used to smear the simulated detector SC resolution.

From the fitted linear function, we finally set the smearing parameters $a = b = c = 2.5$ for the simulation events, which smear the drift chambers resolution of the simulation in the same way as the experiment does. We plot the M_s^2 distributions of the simulation reconstructed events with GPP parameters $f = 0.9$ and $a = b = c = 2.5$ and the experimental reconstructed events in Fig. 6.9, and their Gaussian fitted parameters σ are equal to each other at $\sigma = 0.01978$, which shows the GPP parameters are under control for this analysis.

4.5 RECSIS

After the generated physics events are processed through GSIM and GPP, the outputs of GPP still contain ADC and TDC hit information for each detector component. Then the output files must be processed with the same reconstruction software (RECSIS) that is used for the experimental raw data. Certain modifications however were implemented in the processing of simulated data [3]. After the processing, the

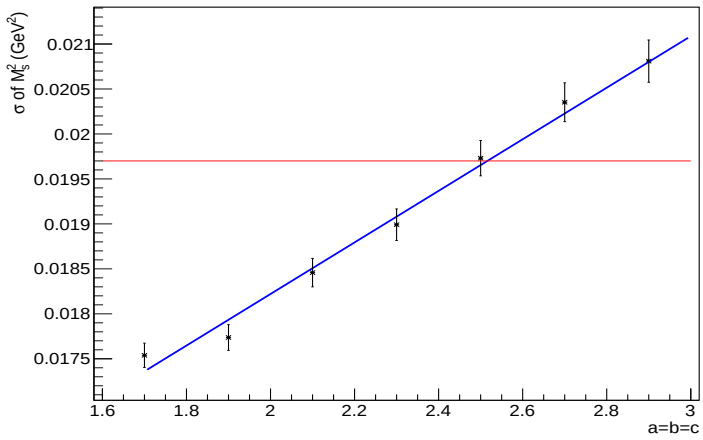

Figure 4.5: The fitted σ values of M_s^2 distributions depending on different $a = b = c$ values are plotted as black points. These are fit by a linear function (blue). The red horizontal line represents the fitted σ values of M_s^2 distributions from the experimental reconstructed events. The value of $a = b = c$ corresponding to the cross point is used to smear the simulated detector DC resolution.

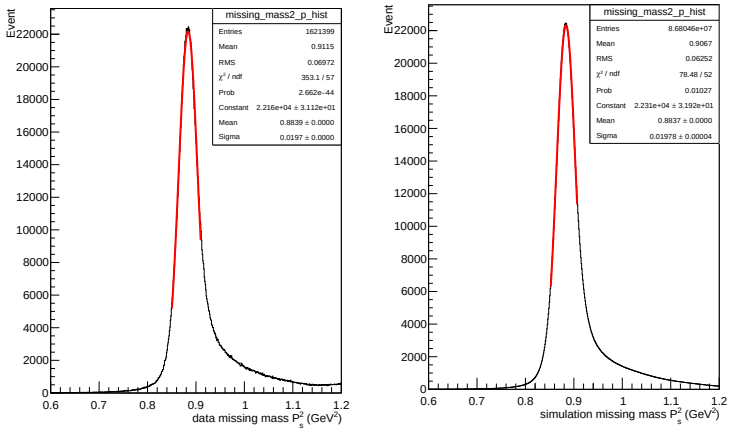

Figure 4.6: The M_s^2 distributions of the exclusive quasi-free events for experimental data (left) and simulation with smearing factors $f = 0.9$ and $a = b = c = 2.5$ (right) are fit by Gaussian functions (red). The corresponding fit parameters are shown in their statistics legend boxes.

simulated events are analyzed similarly to the experimental events and are used to obtain the acceptance corrections, which are then applied to the experimental yield to extract the $\gamma^* n(p) \to p\pi^-(p)$ cross sections. All the details are discussed in the following chapters.

Chapter 5

Corrections and Normalization

The simulated events are used to obtain the acceptance corrections, and the cross section function of the MAID model is used to calculate the bin centering corrections, both of which are applied to the final cross sections calculation. Since we present the final cross sections in the kinematic variable W_f, the radiative effects can only influence the variable Q^2. As a cross check, in Fig. 1.4 of Chapter 1, the radiative corrected W_i distribution, where W_i is calculated by setting M_n by Eq. (1.20) of n^μ, is consistent with the W_f distribution. For this work, the radiative effects are marginal compared to the systematic uncertainties. In addition to these corrections, we also check for consistency of the experimental data with other known cross sections, such as inclusive cross section of the process $eD \to eX$. All details of those procedures will be discussed in the following sections.

5.1 Kinematic Binning

In Chapter 1, we introduced the kinematic variables $W = W_f$, Q^2, $\cos\theta^*_\pi$, and ϕ^*_π in which we present the final cross sections. The range of each kinematic variable is determined by the kinematic nature of the data, and the bin size is needed to be chosen as fine as possible to address the structure of the cross section; meanwhile we also need to minimize the statistical uncertainties to guarantee enough statistics in each kinematic bin. One possible binning solution is listed in Table 5.1 and is illustrated in Fig. 5.1 for W range covering the Δ resonance, the second resonance, and the third resonance regions. W coverage is narrower at higher Q^2 due to the

kinematic limitations.

Table 5.1: W and Q^2 binning of the analysis.

Variable	Lower limit	Upper limit	Number of bins	Bin size
W, GeV	1.1	1.9	32	0.025 GeV
Q^2, GeV^2	0.4	1.0	3	0.2 GeV^2

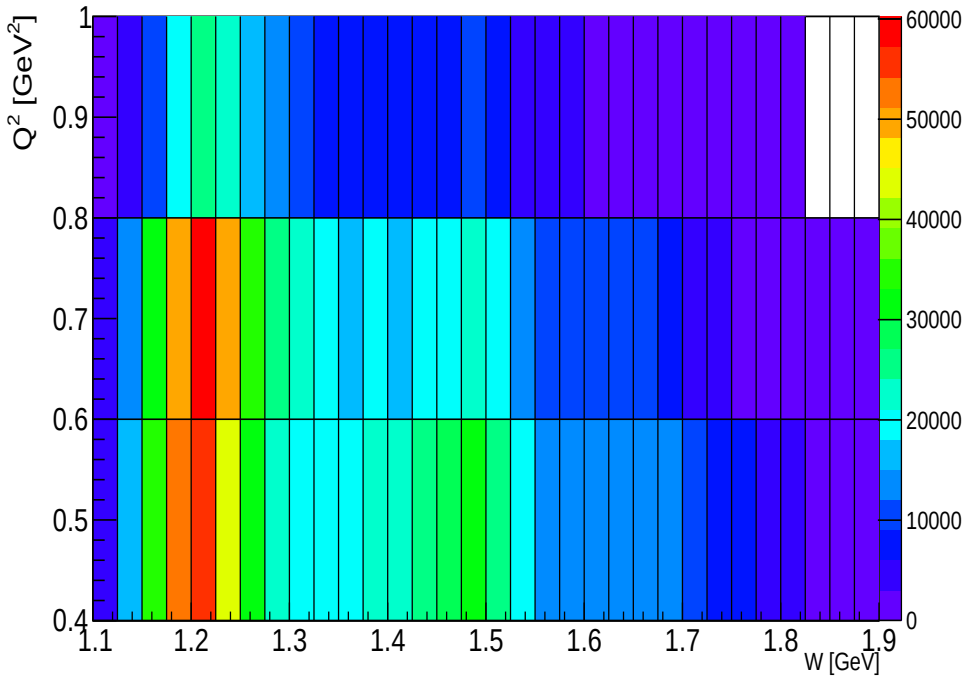

Figure 5.1: W and Q^2 binning for the π^- electroproduction events, where vertical and horizontal lines are shown as the lower and upper corresponding bin limits.

We observe the highest statistics in 1.2 GeV $< W <$ 1.225 GeV and 0.4 GeV^2 $< Q^2 <$ 0.6 GeV^2 bin in Fig. 5.1. We show an example distribution corresponding to $\cos\theta^*$ versus ϕ^* distribution with ϕ^* binned in 9 bins in Fig. 5.2. Due to the low π^- detector acceptance, even in this highest statistics W and Q^2 bin, there are empty kinematic phase space cells in the very forward and the very backward $\phi^*_{\pi^-}$ angles. We tried to enlarge the bin width of the variable $\phi^*_{\pi^-}$, different choices are presented in the Table 5.2. However, this method does not solve the empty cells problem except by increasing the number data points to help the cross section fitting process and

serve as consistency check. In order to get the proper cross section ϕ^* dependence behavior, three sets of ϕ^* bins are finally chosen. These are listed in Tab. 5.2.

Table 5.2: $\cos\theta^*_{\pi^-}$ and $\phi^*_{\pi^-}$ binning of the analysis.

Variable	Lower limit	Upper limit	Number of bins	Bin size
$\cos\theta^*_{\pi^-}$	-1	1	10	0.2
$\phi^*_{\pi^-}$	0°	360°	9	40°
$\phi^*_{\pi^-}$	0°	360°	8	45°
$\phi^*_{\pi^-}$	0°	360°	6	60°

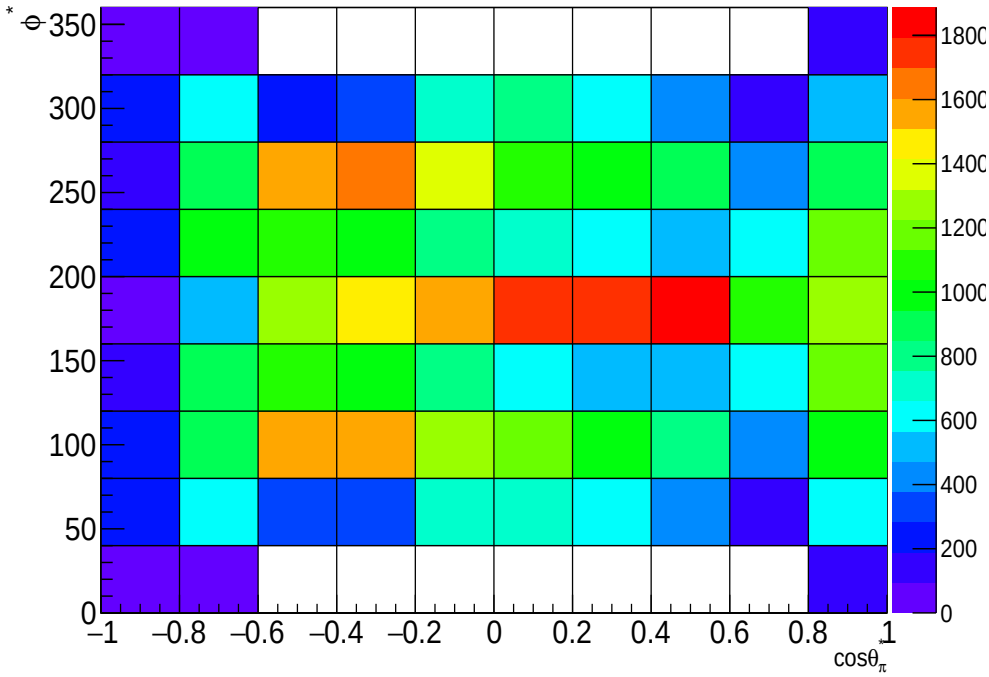

Figure 5.2: Example $\cos\theta^*$ and ϕ^* binning for the π^- electroproduction events in 1.2 GeV $< W <$ 1.225 GeV and 0.4 GeV^2 $< Q^2 <$ 0.6 GeV^2 bin, where vertical and horizontal lines show the lower and the upper bin limits.

5.2 Bin Centering Corrections

The kinematic variables bin-size compromise with our bin-size setting discussed above reveals nicely that the cross section might vary significantly within each kinematic bin. In fact, the extracted cross section $\frac{d\sigma}{d\Omega^*_{\pi^-}}$ is an average value for each 4 dimensional

$(W, Q^2, \cos\theta^*, \phi^*)$ bin. Because of the possibly non-linear behavior of the cross section within a bin, the average cross-section value does not necessarily correspond to the center of the bin. So presenting the final cross section at the center of the bin may not be accurate. To account for such an error, a correction is applied to the cross sections for each 4 dimensional $(W, Q^2, \cos\theta^*, \phi^*\pi^-)$ bin. This bin-centering correction (R_{BC}) is calculated as

$$R_{BC}(W, Q^2, \cos\theta^*, \phi^*_{\pi^-}) = \frac{\sigma^{model}_{center}}{\sigma^{model}_{average}}, \tag{5.1}$$

where σ^{model}_{center} is the cross section calculated by using the parameterization function of MAID2000 model at the numerical center of each kinematic bin, and $\sigma^{model}_{average}$ is

$$\sigma^{model}_{average} = \frac{\int_{x_1}^{x_2} \sigma(x) dx}{\Delta W \Delta Q^2 \Delta \cos\theta^* \Delta\phi^*}, \tag{5.2}$$

where x presents the kinematic bin $(W, Q^2, \cos\theta^*, \phi^*)$, x_1 and x_2 are the limits of the bin, and $\sigma(x)$ is the MAID2000 model cross-section function. Figure 5.3 shows R_{BC} as a function of $\cos\theta^*$ and ϕ^* for the example bin at $W = 1.2125$ GeV and $Q^2 = 0.5$ GeV^2.

5.3 Luminosity

Luminosity ($\mathcal{L}$) is the product of the number of incoming beam particles incident on the target per unit area and per unit time and the total number of target particles within the beam cross-sectional area [59]. The cross section of the reaction should be normalized to the integrated luminosity ($\mathcal{L}_{int}$), which is the integral of $\mathcal{L}$ over the time of the whole experiment. Thus, $\mathcal{L}_{int}$ has dimensions of $[area^{-1}]$. It is calculated as

$$\mathcal{L}_{int} = N_e N_d = \left(\frac{Q_{tot}}{e}\right) \times \left(\frac{N_A d_T l_T}{M_d}\right) = 2.6788 \times 10^{39}\ \text{cm}^{-2}, \tag{5.3}$$

where Q_{tot} is the total live time accumulated Faraday cup charge (4.420 mC), which is collected during the entire experiment production period. Furthermore, e is the elementary charge (1.6×10^{-19} C), d_T is the density of the liquid deuterium target

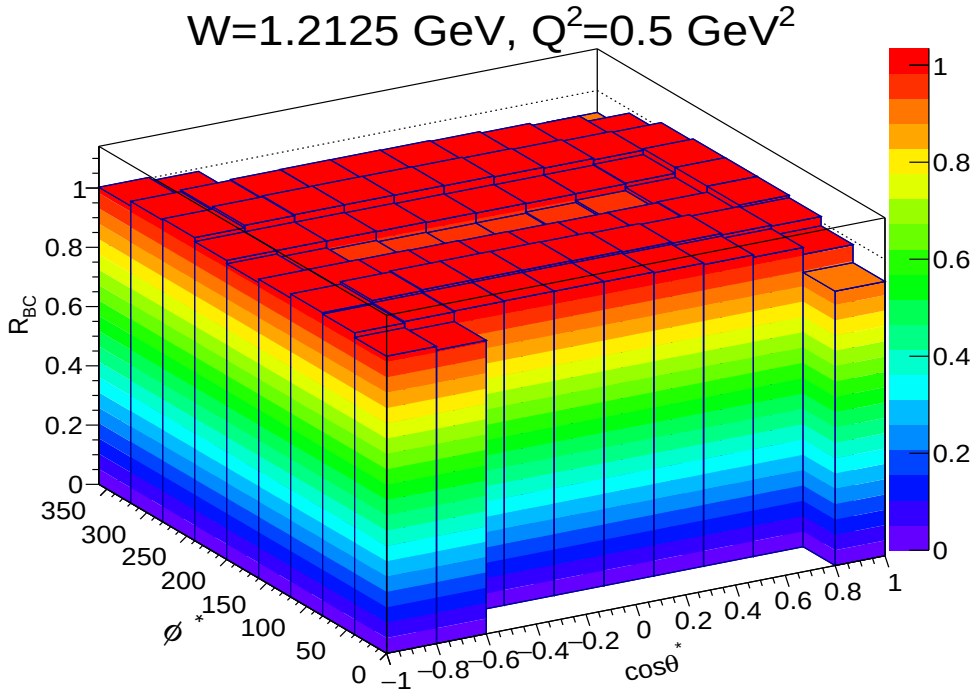

Figure 5.3: Bin centering corrections R_{BC} as a function of $\cos\theta^*$ and ϕ^* in the $W = 1.2125$ GeV and $Q^2 = 0.5$ GeV^2 bin.

(0.1624 g/cm^3, ignoring the temperature and pressure fluctuation of the target system), l_T is the target length (2 cm), N_A is Avogadro's number (6.02×10^{23} mol^{-1}), and M_d is the molar density of deuterium (2.014 g/mol). This value of $\mathcal{L}_{int}$ is used in the Eq. (6.1) to calculate the cross section.

5.4 Empty-Target Background Subtraction

The "e1e" empty-target run numbers are 36597, 36617, 36618, and 36619. These are used to estimate the background originating from the 50 μm-thick Kapton target walls (see Fig. 2.9) and subtract it from the full-target run data. The liquid Deuterium target in those runs was emptied. In order to quantify this background, all events from all empty-target runs are collected, then the same data analysis procedure is applied to those events. Then, the electron z-vertex (Z_e) distributions for full-target and empty-target events are compared as shown in Fig. 5.4a. In the plot, the FWHM

of the full-target Z_e distribution (black) shows that the target is 2-cm long. There is a small peak at 2.58 cm due to the forward foil window (see Fig. 2.9), which should be exactly at the same position for both full-target and empty-target events. This peak can be used to judge the quality of the empty-target background subtraction. We calculate the integrated Faraday cup charge ratio by

$$S_{ratio} = \frac{Q_{total}}{Q_{empty}} = \frac{4.420 \text{ mC}}{0.467 \text{ mC}} = 9.465, \tag{5.4}$$

where Q_{empty} is the total live time accumulated Faraday cup charge for all empty-target runs. Therefore, the empty-target Z_e distribution must be multiplied by S_{ratio} to be compared with the corresponding distribution of the full-target run events. The scaled Z_e distribution of the empty-target (red) in Fig. 5.4a has two peaks for the Kapton cell wall, and one peak at 2.73 cm related to the forward foil, which is slightly shifted from the corresponding peak in the full-target event distribution. The 4 empty-target runs were measured at the end of the "e1e" experiment. During empty-target runs the whole target system is on average warmer than during the full-target runs. The corresponding shift-corrected Z_e distribution of the empty-target (red) is plotted in Fig. 5.4b, where the forward foil peak is now consistent with that of the full-target Z_e distribution. We then subtract the S_{ratio} corrected empty-target Z_e distributions from the full-target Z_e distribution sector by sector. This procedure allows us to check that the 2.73 cm peak is vanished properly after subtracting the empty-target Z_e distribution from that of the full-target, examples are shown in Fig. 5.5. It turns out that the S_{ratio} has been determined correctly and that we can safely use it to subtract the S_{ratio} scaled empty-target from the full-target events in each kinematic bin and to extracted the final cross sections with Eq. (6.1). The absolute amount of this background due to cell walls is less than 1%, and the error of this background correction is absolutely negligible.

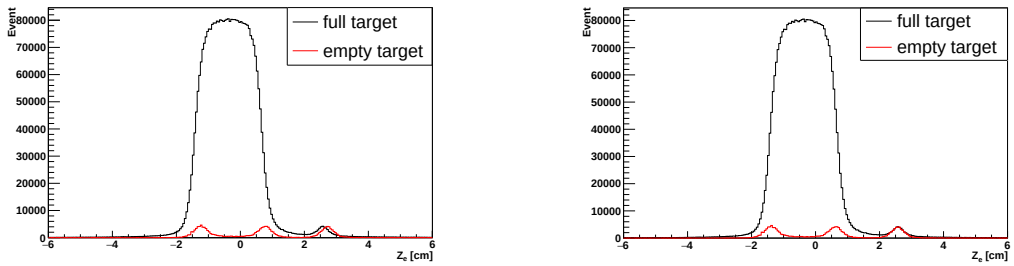

(a) (b)

Figure 5.4: (a) Measured electron vertex (Z_e) distributions for full target events (black) and scaled empty target events (red). (b)The black distribution is kept the same as (a), and the vertex distribution for scaled empty target events is shifted to ($Z_e - 1.5$ mm) (red).

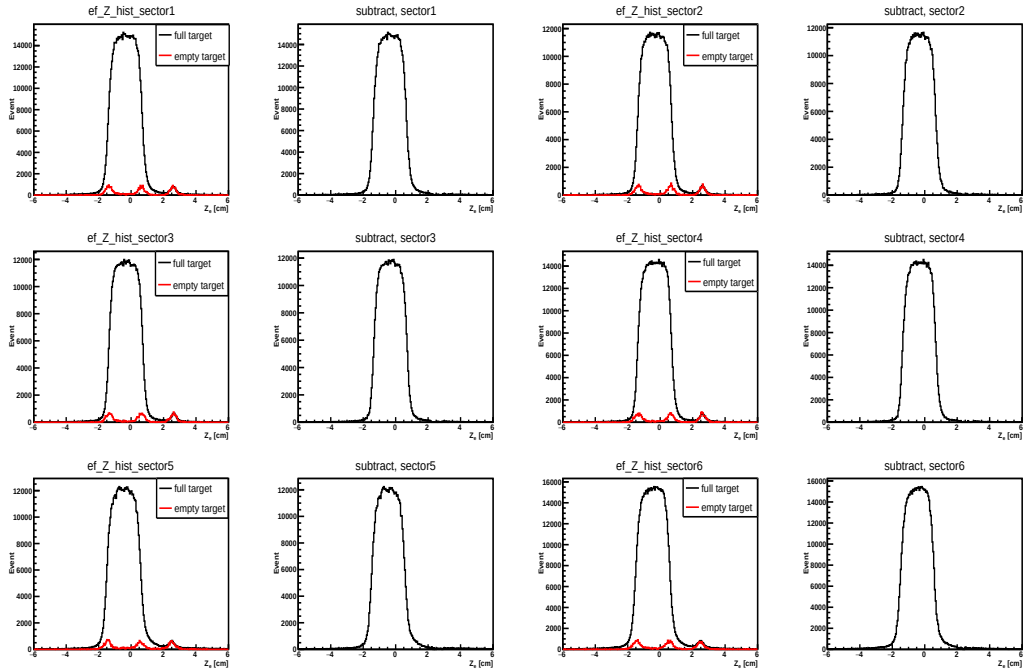

Figure 5.5: Z_e distributions for full-LD_2-target (black) and scaled empty-target events (red) are plotted together in one canvas and compared with these of the empty target subtracted full LD_2 target events sector by sector.

5.5 Acceptance Corrections

Acceptance corrections (A^{Rad}) are calculated using the Monte Carlo simulated events for each 4-dimensional bin as

$$A^{Rad}(W, Q^2, \cos\theta^*, \phi^*) = \frac{N_{rec}^{Rad}(W, Q^2, \cos\theta^*, \phi^*)}{N_{thrown}^{Rad}(W, Q^2, \cos\theta^*, \phi^*)}, \tag{5.5}$$

where $N^{Rad}_{thrown}(W, Q^2, \cos\theta^*, \phi^*)$, known as "thrown events", represents the number of events that are generated by the physics event generator "*aao_rad*" with the MAID2000 model in each kinematic bin radiative effects included. N^{Rad}_{rec} denotes the number of events in the same kinematic bin that have gone through the entire simulation process as shown in Fig. 4.1 and passed all analysis cuts. Those acceptance corrections are applied to obtain the cross sections bin by bin later.

5.6 Radiative Corrections

The $\gamma^* n(p) \to p\pi^-(p)$ process in not the only process contributing to the extracted electroproduction cross section. There are other possible processes (Fig. 5.6) affecting our results by emitting a additional photon. It is impossible to isolate them on the level of the event selection procedure, especially when the energy of the emitted photon is within the detector resolution. So we have to use theory approaches to correct them, which are called radiative corrections. For this analysis, the approach developed by Mo and Tsai [48] is used for correcting the final results. The same amount of $en \to e^{'}p\pi^-$ events with and without radiative effects are generated by the available "*aao_rad*" and "*aao_norad*" software packages [9], respectively, by applying the same electromagnetic multipole table from the MAID2000 model. The radiative correction factor RC is calculated by

$$RC(W, Q^2, \cos\theta^*, \phi^*) = \frac{N^{Rad}_{thrown}(W, Q^2, \cos\theta^*, \phi^*)}{N^{noRad}_{thrown}(W, Q^2, \cos\theta^*, \phi^*)}, \tag{5.6}$$

where $N^{noRad}_{thrown}(W, Q^2, \cos\theta^*, \phi^*)$ known as "thrown events" without radiative effects represents those events that are generated by the physics event generator "*aao_norad*" in each kinematic bin. $N^{Rad}_{thrown}(W, Q^2, \cos\theta^*, \phi^*)$ corresponds to the same quantity used in Eq. (5.5). Finally the RC will be combined with the acceptance corrections factor A^{Rad} Eq. (5.5) to calculated the radiative corrected acceptance A_{RC}, which is

represented by

$$
\begin{aligned}
A_{RC}(W, Q^2, \cos\theta^*, \phi^*) &= A^{Rad}(W, Q^2, \cos\theta^*, \phi^*) RC_{correct}(W, Q^2, \cos\theta^*, \phi^*), \\
&= \frac{N^{Rad}_{rec}(W, Q^2, \cos\theta^*, \phi^*)}{N^{Rad}_{thrown}(W, Q^2, \cos\theta^*, \phi^*)} \frac{N^{Rad}_{thrown}(W, Q^2, \cos\theta^*, \phi^*)}{N^{noRad}_{thrown}(W, Q^2, \cos\theta^*, \phi^*)}, \\
&= \frac{N^{Rad}_{rec}(W, Q^2, \cos\theta^*, \phi^*)}{N^{noRad}_{thrown}(W, Q^2, \cos\theta^*, \phi^*)}.
\end{aligned} \tag{5.7}
$$

This factor is applied to the calculation of the cross sections in the chapter 6, the example is shown in Eq. (6.1).

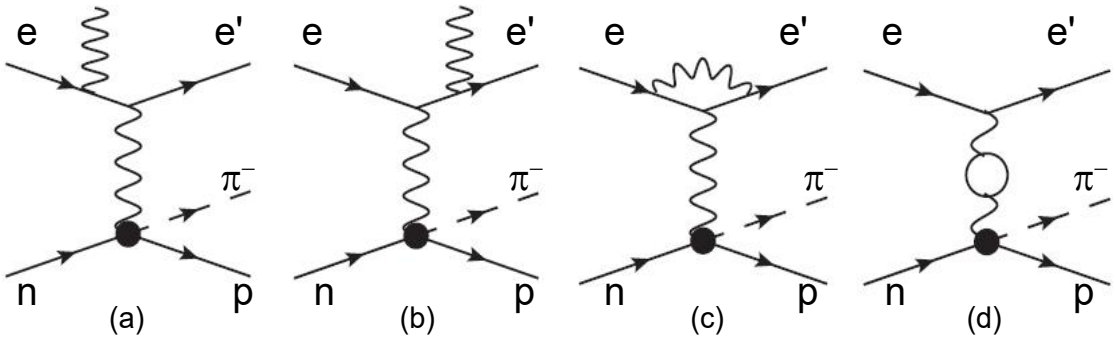

Figure 5.6: Feynman diagrams of the radiative effects in the π^- electroproduction. (a) and (b) Brehmsstrahlung, (c) Vertex correction, and (e) Vacuum polarization, as used by [48].

5.7 Background Subtraction

In order to obtain the right number of exclusive events for the process $\gamma^* n\,(p) \rightarrow p\pi^-\,(p)$ from deuterium target data, we need to remove all possible backgrounds within the M_s^2 cut region. For this reason, the events of the $\gamma^* p \rightarrow p\pi^-\pi^+$ process, considered to be the main source of possible physics background, are simulated by the double-pion scattering event generator ("genev" [11]) under the same experimental condition as the "e1e" run. Then, we applied the same data analysis procedure to these simulated events, and compared their M_s^2 (calculated from Eq. (3.26)) distributions with that of the "e1e" run experimental data and the $\gamma^* n(p) \rightarrow p\pi^-(p)$ simulation events to check the background contributions. The compared results are

shown in Fig. 5.7. Inside the 0.811 GeV^2 $< M_s^2 <$ 0.955 GeV^2 cut region, there is no $\gamma^* p \to p\pi^-\pi^+$ background contribution below 1.1 GeV^2. Furthermore, in order to check the arbitrary background contribution, we compare the M_s^2 distributions for experimental events with simulated $\gamma^* n\,(p) \to p\pi^-\,(p)$ events bin by bin. Typical example plots are shown in Fig. 5.8. The M_s^2 distributions of simulated events (red points) are normalized to the data distribution by the integral of their M_s^2 cut areas. In summary, from these above comparisons, there is no need to do any background subtraction for the exclusive $\gamma^* n\,(p) \to p\pi^-\,(p)$ process in the "e1e" run.

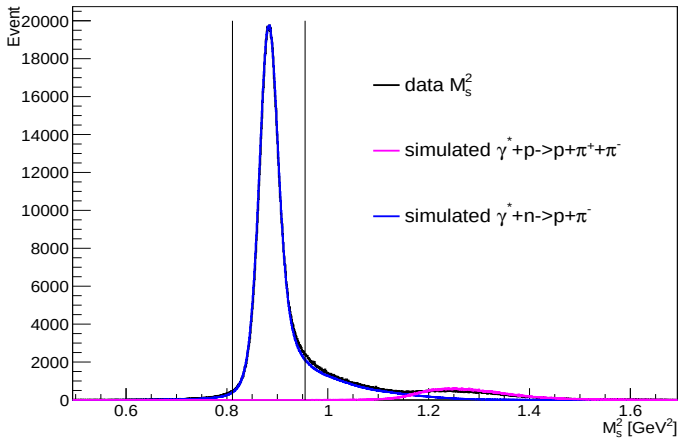

Figure 5.7: M_s^2 distributions for measured (black) and simulated $\gamma^* n\,(p) \to p\pi^-(p)$ (blue), as well as simulated $\gamma^* p \to p\pi^-\pi^+$ events are plotted with the M_s^2 cut limits.

5.8 Inclusive Cross Section

In order to cross check the determined luminosity in the deuteron-target measurement, we extract and compare the cross section of the inclusive scattering $eD \to e^{'}X$ process to Osipenko's world-data parameterization results [54]. In addition to this, we need to check if the problem of the Cherenkov counter not working properly during the hydrogen target period [30] is presented also in the deuteron target data.

For inclusive scattering, since the cross section only depends on two kinematical variables, it is convenient to choose W and Q^2 as binning variables. Then, the

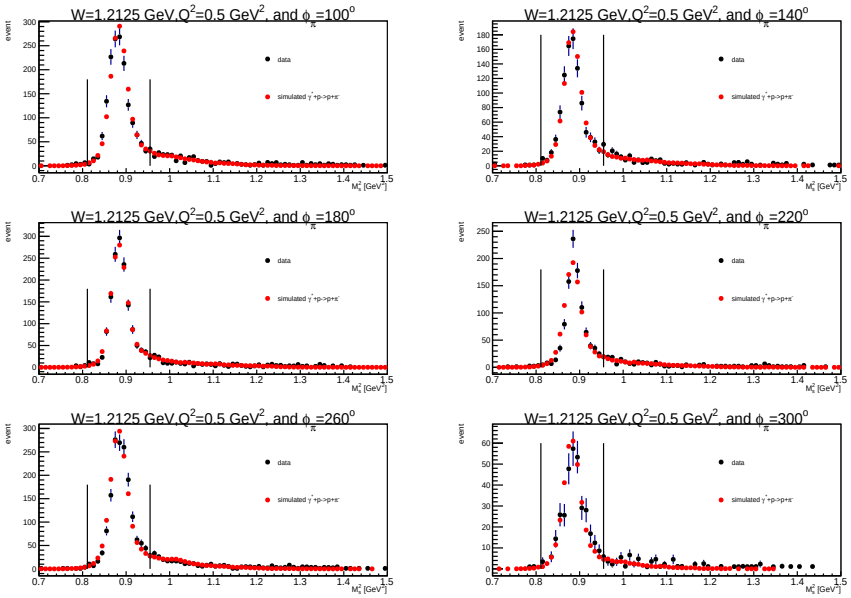

Figure 5.8: M_s^2 distributions for measured (black) and simulated $\gamma^* n\,(p) \to p\pi^-(p)$ (red) events are plotted with the M_s^2 cut limits for $W = 1.2125$ GeV, $Q^2 = 0.5$ GeV, and $\cos\theta^* = -0.3$ in $\phi^*_{\pi^-} = 100°$, 140°, 180°, 220°, 260°, and 300° bins individually.

inclusive cross section is calculated by

$$\frac{d\sigma^2(W,Q^2)}{dW\,dQ^2} = \frac{N_{full}(W,Q^2) - S_{ratio}N_{empty}(W,Q^2)}{\mathcal{L}_{int}\Delta W\Delta Q^2\varepsilon_{eff}(W,Q^2)}, \tag{5.8}$$

where $N_{full}(W,Q^2)$ and $N_{empty}(W,Q^2)$ correspond to the full-and the empty-target event yields in each (W,Q^2) bin. These are inclusive scattering events which passed the whole electron identification procedure described in Chapter 3. Furthermore, S_{ratio} and $\mathcal{L}_{int}$ are calculated by Eq. (5.4) and Eq. (5.3), respectively. ΔW and ΔQ^2 represent the corresponding bin widths. In addition, $\varepsilon_{eff}(W,Q^2)$ is the acceptance correction for each (W,Q^2) bin calculated as

$$\varepsilon_{eff}(W,Q^2) = \frac{N_{rec}(W,Q^2)}{N_{thrown}(W,Q^2)}, \tag{5.9}$$

where N_{rec} denotes to the number of events that passed through the entire simulation process as shown in Fig. 4.1, including the electron identification procedure, N_{thrown} represents those events that are generated by Osipenko's inclusive deuteron scattering event generator [12]. The generator is based on the world data cross section and

includes radiative effects. In order to save simulation time, the thrown events are only generated in a looser fiducial-cut region compared to the data instead of in the complete 4π phase space. In general, the inclusive cross section is calculated from the world data by

$$\frac{d\sigma^2(W,Q^2)}{dWdQ^2} = \frac{N_{thrown}(W,Q^2)}{N_{total}\Delta W\Delta Q^2}\sigma_{int}, \tag{5.10}$$

where N_{total} is the total number of events generated in 4π phase space, $N_{thrown}(W,Q^2)$ corresponds to the yield in each (W,Q^2) bin, and σ_{int} is the integral cross section of the world data. In this way, we compare the inclusive $eD \to e^{'}X$ cross section calculated by Eq. (5.8) from the experimental data with that calculated by Eq. (5.10) from the world data parameterization. However, in this particular case, instead of comparing Eq. (5.8) with Eq. (5.10) results, one can compare $\varepsilon_{eff}(W,Q^2) \times$ Eq. (5.8) with the $\varepsilon_{eff}(W,Q^2) \times$ Eq. (5.10) results. For this particular event generator, $\varepsilon_{eff}(W,Q^2)$ can also be written as

$$\varepsilon_{eff}(W,Q^2) = \frac{N_{rec}(W,Q^2)}{N_{thrown}(W,Q^2)} = \frac{N_{rec}(W,Q^2)\varepsilon^{osi}_{fid}(W,Q^2)}{N^{osi}_{thrown}(W,Q^2)}, \tag{5.11}$$

where $N^{osi}_{thrown}(W,Q^2)$ corresponds to the yield in each (W,Q^2) bin with θ and ϕ angles covered in Dr.Osipenko's fiducial-cut region [12] and $\varepsilon^{osi}_{fid}(W,Q^2)$ is defined as $\frac{N^{osi}_{thrown}(W,Q^2)}{N_{thrown}(W,Q^2)}$.

Multiplying Eq. (5.8) by $\varepsilon_{eff}(W,Q^2)$, the corresponding result is given by

$$\varepsilon_{eff}(W,Q^2) \times Eq.\ (5.8) = \frac{N_{full}(W,Q^2) - \frac{Q_{full}}{Q_{empty}}N_{empty}(W,Q^2)}{\mathcal{L}_{int}\Delta W\Delta Q^2}. \tag{5.12}$$

Furthermore, we multiply Eq. (5.10) by $\varepsilon_{eff}(W,Q^2)$, which is calculated by Eq. (5.11) and leads to the whole expression

$$\begin{aligned}
\varepsilon_{eff}(W,Q^2) \times Eq.\ (5.10) &= \frac{N_{rec}(W,Q^2)\varepsilon^{osi}_{fid}(W,Q^2)}{N^{osi}_{thrown}(W,Q^2)} \times \frac{N_{thrown}(W,Q^2)}{N_{total}\Delta W\Delta Q^2}\sigma_{int} \\
&= \frac{N_{rec}(W,Q^2)\varepsilon^{osi}_{fid}(W,Q^2)}{N^{osi}_{thrown}(W,Q^2)} \times \frac{N^{osi}_{thrown}(W,Q^2)\varepsilon^{osi}_{fid}\sigma_{int}}{\varepsilon^{osi}_{fid}(W,Q^2)N^{osi}_{total}\Delta W\Delta Q^2} \\
&= \frac{N_{rec}(W,Q^2)}{N^{osi}_{total}\Delta W\Delta Q^2}\sigma^{osi}_{int},
\end{aligned} \tag{5.13}$$

where ε_{fid}^{osi} is the acceptance factor of Osipenko's event generator and σ_{int}^{osi} is the reduced integral cross section corresponding to the Osipenko's fiducial-cut region. So finally, we compare Eq. (5.12) and Eq. (5.13) directly, and the corresponding comparison plots are shown in Fig. 5.9. Where the data normalized yields (black stars) extracted from Eq. (5.12) project on W variable in each individual Q^2 bin are consistent with the model dependent Osipenko's world-data parameterization results calculated from Eq. (5.13) (magenta stars), which shows that overall luminosity and hence the corresponding normalization procedure is reliable within the estimated systematic error of 5% (see Chapter 6)and can therefore be applied to the exclusive scattering $\gamma^* n\,(p) \rightarrow p\pi^-(p)$ process.

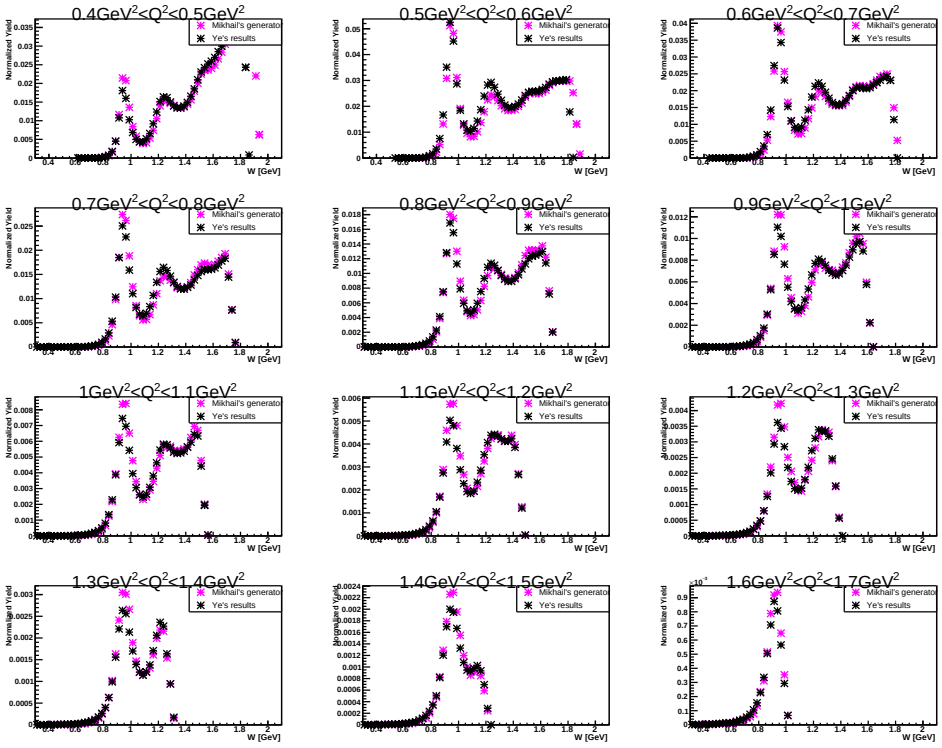

Figure 5.9: W dependent normalized yield distributions in the $eD \rightarrow e^{'}X$ process are presented for data with black stars and for Osipenko's world-data parameterization with magenta stars in individual Q^2 bins from 0.4 GeV^2 to 1.7 GeV^2 in steps of $\Delta Q^2 = 0.1$ GeV^2.

Chapter 6

Results

In a short summary, the whole data analysis process is shown as a flowchart in Fig. 6.1. With all the information discussed in the previous chapters, the final cross sections will be calculated in this chapter, from which the electromagnetic multipoles can be extracted and finally passed through amplitudes analyses to calculate the $N - N^*$ transition form factors, which are beyond the scope of this thesis.

6.1 Cross Sections

The Exclusive Cross Section

The exclusive cross section of the $\gamma^* n\,(p) \rightarrow p\pi^-\,(p)$ process can be calculated from the acceptance corrected yield of the exclusive events as

$$\begin{aligned}\frac{d\sigma^{ex}}{d\Omega^*_{\pi^-}} &= \frac{1}{\Gamma_\upsilon\,(W,Q^2)}\frac{d^4\sigma}{dW\,dQ^2 d\Omega_{\pi^*_-}} \\ &= \frac{(\Delta N_{full}\,(W,Q^2,\cos\theta^*_{\pi^-},\phi^*_{\pi^-}) - S_{ratio}\Delta N_{empty}\,(W,Q^2,\cos\theta^*_{\pi^-},\phi^*_{\pi^-}))R_{BC}}{\Gamma_\upsilon\,(W,Q^2)\,A_{RC}(W,Q^2,\cos\theta^*_{\pi^-},\phi^*_{\pi^-})\Delta W\,\Delta Q^2\,\Delta\cos\theta^*_{\pi^-}\,\Delta\phi^*_{\pi^-}\,\mathcal{L}_{int}},\end{aligned} \tag{6.1}$$

where ΔN_{full} and ΔN_{empty} represent the numbers of the exclusive events inside each 4-dimensional bin $(W, Q^2, \cos\theta^*_{\pi^-}, \phi^*_{\pi^-})$ for the target with and without LD_2, respectively. $A_{RC}(W, Q^2, \cos\theta^*_{\pi^-}, \phi^*_{\pi^-})$ is the radiative corrected acceptance-correction factor calculated from Eq. (5.7), and S_{ratio} is the integrated Faraday Cup ratio, which is calculated from Eq. (5.4). In addition, R_{BC} is the bin-centering correction factor, which is calculated from Eq. (5.1). $\Gamma_\upsilon\,(W, Q^2)$ represents the virtual photon flux that

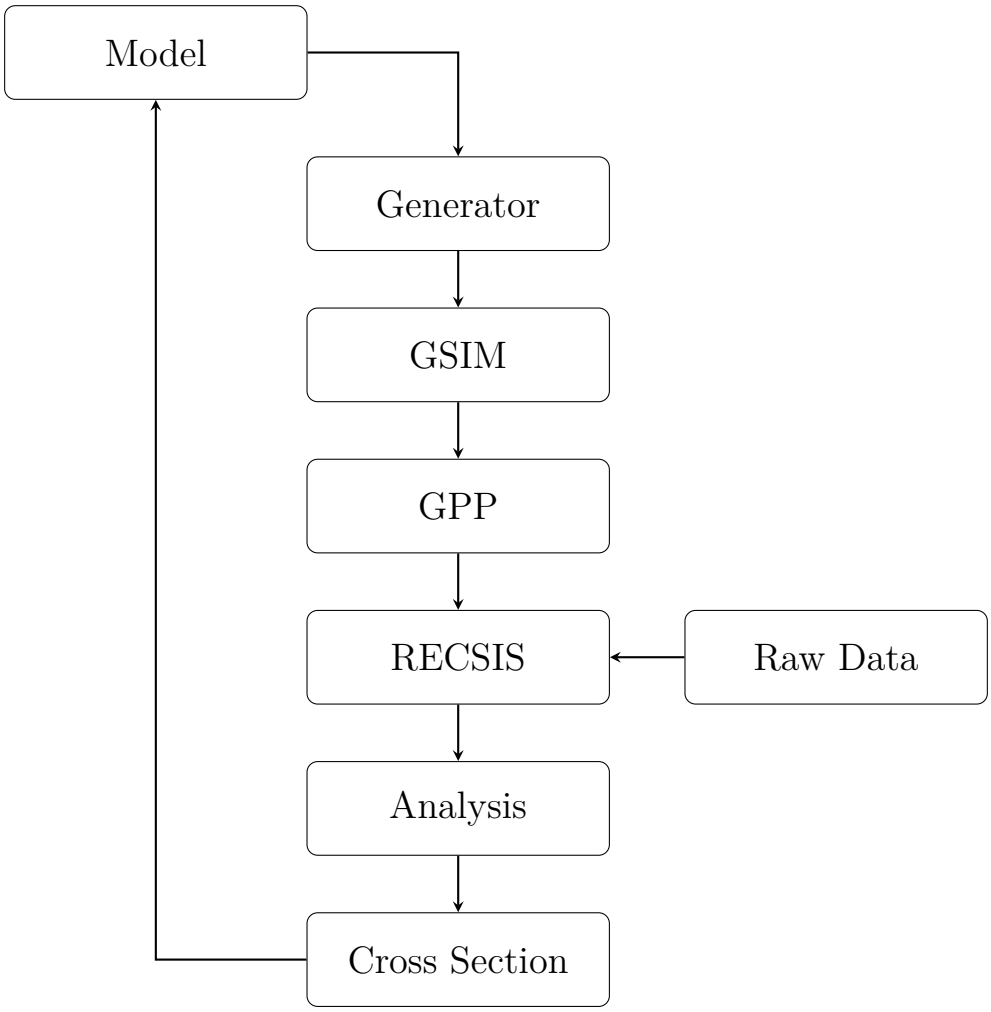

Figure 6.1: The whole analysis process. Simulated physics events are generated according to the reaction model MAID2000 and processed through the GSIM and GPP detector simulation programs. The output of the detector simulation programs looks like the raw data and is processed by the program RECSIS, which is also used for the raw experimental data. Then the reconstructed simulated and experimental events are analyzed through the analysis code to extract the cross section. In the future, the extracted cross sections can be used as an input to the reaction model to apply on the event generator to further improve the simulation results.

is obtained from Eq. (1.30). ΔW, ΔQ^2, $\Delta \cos\theta^*_{\pi^-}$ and $\Delta\phi^*_{\pi^-}$ are the bin widths of the corresponding kinematic variables. $\mathcal{L}_{int}$ is the luminosity calculated by Eq. (5.3).

The Exclusive Quasi-free Cross Section

As described in Chapter 3, we extract the exclusive quasi-free events successfully by applying a $|\vec{P}_s|<$ 200 MeV cut on the exclusive events. The exclusive quasi-free cross section is then calculated by

$$\frac{d\sigma^{qf}}{d\Omega^*_{\pi^-}} = \frac{d\sigma^{cut}}{d\Omega^*_{\pi^-}} \frac{1}{r\left(W, Q^2, \cos\theta^*, \phi^*\right)}, \tag{6.2}$$

where $\frac{d\sigma^{cut}}{d\Omega^*_{\pi^-}}$ is the cross section calculated after applying the $|\vec{P}_s|<$ 200 MeV cut and $r\left(W, Q^2, \cos\theta^*, \phi^*\right)$ obtained from Eq. (3.27) denotes the factor to correct good quasi-free events outside the $|\vec{P}_s|<$ 200 MeV cut. Based on the yield of the cut-surviving events, the cross section is extracted as

$$\frac{d\sigma^{cut}}{d\Omega^*_{\pi^-}} = \frac{\left(\Delta N^{cut}_{full}\left(W, Q^2, \cos\theta^*, \phi^*\right) - S_{ratio}\Delta N^{cut}_{empty}\left(W, Q^2, \cos\theta^*, \phi^*\right)\right) R_{BC}}{\Gamma_v\left(W, Q^2\right) A^{cut}_{RC}(W, Q^2, \cos\theta^*, \phi^*)\Delta W \Delta Q^2 \Delta\cos\theta^* \Delta\phi^* \mathcal{L}_{int}}, \tag{6.3}$$

where "cut" presents the corresponding quantities that are calculated within the $|\vec{P}_s|<$ 200 MeV cut condition.

From the above information, the full exclusive and quasi-free cross sections are calculated in dependence on the angle $\phi^*_{\pi^-}$. In this way, the physics information is extracted conveniently by the angular dependencies of the cross sections. In the Δ resonance region, the example $\phi^*_{\pi^-}$ dependent cross sections with high statistics at $W = 1.2125$ GeV for different Q^2 bins are shown in Figs. 6.2, 6.3, and 6.4. In these figures, the full exclusive and quasi-free cross sections are represented by the black points and green squares, respectively, as well as the corresponding systematic uncertainties (see Chapter 6.5) by the black bars in the bottom of each plot. These cross-section points are distributed symmetrically around $\phi^*_{\pi^-} = 180°$; this demonstrates the good quality of the measured cross sections. In addition, these $\phi^*_{\pi^-}$

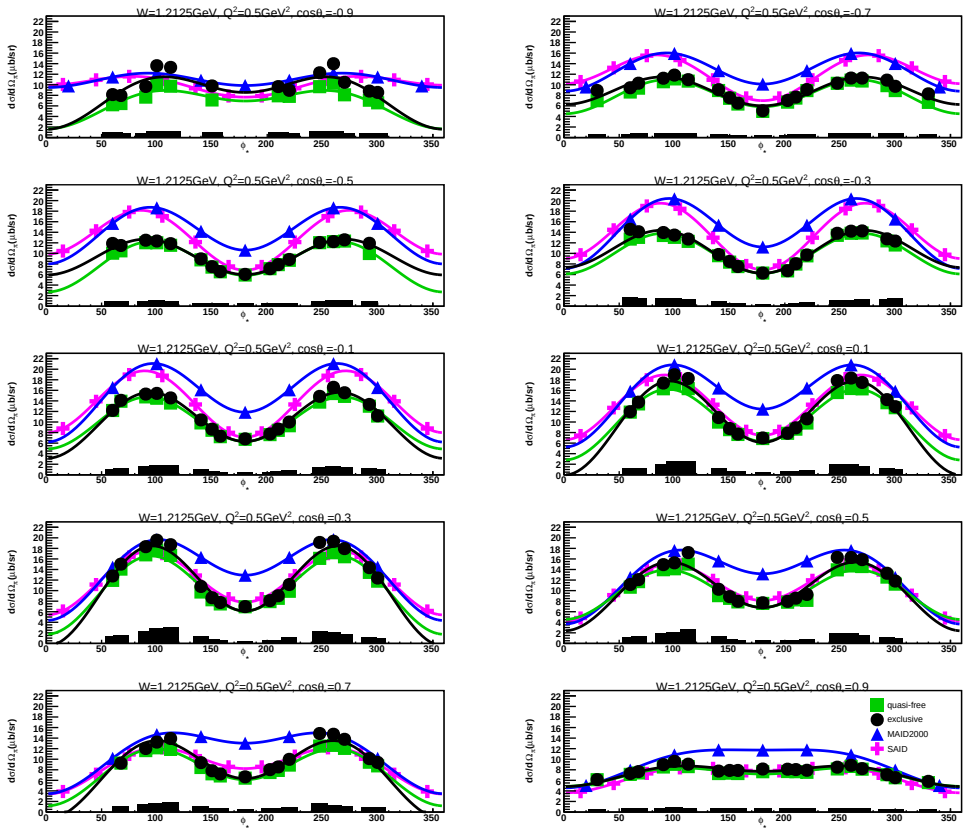

Figure 6.2: Exclusive (black points) and quasi-free (green squares) cross sections in μb/sr are represented for $W = 1.2125$ GeV and $Q^2 = 0.5$ GeV^2. The $\phi^*_{\pi^-}$ dependent cross sections are illustrated in each $\cos\theta^*_{\pi^-}$ bin. The magenta crosses and blue triangles show SAID and MAID2000 model predictions. The color lines show fits to the cross sections by the function "$a + b\cos 2\phi^*_{\pi^-} + c\cos\phi^*_{\pi^-}$". The black bars at the bottom of each subplot represent the systematic uncertainty for each cross section points.

dependent cross sections are fit by the function "$a + b\cos 2\phi^*_{\pi^-} + c\cos\phi^*_{\pi^-}$", which is presented by the corresponding color line, to extract the physics quantities for the amplitude analysis. In Figs. 6.2, 6.3, and 6.4, these cross sections are presented at the same $W = 1.2125$ GeV bin but with gradually increasing Q^2. The comparison shows that these cross sections decrease with increasing Q^2. Furthermore, in each $(W, Q^2, \cos\theta^*_{\pi^-})$ bin, there is not enough data to provide statistically trustworthy cross sections at the very forward and backward $\phi^*_{\pi^-}$ angles.

In the second and the third resonance regions, examples of these cross sections

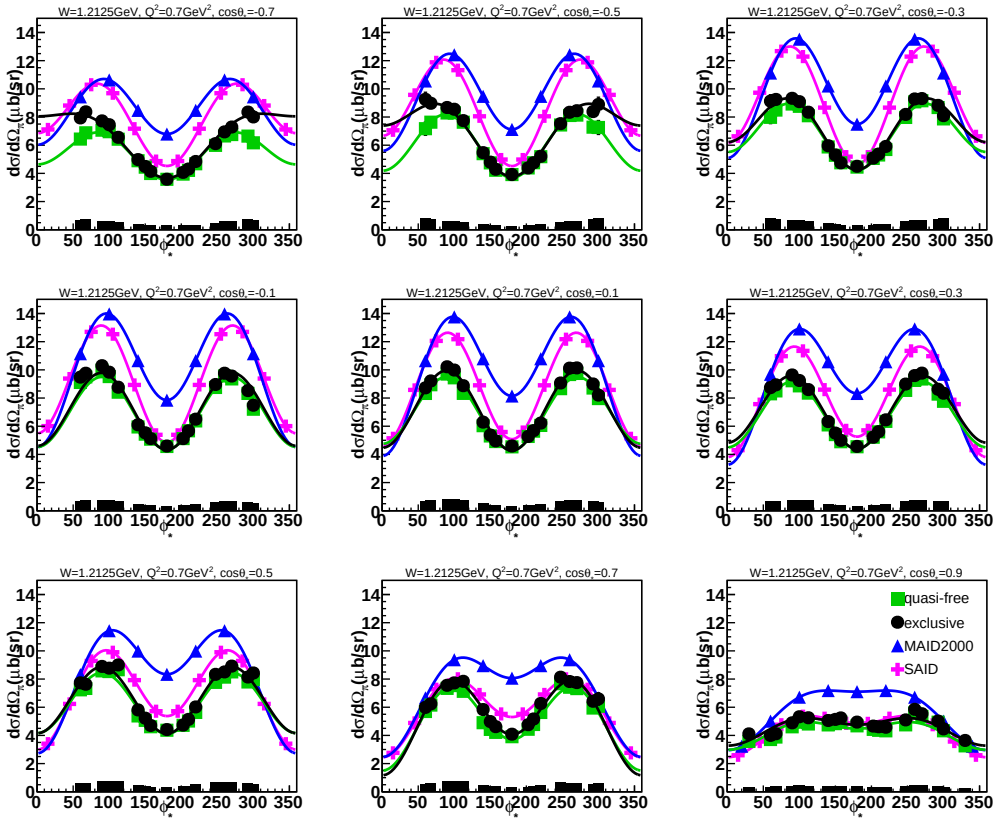

Figure 6.3: Exclusive (black points) and quasi-free (green squares) cross sections in μb/sr are represented for $W = 1.2125$ GeV and $Q^2 = 0.7$ GeV^2. The $\phi^*_{\pi^-}$ dependent cross sections are illustrated in each $\cos\theta^*_{\pi^-}$ bin. The magenta crosses and blue triangles show SAID and MAID2000 model predictions. The color lines show fits to the cross sections by the function "$a + b\cos 2\phi^*_{\pi^-} + c\cos\phi^*_{\pi^-}$". The black bars at the bottom of each subplot represent the systematic uncertainty for each cross section points.

are shown at $W = 1.4875$ GeV and $W = 1.6625$ GeV for the same $Q^2 = 0.5$ GeV^2 bin in Figs. 6.5 and 6.6, respectively. In the higher resonance region, we have even less statistics, leading to $\phi^*_{\pi^-}$ dependent cross sections with typically less data points at all $\theta^*_{\pi^-}$ angles. As it can be seen in Figs. 6.2, 6.3, 6.4, 6.5, and 6.6, in each $(W, Q^2, \cos\theta^*_{\pi^-})$ bin, the exclusive cross section is always larger than the quasi-free cross section due to additional contributions from final state interactions.

Furthermore, the measured cross sections are compared with the predictions of two models, SAID [4] and MAID2000 [8], which describe successfully the cross sec-

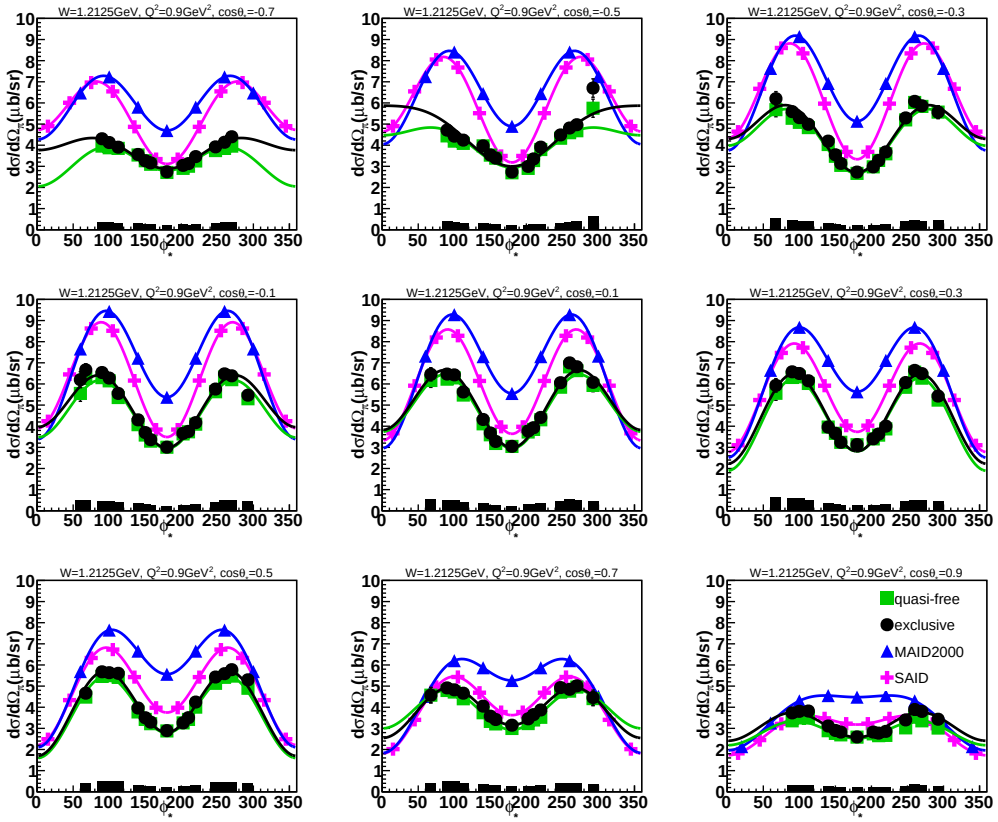

Figure 6.4: Exclusive (black points) and quasi-free (green squares) cross sections in μb/sr are represented for $W = 1.2125$ GeV and $Q^2 = 0.9$ GeV^2. The $\phi^*_{\pi^-}$ dependent cross sections are illustrated in each $\cos\theta^*_{\pi^-}$ bin. The magenta crosses and blue triangles show SAID and MAID2000 model predictions. The color lines show fits to the cross sections by the function "$a + b\cos 2\phi^*_{\pi^-} + c\cos\phi^*_{\pi^-}$". The black bars at the bottom of each subplot represent the systematic uncertainty for each cross section points.

tions of the single pion production off the free proton in the low-lying resonance region. Examples of this comparison are shown in Figs. 6.2, 6.3, 6.4, 6.5, and 6.6. The magenta crosses and blue triangles represent the model predictions of SAID and MAID2000 individually. In the Δ resonance region, these cross sections are in reasonable agreement with the predictions of the SAID model at forward $\theta^*_{\pi^-}$ angles. However, at the backward $\theta^*_{\pi^-}$ angles, the measured cross sections are smaller than the prediction of both models. Due to the lack of experimental data for the $\gamma^* n\,(p) \to p\pi^-\,(p)$ process, the discrepancy between the model predictions and the

measured cross-section results is not surprising. The models need neutron data to improve their predictions.

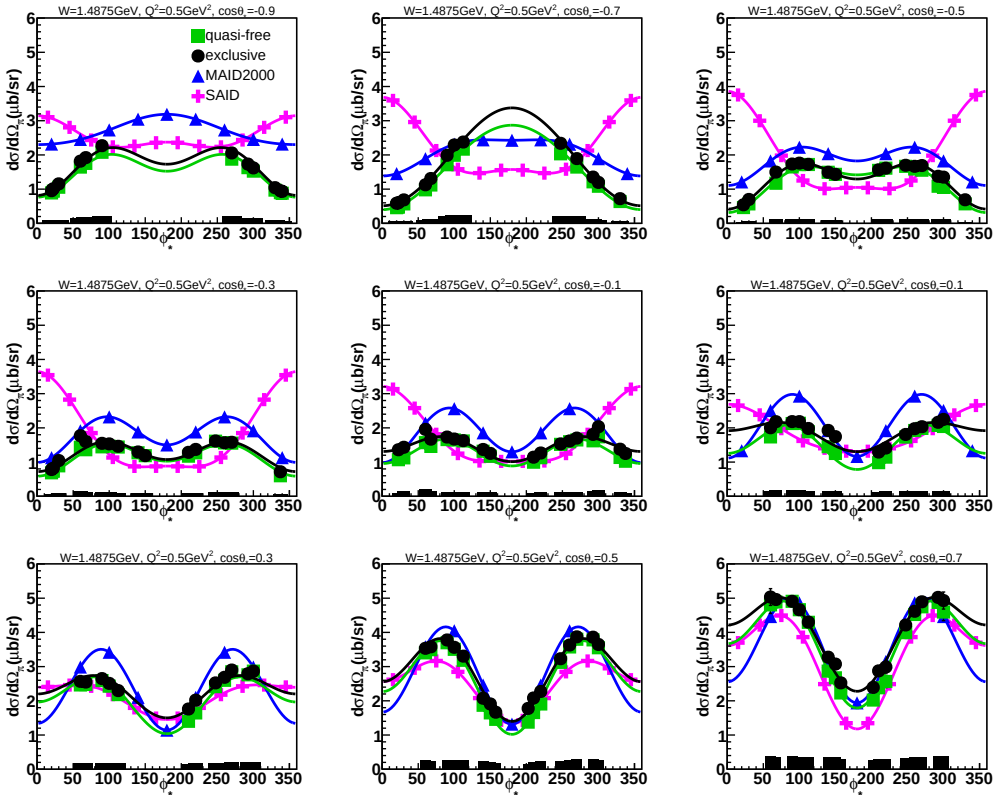

Figure 6.5: Exclusive (black points) and quasi-free (green squares) cross sections in μb/sr are represented for $W = 1.4875$ GeV and $Q^2 = 0.5$ GeV^2. The $\phi^*_{\pi^-}$ dependent cross sections are illustrated in each $\cos\theta^*_{\pi^-}$ bin. The magenta crosses and blue triangles show SAID and MAID2000 model predictions. The color lines show fits to the cross sections by the function "$a + b\cos 2\phi^*_{\pi^-} + c\cos\phi^*_{\pi^-}$". The black bars at the bottom of each subplot represent the systematic uncertainty for each cross section points.

6.2 Kinematical Final State Interaction Contribution

With the measured fully exclusive and quasi-free differential cross sections, the kinematical final-state-interaction contribution factor R_{FSI} can be calculated for each 4 dimensional bin $(W, Q^2, \cos\theta^*_{\pi^-}, \phi^*_{\pi^-})$. This factor accounts for the fraction of final state interactions in the full exclusive process and is defined by

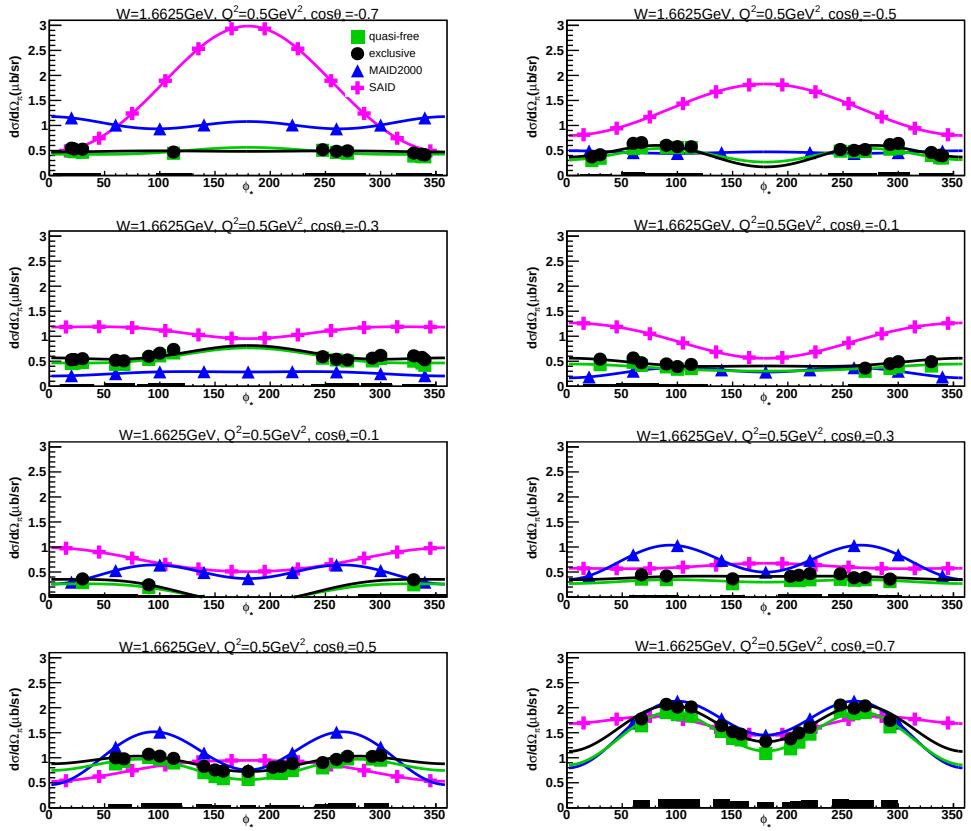

Figure 6.6: Exclusive (black points) and quasi-free (green squares) cross sections in μb/sr are represented for $W = 1.6625$ GeV and $Q^2 = 0.5$ GeV^2. The $\phi^*_{\pi^-}$ dependent cross sections are illustrated in each $\cos\theta^*_{\pi^-}$ bin. The magenta crosses and blue triangles show SAID and MAID2000 model predictions. The color lines show fits to the cross sections by the function "$a + b\cos 2\phi^*_{\pi^-} + c\cos\phi^*_{\pi^-}$". The black bars at the bottom of each subplot represent the systematic uncertainty for each cross section points.

$$R_{FSI}(W, Q^2, cos\theta^*_{\pi^-}, \phi^*_{\pi^-}) = \frac{\frac{d\sigma^{qf}}{d\Omega^*_{\pi^-}}}{\frac{d\sigma^{ex}}{d\Omega^*_{\pi^-}}}. \tag{6.4}$$

From the physics perspective, kinematical final state interaction contribution factor R_{FSI} should be $\phi^*_{\pi^-}$ independent. The ratio between $R_{FSI}(W, Q^2, \cos\theta^*_{\pi^-}, \phi^*_{\pi^-})$ and $R_{FSI}(W, Q^2, \cos\theta^*_{\pi^-})$ (i.e. $\phi^*_{\pi^-}$ integrated $R_{FSI}(W, Q^2, \cos\theta^*_{\pi^-}, \phi^*_{\pi^-})$) are plotted against $\phi^*_{\pi^-}$. Distribution examples for 1.2 GeV $< W <$ 1.225 GeV and 0.6 GeV^2 $< Q^2 <$ 0.8 GeV^2 are shown in Figs. 6.7 and 6.8 for W binning according to W_i and W_f, respectively. Each individual plot represents the ratios for different $\cos\theta^*_{\pi^-}$ bins. It

turns out that the ratios all distribute around one without a $\phi^*_{\pi^-}$ dependent structure if binned in W_i rather than W_f. For the quasi-free events, binning data in W_f is the best choice from what we have observed. However for the exclusive events, which include final state interactions, it seams that binning the data with W_i is the better choice. We will need further investigate and optimize the impact of the W binning on the data extraction.

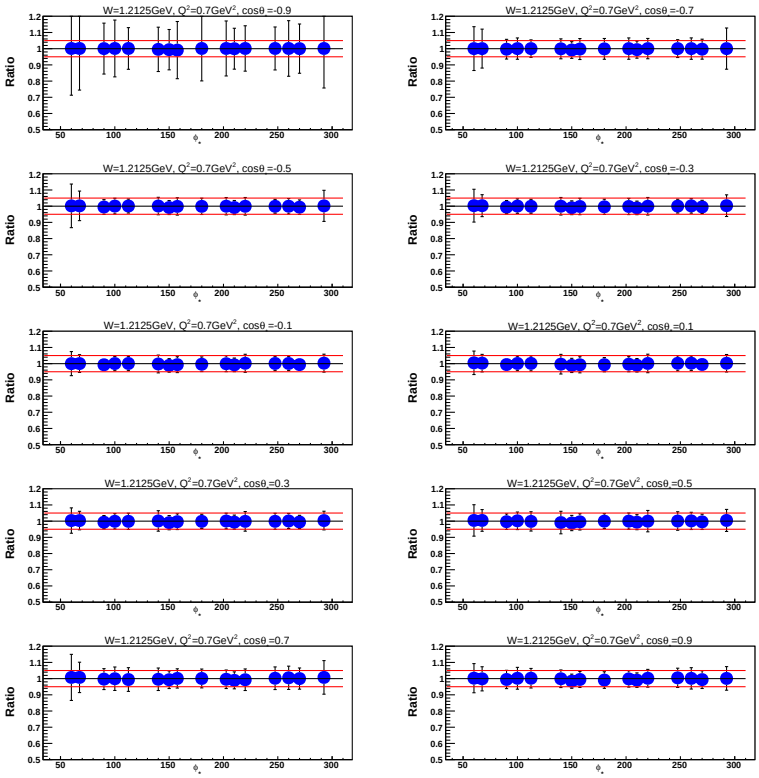

Figure 6.7: The ratios of $R_{FSI}(W_i, Q^2, \cos\theta^*_{\pi^-}, \phi^*_{\pi^-})$ over $R_{FSI}(W_i, Q^2, \cos\theta^*_{\pi^-})$ are represented by Blue points for different $\phi^*_{\pi^-}$ at 1.2 GeV $< W_i <$ 1.225 GeV and 0.6 GeV^2 $< Q^2 <$ 0.8 GeV^2. The individual plot shows the ratios for different $\cos\theta^*_{\pi^-}$ bins. The three lines from bottom to top correspond to 0.95, 1, and 1.05, respectively.

In order to quantify the dependence of kinematical final-state-interaction contribution factors R_{FSI} on the polar angle $\theta^*_{\pi^-}$, the $\phi^*_{\pi^-}$ integrated R_{FSI} versus $\theta^*_{\pi^-}$ distributions are plotted for different W and Q^2 bins, which are shown in the Figs. 6.9, 6.10, and 6.11, respectively. The red and black points correspond to R_{FSI} binned in W_i and W_f, respectively. The dependence of kinematical final-state-interaction con-

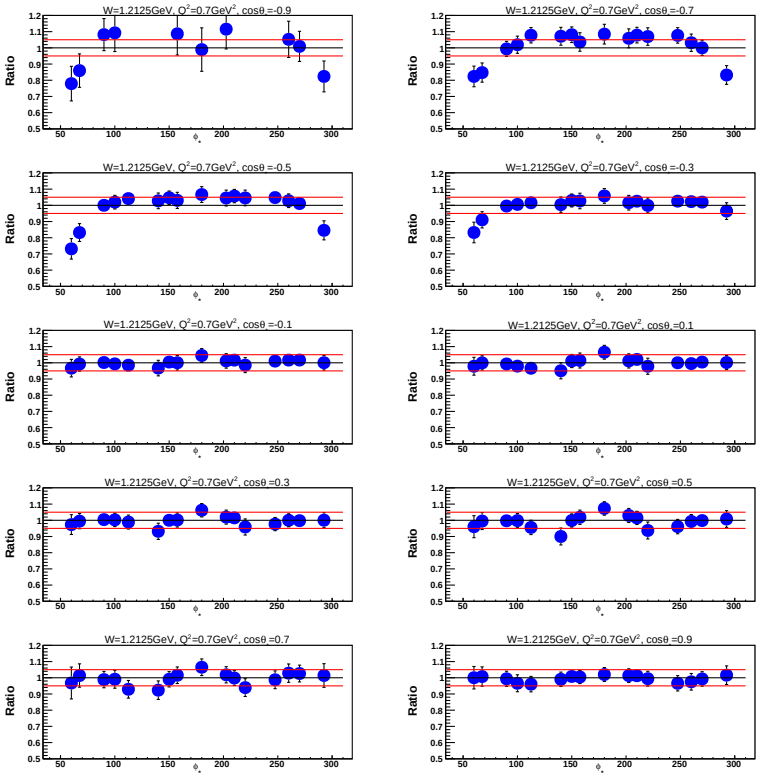

Figure 6.8: The ratios of $R_{FSI}(W_i, Q^2, \cos\theta^*_{\pi^-}, \phi^*_{\pi^-})$ over $R_{FSI}(W_i, Q^2, \cos\theta^*_{\pi^-})$ are represented by Blue points for different $\phi^*_{\pi^-}$ at 1.2 GeV $< W <$ 1.225 GeV and 0.6 GeV^2 $< Q^2 <$ 0.8 GeV^2. The individual plot shows the ratios for different $\cos\theta^*_{\pi^-}$ bins. The three lines from bottom to top correspond to 0.95, 1, and 1.05, respectively.

tribution factor R_{FSI} on the polar angle $\theta^*_{\pi^-}$ is consistent for both binnings, maybe with the exception of the threshold $W = 1.1125\ GeV$ bin. This is consistent with the fact that the $W_f = \sqrt{(p^\mu + \pi^\mu)^2}$ for the exclusive events is less than the true W value, which should include the undetected outgoing low momentum proton (below the detector threshold). From Figs. 6.9, 6.10, and 6.11, it turns out that the final state interaction contribution for the reaction $\gamma^* n(p) \to p\pi^-(p)$ with the "e1e" run data kinematic coverage is on average about $10\% - 20\%$.

6.3 Structure Functions

The above hadronic cross sections are fit in terms of $\cos\phi^*_{\pi^-}$ and $\cos 2\phi^*_{\pi^-}$ (Eq. (6.5)) to extract the structure functions. Each fitted function has three fit parameters

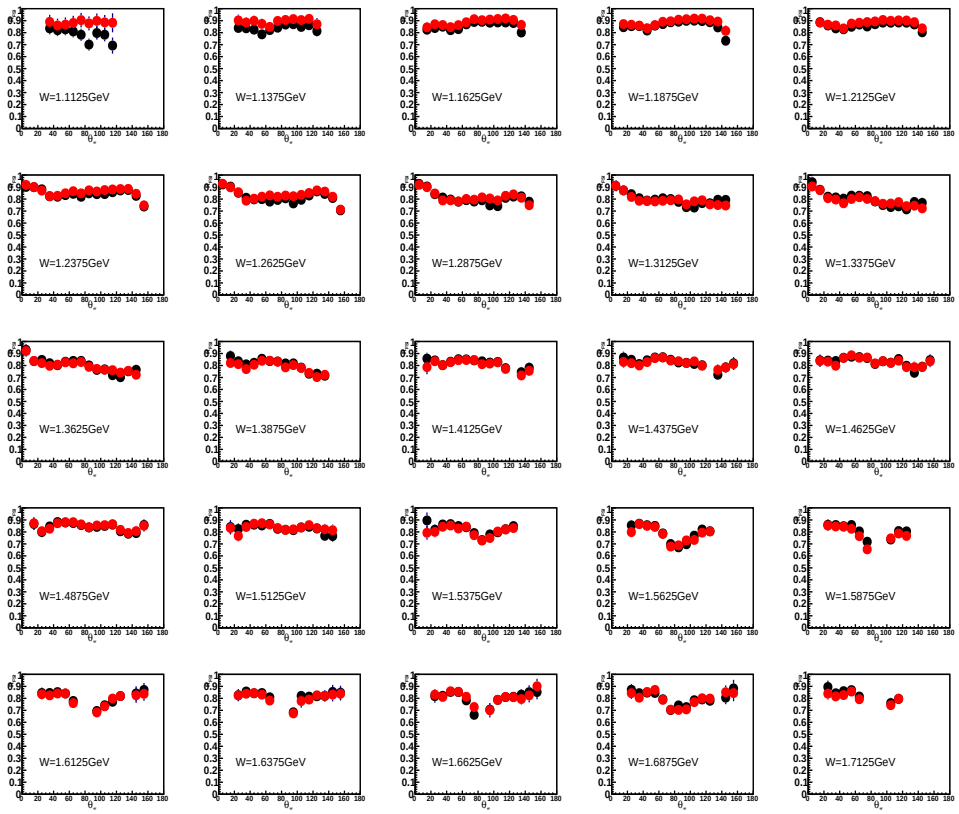

Figure 6.9: R_{FSI} versus $\theta^*_{\pi^-}$ distribution example for individual W bins, which are increasing by 0.025 GeV in the range of 1.1 GeV $< W <$ 1.725 GeV for 0.4 GeV^2 $< Q^2 <$ 0.6 GeV^2. The red and black points correspond to R_{FSI} binned in W_i and W_f, respectively.

a, b, and c, which correspond to the structure functions $\sigma_T + \epsilon\sigma_L$, σ_{TT}, and σ_{TL}, respectively,

$$\frac{d\sigma}{d\Omega^*_{\pi^-}} = a + b\cos 2\phi^*_{\pi^-} + c\cos\phi^*_{\pi^-},\ a = \sigma_T + \epsilon\sigma_L,\ b = \epsilon\sigma_{TT},\ \text{and}\ c = \sqrt{2\epsilon\,(1+\epsilon)}\sigma_{TL}, \tag{6.5}$$

where ϵ is the transverse polarization of the virtual photon, "T" and "L" represent transverse and longitudinal components, as well as "TT" and "TL" the interference terms. The exclusive and quasi-free cross sections from Eq. (6.1) and Eq. (6.2), respectively, are fit to extract the corresponding structure functions. Examples at $W = 1.2125$ GeV with $Q^2 = 0.5$ GeV^2, $Q^2 = 0.7$ GeV^2, and $Q^2 = 0.9$ GeV^2 are shown in Fig. 6.2. In addition, these structure functions are also compared with the

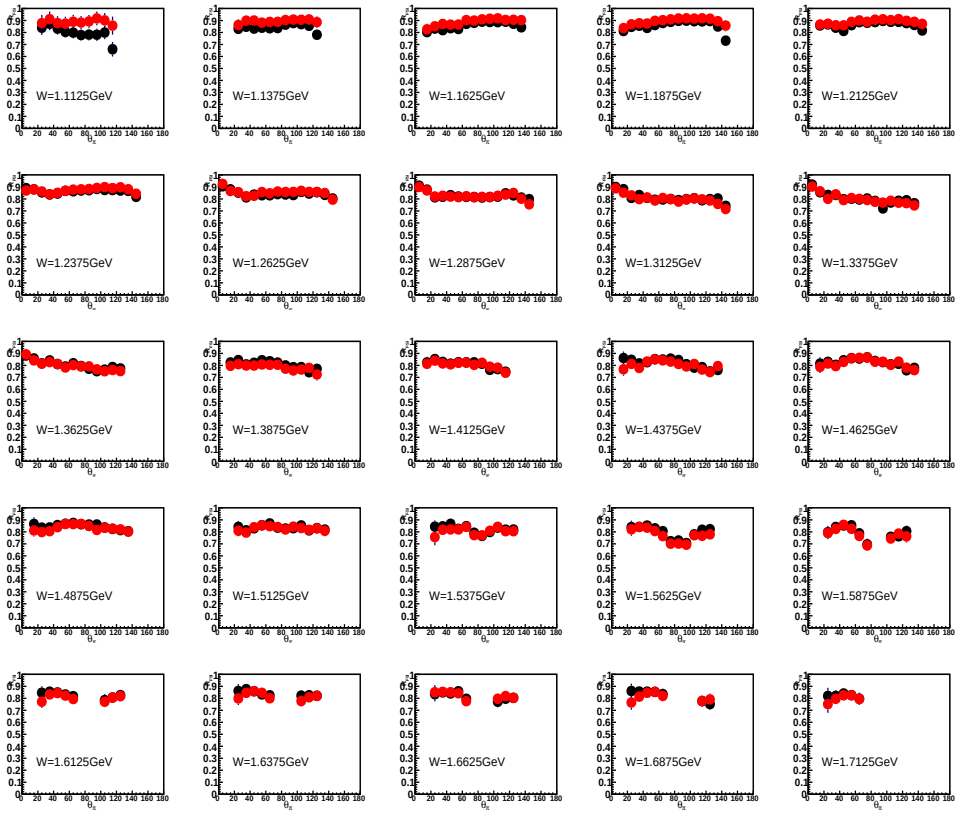

Figure 6.10: R_{FSI} versus $\theta^*_{\pi^-}$ distributions example for individual W bins, which are increasing by 0.025 GeV in the range of 1.1 GeV $< W <$ 1.725 GeV for 0.6 GeV^2 $< Q^2 <$ 0.8 GeV^2. The red and black points correspond to R_{FSI} binned in W_i and W_f, respectively.

predictions of the SAID and MAID2000 models. The solid black bars show the systematic errors that are calculated through error propagation procedure, see Chapter 6.5. The color lines represent the corresponding Legendre polynomial expansions for π^- angular momenta up to $l = 2$. These fits are discussed in the following section.

6.4 Legendre Polynomials Expansion

For each (W, Q^2) bin, the extracted structure functions are functions of $\cos\theta^*_{\pi^-}$ and can be expressed in terms of Legendre polynomials. In this way, we can get insight on the dominant wave contribution in a particular resonance region. The Legendre polynomial expansion of the structure functions for π^- angular momentum up to

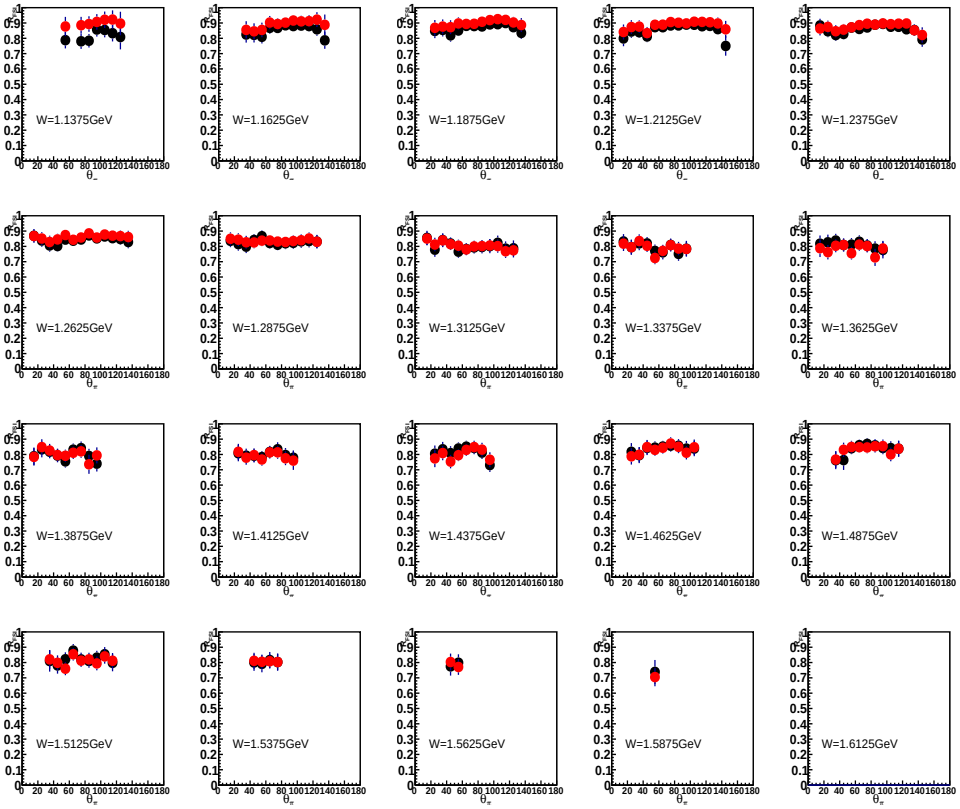

Figure 6.11: R_{FSI} versus $\theta^*_{\pi^-}$ distributions example for individual W bins, which are increasing by 0.025 GeV in the range of 1.125 GeV $< W <$ 1.6 GeV for 0.8 GeV^2 $< Q^2 <$ 1.0 GeV^2. The red and black points correspond to R_{FSI} binned in W_i and W_f, respectively.

$l = 1$ (p-wave) can be expressed by

$$\sigma_T + \epsilon\sigma_L = A_0 P_0(\cos\theta^*_{\pi^-}) + A_1 P_1(\cos\theta^*_{\pi^-}) + A_2 P_2(\cos\theta^*_{\pi^-}), \tag{6.6}$$

$$\sigma_{TT} = B_0 P_0(\cos\theta^*_{\pi^-}), \tag{6.7}$$

$$\sigma_{LT} = C_0 P_0(\cos\theta^*_{\pi^-}) + C_1 P_1(\cos\theta^*_{\pi^-}), \tag{6.8}$$

and up to $l = 2$ (d-wave) by

$$\begin{aligned}\sigma_T + \epsilon\sigma_L =& A_0 P_0(\cos\theta^*_{\pi^-}) + A_1 P_1(\cos\theta^*_{\pi^-}) + A_2 P_2(\cos\theta^*_{\pi^-}) + A_3 P_3(\cos\theta^*_{\pi^-}) \\ &+ A_4 P_4(\cos\theta^*_{\pi^-}),\end{aligned} \tag{6.9}$$

$$\sigma_{TT} = B_0 P_0(\cos\theta^*_{\pi^-}) + B_1 P_1(\cos\theta^*_{\pi^-}) + B_2 P_2(\cos\theta^*_{\pi^-}), \text{ and} \tag{6.10}$$

$$\sigma_{LT} = C_0 P_0(\cos\theta^*_{\pi^-}) + C_1 P_1(\cos\theta^*_{\pi^-}) + C_2 P_2(\cos\theta^*_{\pi^-}) + C_3 P_3(\cos\theta^*_{\pi^-}), \tag{6.11}$$

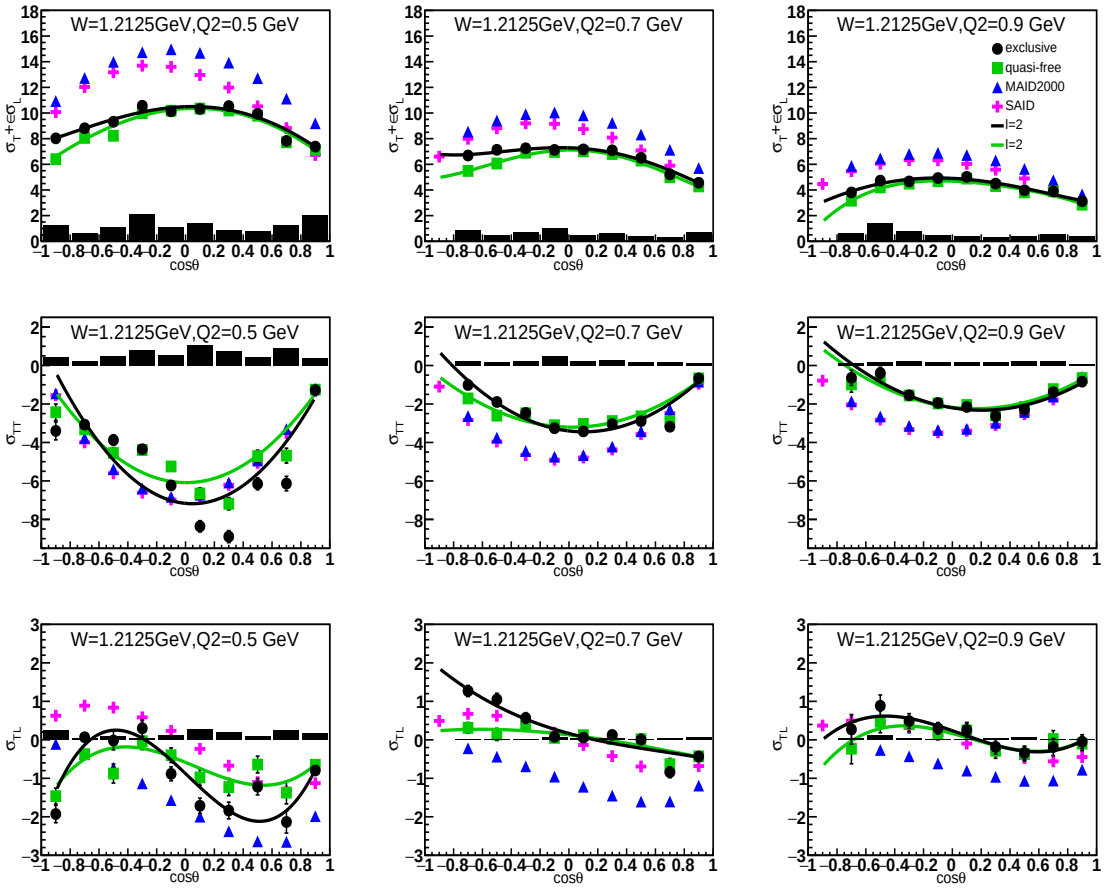

Figure 6.12: Example of the $\cos\theta^*_{\pi^-}$ dependent structure functions $\sigma_T+\epsilon\sigma_L$ (top row), σ_{TT} (middle row), and σ_{TL} (bottom row) for $W = 1.2125$ GeV at $Q^2 = 0.5$ GeV^2 (left column), $Q^2 = 0.7$ GeV^2 (middle column), and $Q^2 = 0.9$ GeV^2 (right column) that are extracted for the exclusive (black points) and quasi-free (green squares) cross sections and compared with the predictions of the SAID (magenta points) and MAID2000 (blue points) models. The solid black bars represent the corresponding systematic uncertainties. The Legendre polynomial expansions are fitted to the corresponding structure function data for π^- angular momenta up to $l = 2$.

where $P_l(\cos\theta^*_{\pi^-})$ corresponds to the lth-order Legendre polynomial, and the coefficients A_l, B_l, and C_l represent the Legendre moments, which can be associated with the magnetic ($M_{l\pm}$), electric ($E_{l\pm}$), and scalar ($S_{l\pm}$) πN multipoles [58]. Figure 6.12 shows that the Legendre polynomial expansion of the structure functions up to $l = 1$ fails to provide an adequate description of the data, but up to $l = 2$ leads already to a reasonable description.

6.5 Systematic Uncertainty

The studied systematic uncertainties for this analysis are these uncertainties that are inherent in the experiment and cannot be improved by repeating the experiment. The systematic uncertainties are calculated for each 4-dimensional variable bin from five different sources.

The first source of systematic uncertainties are the cuts used for particle identification and event selection. It is not feasible to determine the ideal cut positions, so we estimate how the final results depend on the shape and the position of a particular cut.

Since the cross sections are presented in the CM frame, all measured particle momenta from the lab frame have to be boosted to the CM frame through with the boost vector $\vec{\beta}$, which can be calculated either from the initial particle (n^μ and q^μ) or final particles ($\pi^{-\mu}$ and p^μ) four momenta. Even though we finally use $\vec{\beta_f}$, which is calculated from the final state particles, the influence on the final cross sections by using different $\vec{\beta}$s contributes to the systematic uncertainty. Hence, the second source of systematic uncertainty is determined by estimating how much the final results are influenced by the choice of different boost vectors.

In order to isolate the exclusive quasi-free process $\gamma^* n(p_s) \rightarrow p\pi^-(p_s)$, the missing momentum P_s distribution needs to be compared with the simulated Fermi momentum of the spectator. The Fermi momentum distribution of the independent "spectator" proton is generated by the CD-Bonn potential [28] in the event generator. The CD-Bonn potential is considered to be more accurate than other models, such as the Pairs [42] and Hulthen [22] potentials, but for the purpose of the systematic uncertainty study, all three deuteron potential distributions are compared to determine the third source of the systematic uncertainty.

The bin centering correction factor is calculated from the cross-section function of a reaction model, so the influence of applying R_{BC}, as it is calculated from different

models, on the cross sections is the fourth source of the systematic uncertainty.

Last but not least, the normalization uncertainty extracted from the comparison of our measured inclusive cross sections with the world data parameterization results accounts for the last source of the systematic uncertainty.

To study now cut are influencing the results, we typically vary the chosen cuts by making them tighter or looser. So the final results for the systematic uncertainty found due to variation of cuts is determined as the RMS of the deviations of the varied cross section from the original one by

$$\Delta_{cut^i}^{RMS} = \sqrt{\frac{\Delta_{tight}^2 + \Delta_{loose}^2}{2}}, \tag{6.12}$$

where Δ_{tight} and Δ_{loose} correspond to the difference between the cross sections with the chosen cut and the varied one.

The following cuts are studied to determine the final systematic uncertainty.

Electron ID

- θ_{CC} cut

  We vary the θ_{CC} cut within

$$\begin{aligned} &\theta_{CC_\mu} - 3\sigma < \theta_{CC} < \theta_{CC_\mu} + 2\sigma \text{ (tight) and} \\ &\theta_{CC_\mu} - 5\sigma < \theta_{CC} < \theta_{CC_\mu} + 4\sigma \text{ (loose),} \end{aligned} \tag{6.13}$$

  where μ ($\theta_{CC\mu}$) and σ are the original cut parameters, which are introduced in the electron identification section of Chapter 3. The same procedure is applied to the simulation. With the tight or loose cut conditions, the cross sections are calculated exactly in the same way as the above reported final cross section. The systematic uncertainty is determined for each 4-dimensional variable bin, and the average systematic uncertainty over all bins due to the θ_{CC} cut is 0.78%.

- Electron sampling fraction cut

  Similar to the θ_{CC} cut, variations of the sampling fraction cut are represented by

$$\begin{aligned}(\frac{E_{total}}{p_e})_\mu - 2\sigma < \frac{E_{total}}{p_e} < (\frac{E_{total}}{p_e})_\mu + 2\sigma \text{ (tight) and} \\ (\frac{E_{total}}{p_e})_\mu - 4\sigma < \frac{E_{total}}{p_e} < (\frac{E_{total}}{p_e})_\mu + 4\sigma \text{ (loose)},\end{aligned} \tag{6.14}$$

  where μ and σ are the original sampling fraction cut parameters. The average systematical uncertainty over all bins due to this cut is 1.26%.

- Electron fiducial cut

  Electron fiducial tight and loose cut definitions are

$$\begin{aligned}&(sector-1)*60^\circ - \Delta\phi_e + 1^\circ < \phi_e^{sector} < (sector-1)*60^\circ + \Delta\phi_e - 1^\circ \text{(tight)} \ ; \\ &(sector-1)*60^\circ - \Delta\phi_e - 1^\circ < \phi_e^{sector} < (sector-1)*60^\circ + \Delta\phi_e + 1^\circ \text{(loose)} \ ,\end{aligned} \tag{6.15}$$

  where $\Delta\phi_e$ is defined by Eq. (3.16). The electron fiducial cuts contribute 2.10% on average to the final systematic uncertainties.

π^- ID

- π^- ΔT cut

  The pion identification is based on the timing ΔT cut, and the chosen cuts are listed in Eq. (3.10). In order to determine the influence of the ΔT cut variation on the final cross sections, we tighten or loosen the chosen cut as

$$\begin{aligned}(\Delta T_{\pi^-})_\mu - 2\sigma < \Delta T_{\pi^-} < (\Delta T_{\pi^-})_\mu + 2\sigma \text{ (tight) and} \\ (\Delta T_{\pi^-})_\mu - 4\sigma < \Delta T_{\pi^-} < (\Delta T_{\pi^-})_\mu + 4\sigma \text{ (loose)},\end{aligned} \tag{6.16}$$

  where μ and σ are the originally chosen cut parameters. Figure 6.13 shows tight, chosen, and loose cuts together on the π^- ΔT distributions for all sectors. The average systematic uncertainty over all bins due to this cut is 1.78%.

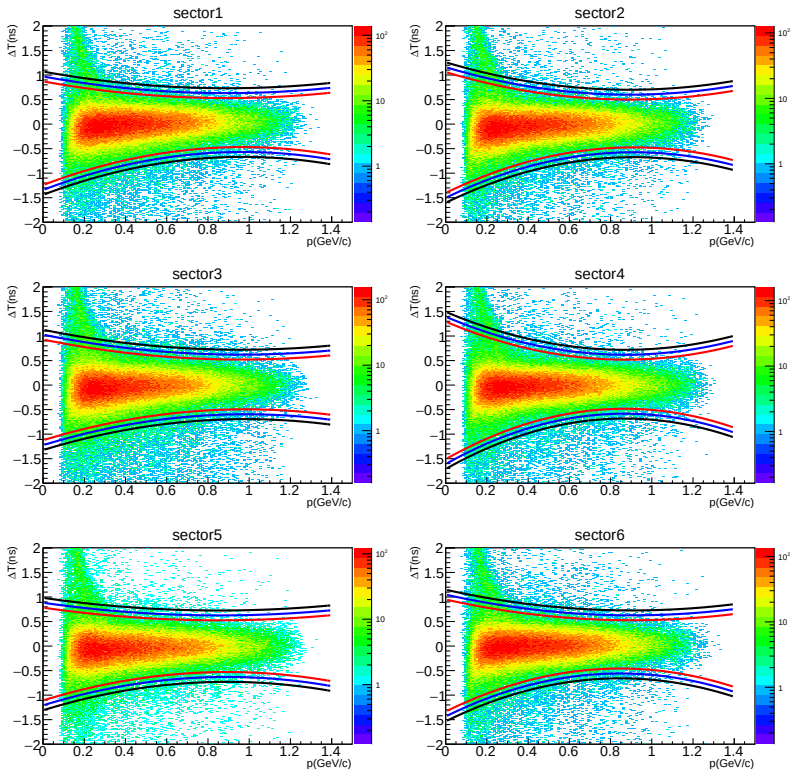

Figure 6.13: The ΔT distribution of pions in six sectors. The black, blue, and red lines represent the 4σ, 3σ, and 2σ cut boundaries, respectively.

- π^- fiducial cut

  We vary the π^- fiducial cut within

$$\begin{aligned} &\phi_{\pi^-}^{min} + 1^\circ < \phi_{\pi^-} < \phi_{\pi^-}^{max} - 1^\circ \text{ (tight) and} \\ &\phi_{\pi^-}^{min} - 1^\circ < \phi_{\pi^-} < \phi_{\pi^-}^{max} + 1^\circ \text{ (loose)} , \end{aligned} \tag{6.17}$$

  where $\phi_{\pi^-}^{min}$ and $\phi_{\pi^-}^{max}$ are described in Eq. (3.19). The average systematic uncertainty over all bins generated by this source is 1.73%.

Proton ID

- Proton ΔT cut

  Similar to the pion ΔT cut procedure, we tighten or loosen the chosen proton

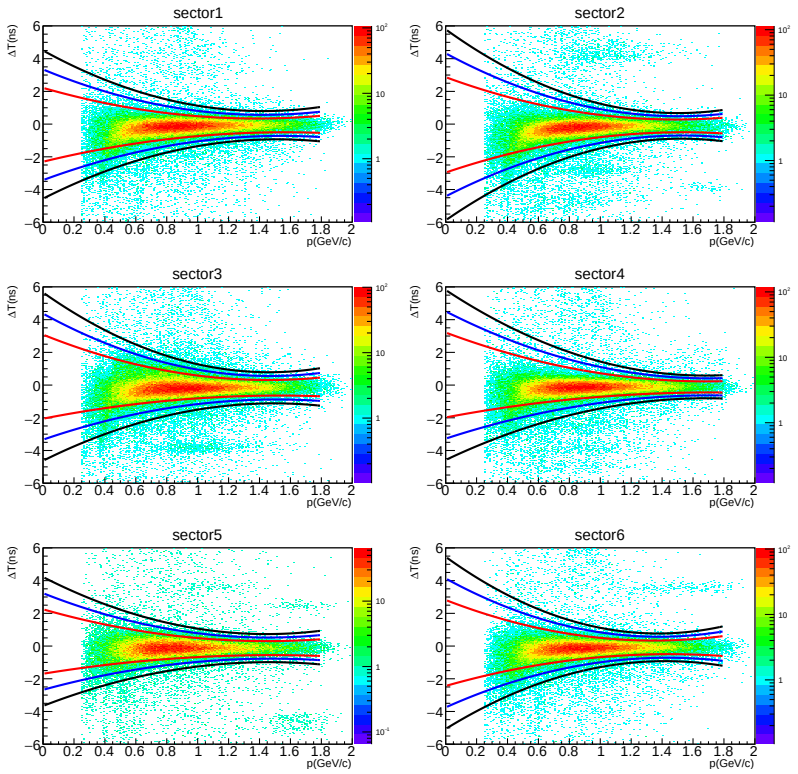

Figure 6.14: The ΔT distribution of protons in six sectors. The black, blue, and red lines represent the 4σ, 3σ, and 2σ cut boundaries, respectively.

ΔT cut described in Eq. (3.13) within

$$\begin{aligned}&(\Delta T_{proton})_{\mu} - 2\sigma < \Delta T_{proton} < (\Delta T_{proton})_{\mu} + 2\sigma \text{ (tight); and} \\ &(\Delta T_{proton})_{\mu} - 4\sigma < \Delta T_{proton} < (\Delta T_{proton})_{\mu} + 4\sigma \text{ (loose),}\end{aligned} \tag{6.18}$$

where μ and σ are the originally chosen cuts parameters. All cuts are shown in Fig. 6.14. The average systematic uncertainty over all bins contributed due to this cut is 1.39%.

- Proton fiducial cut

  We tighten or loosen the chosen proton fiducial cuts presented in Eq. (3.23) within

$$\begin{aligned}&\phi_{proton}^{min} + 1^{\circ} < \phi_{proton} < \phi_{proton}^{max} - 1^{\circ} \text{ (tight) and} \\ &\phi_{proton}^{min} - 1^{\circ} < \phi_{proton} < \phi_{proton}^{max} + 1^{\circ} \text{ (loose) ,}\end{aligned} \tag{6.19}$$

which are shown in Fig. 6.15 as black and magenta lines individually for all sectors. The average systematical error over all bins due to the proton fiducial cut is 2.39%.

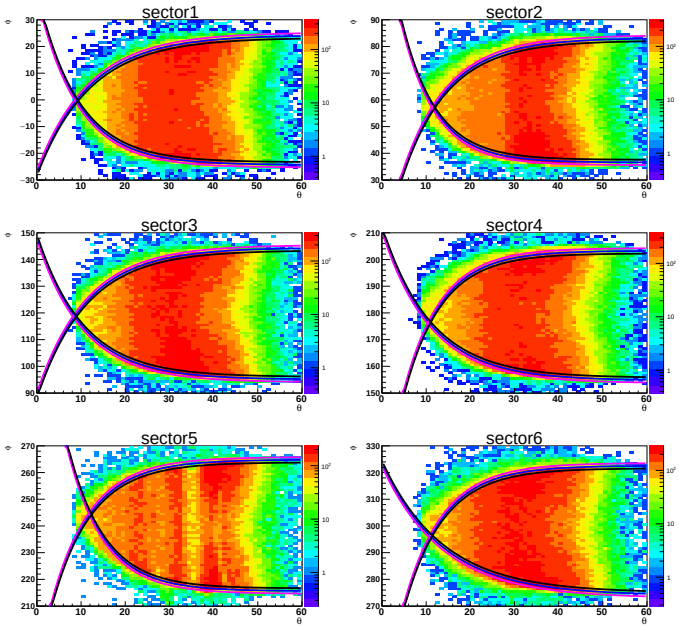

Figure 6.15: (Color online) The ϕ_p versus θ_p distributions for six sectors without proton fiducial cuts. The magenta, blue, and black lines represent loose, chosen, and tight proton fiducial cuts, respectively.

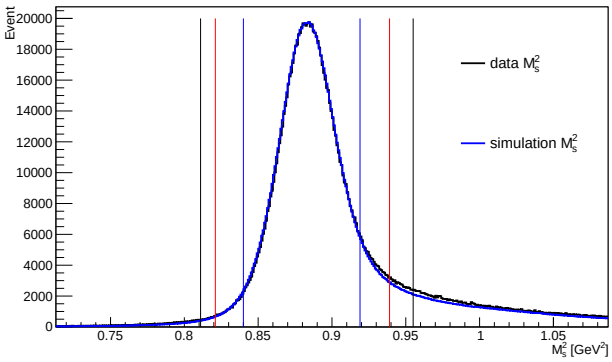

Figure 6.16: (Color online) The spectator missing mass squared M_s^2 distributions for data (black curve) and simulation (blue curve). The black, red, and blue vertical lines represent loose, chosen, and tight M_s^2 cuts, respectively.

Event Selection

- M_s^2 cut

  We varied the chosen M_s^2 cut limits within

$$\begin{aligned} &0.840 \text{ GeV} < M_s^2 < 0.919 \text{ GeV (tight); and} \\ &0.811 \text{ GeV} < M_s^2 < 0.955 \text{ GeV (loose),} \end{aligned} \tag{6.20}$$

  which are all shown in Fig. 6.16. The average systematic uncertainty over all bins due to this cut is 2.29%.

- $|\vec{P}_s|$ cut

  We modified the tight and loose $|\vec{P}_s|$ cuts within

$$\begin{aligned} &0.18 \text{ GeV} < |\vec{P}_s| \text{ (tight); and} \\ &0.22 \text{ GeV} < |\vec{P}_s| \text{ (loose),} \end{aligned} \tag{6.21}$$

  which are all shown with the chosen $|\vec{P}_s|$> 0.2 GeV cut in Fig. 6.17. The $|\vec{P}_s|$ cut is on average responsible for 2.21% of the final systematic uncertainty.

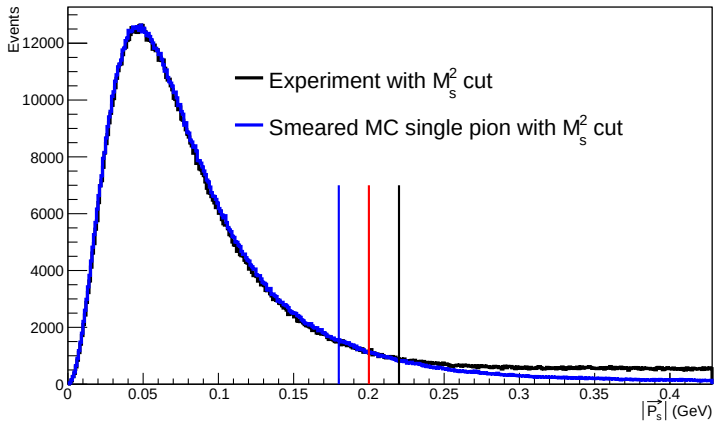

Figure 6.17: (Color online) The spectator missing momentum $|\vec{P}_s|$ distributions for data (black curve) and simulation (blue curve). The black, red, and blue vertical lines represent loose, chosen, and tight $|\vec{P}_s|$ cuts, respectively.

Boost

In the "Boost the kinematic variables" section of Chapter 1, we introduce the boost method. We boost all particle momenta measured in the lab frame into the CM frame, where the net momentum of the final proton and π^- is zero. The boost vector $\vec{\beta}$ is calculated from the final particles (proton and π^-) as

$$\vec{\beta}_f = \frac{\vec{p} + \vec{\pi^-}}{E_p + E_{\pi^-}}, \tag{6.22}$$

where E_p and E_{π^-} are the energies of the proton and π^-, respectively. In addition, $\vec{\beta}$ can be calculated from the initial particles (virtual photon and moving neutron) as

$$\begin{aligned} \vec{\beta}_i &= \frac{\vec{q} + \vec{n}}{\nu + E_n} \text{ with} \\ \vec{n} &= -\vec{p_s} \text{ and} \\ \nu &= E_e - E_{e'}, \end{aligned} \tag{6.23}$$

where ν is the transferred electron energy and E_n the energy of the initial off-shell neutron. Even though finally $\vec{\beta_f}$ is applied in the boost procedure, we want to quantify the difference between boosting with $\vec{\beta_i}$ or $\vec{\beta_f}$ by constructing the initial neutron four momentum by $n^\mu = (-\vec{P_s}, M_n)$ and $E_n = \sqrt{(-\vec{P_s})^2 + (M_n)^2}$, which are introduced in Chapter 1. Since the initial neutron is off-shell, the neutron mass (M_n) is not well defined and can be varied empirically follows

$$M_n = m_n, \tag{6.24}$$

$$M_n = m_n - 2K - 2MeV, \tag{6.25}$$

$$M_n = m_n - K - 1MeV, \tag{6.26}$$

$$M_n = m_n + K + 1MeV, \tag{6.27}$$

$$M_n = m_n + 2K + 2MeV, \tag{6.28}$$

where $K = \frac{(|\vec{P_s}|)^2}{2m_n}$ and m_n is neutron rest mass. Here, the Eq. (6.25) and Eq. (6.28) show two extreme cases of distributing the off-shellness. So we calculate the RMS of

the deviations of these cross sections that are calculated by boosting with β_i from β_f, where β_i is calculated by setting M_n to the different values according to Eqs. (6.24) to (6.28). The systematic uncertainty average over all bins due to different boosts is 2.12%.

Deuteron Potential

We generate the spectator momentum distribution with the CD-Bonn deuteron potential, which allows us to isolate the exclusive quasi-free process and to calculate the kinematical final-state-interaction contribution factor R_{FSI}. There are also other popular deuteron potential models available, as for example the Paris and Hulthen potentials. So we plot the normalized cumulative "spectator" proton momentum distributions based on the deuteron potentials of these three models in Fig. 6.18, and compare the ratios corresponding to the integrals of these distributions from $|\vec{p}|$= 0 GeV/c to $|\vec{p}|$= 0.2 GeV/c and from $|\vec{p}|$= 0 GeV/c to $|\vec{p}|$= 1 GeV/c to get the RMS of the deviations impacted by the CD-Bonn potential from the other two potentials. The systematic uncertainty due to these different deuteron potential models is 3.2% when averaged over all every 4-dimensional bins.

Bin Centering Correction

In the previous Chapter, the MAID2000 model was selected to calculate the bin centering correction factor R_{BC}. In Fig. 4.2a it is shown that the MAID2000 model describes the experimental data better than other MAID versions. However, for the systematic uncertainty study, the factor R_{BC} is calculated with MAID98 and MAID2007 separately and applied to the uncorrected cross sections. The difference between these R_{BC} corrected cross section is then used to quantify the systematic uncertainty due to R_{BC} being calculated from different versions of the MAID model. The average systematic uncertainty found by the deviation of the cross sections cor-

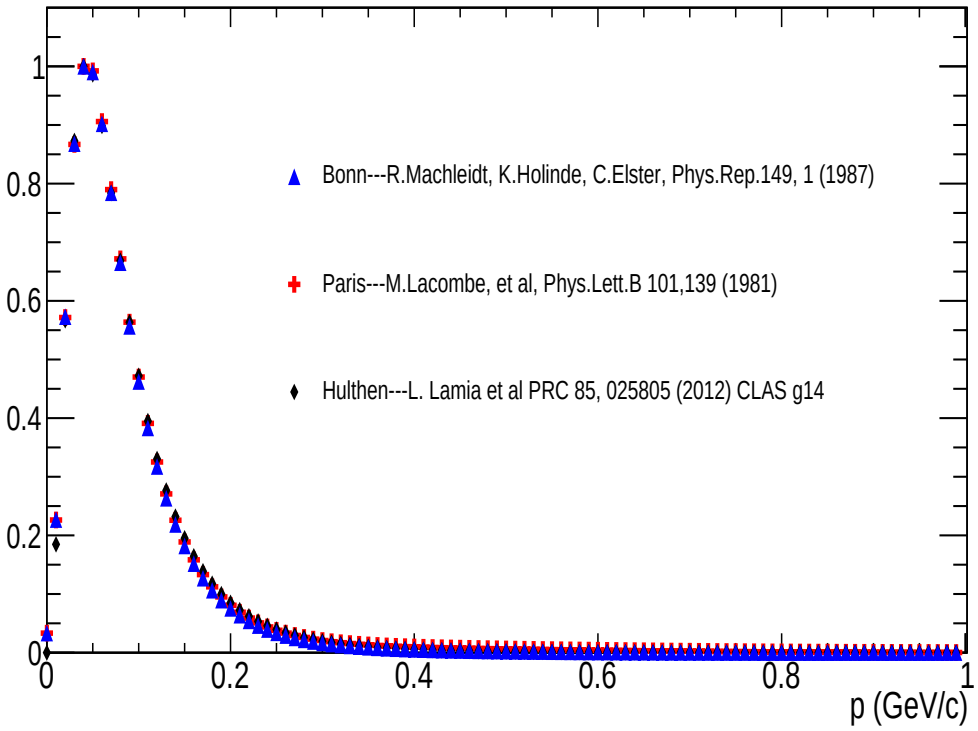

Figure 6.18: The normalized cumulative "spectator" proton momentum distributions from different deuteron potentials. The black, blue, and red points represent the CD-Bonn, Paris, and Hulthen potentials, respectively.

rected by R_{BC} calculated by MAID2000 from these corrected by R_{BC} calculated by MAID98 is 0.55% on average. Even though the MAID2007 model does not describe the experimental data well at all, the R_{BC} calculated by this version would still only contribute 1.39% to the final systematic uncertainty.

Radiative Correction

The cross sections are represented by the variables W_f, Q^2, $\cos\theta^*_{\pi^-}$, and $\phi^*_{\pi^-}$. The radiative correction applied by the Mo and Tsai [48] approach is carried out to eliminate the influence on the Q^2 distribution. The above quasi-free differential cross sections with and without radiative correction are shown in Fig. 6.19 as red points and black squares, respectively. The difference between these two cross sections, ac-

counting for the radiative correction contribution, is on average about 2.0%. The average systematic uncertainty of the radiative correction is set to 1.0% .

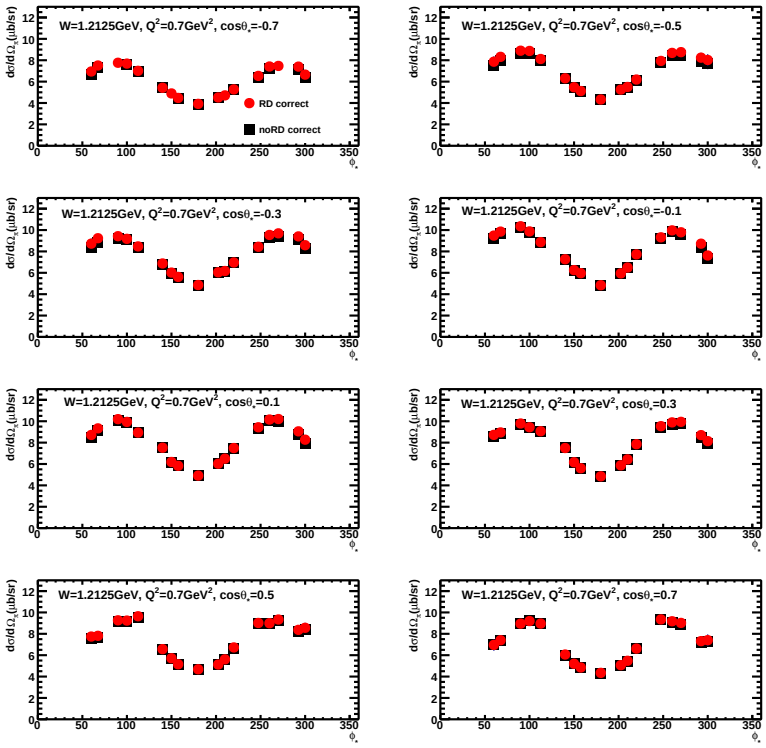

Figure 6.19: The $\phi^*_{\pi^-}$ dependence of the exclusive cross sections with and without radiative correction are marked as red points and black squares, respectively for an example at $W = 1.2125$ GeV and $Q^2 = 0.7$ GeV^2. The individual plots correspond to different $\cos\theta^*_{\pi^-}$ bins.

Normalization

In order to quantify the systematic uncertainty of the overall luminosity, a comparison of the measured inclusive cross sections and the Osipenko's world-data parameterization results is carried out. Since the overall luminosity is the same for all W and Q^2 bins and due to the relatively large uncertainty of the Osipenko's model for different W and Q^2 values, the W and Q^2 weighted average ratios of the Osipenko world-data parameterization results (Eq. (5.13)) and the measured inclusive cross sections (Eq. (5.12)) are shown as the red dot lines in Figs. 6.20 and 6.21 for all six sectors,

separately. It turns out that both kinds of ratios deviate from "1" by no more than 5%. Due to the model dependence of the Osipenko event generator, we pick up the elastic normalization systematic uncertainty of 5% from the CLAS "e1e" data run with hydrogen target [44] for this analysis, which is consistent with the Osipenko driven uncertainty. It is used as the value of the overall normalization uncertainty, and includes target geometry, target density fluctuation, Faraday cup uncertainties.

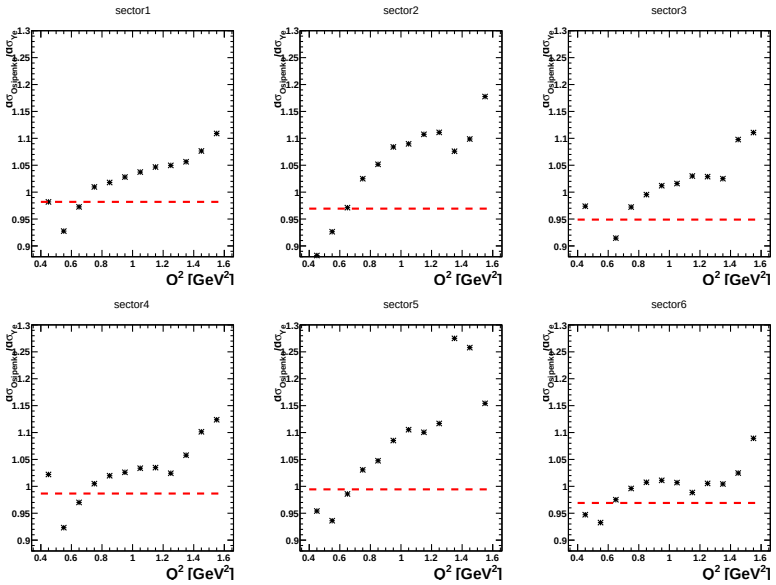

Figure 6.20: The ratios of W integrated inclusive cross sections of $\sigma_{Osipenko}$ over σ_{Ye} marked as black stars are plotted against Q^2. The red dot lines represent the Q^2 averaged ratios.

Summary

Summing over all of the above systematic uncertainty sources listed in the Tab. 6.1, the total average systematic uncertainty is 8.26%. From the above discussion, the total systematic uncertainty can be calculated bin by bin

$$\Delta_{RMS} = \sqrt{\sum_{i}^{9}(\Delta_{cut^i}^{RMS})^2 + (\Delta_{boost}^{RMS})^2 + {\Delta_{potential}}^2 + {\Delta_{R_{BC}}}^2 + {\Delta_{Rad}}^2 + {\Delta_{normalization}}^2}, \tag{6.29}$$

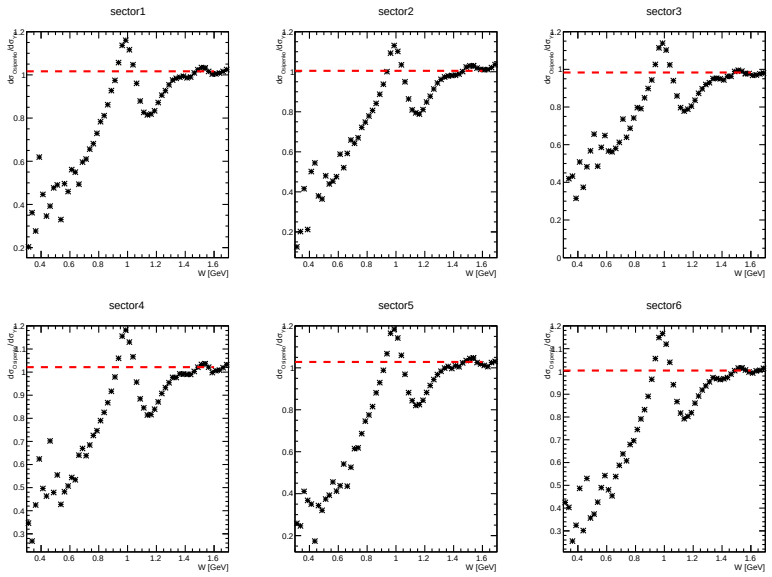

Figure 6.21: The ratios of Q^2 integrated inclusive cross sections of $\sigma_{Osipenko}$ over σ_{Ye} marked as black stars are plotted against W. The red dot lines represent the W averaged ratios.

Table 6.1: Summary of sources of the average systematical uncertainty.

Sources	Uncertainty (%)
Electron θ_{CC} cut	0.78
Electron SF cut	1.26
Electron fiducial cut	2.10
Proton ΔT cut	1.39
Proton fiducial cut	2.39
Pion ΔT cut	1.78
Pion fiducial cut	1.73
M_s^2 cut	2.29
p_s cut	2.21
Boosts	2.12
Potential	3.2
Bin center correction	0.55
Radiative correction	1.0
Normalization	5.0
Total	8.39

where for each variable bin $\Delta_{cut^i}^{RMS}$ corresponds to the RMS of the cross-section deviations of the modified cut (tight or loose) from the chosen cut and Δ_{boost}^{RMS} to the RMS of deviations of the cross sections between different boost vectors $\vec{\beta}_i$ and $\vec{\beta}_f$. $\Delta_{potential}$

corresponds to the deviations of the CD-Bonn potential from other potentials, which is 3.2% for every variable bin, Δ_{Rad} to the radiative correction, and $\Delta_{normalization}$ to the CLAS standard normalization uncertainty, which is 5% for every variable bin. Δ_{RMS} is shown as back bars in the final hadronic differential cross section plots in Figs. 6.2, 6.3, 6.4, 6.5, and 6.6.

Error Propagation

The above systematic uncertainty is calculated for the cross section. In order to have the systematic uncertainty for the structure functions, we apply the same procedure to the $\phi^*_{\pi^-}$ dependent cross section fit $(a + b\cos 2\phi^*_{\pi^-} + c\cos\phi^*_{\pi^-})$ for the chosen cross sections and all other cross-section variations, corresponding to the different cuts, boost, potential, bin centering corrections, and normalizations. Then the RMS of the structure functions is given by Eq. (6.29) bin by bin for three sets of $\phi^*_{\pi^-}$ bins ($\Delta\phi^*_{\pi^-} = 40°$, $\Delta\phi^*_{\pi^-} = 45°$, and $\Delta\phi^*_{\pi^-} = 60°$), respectively. The smallest RMS of the three sets of $\phi^*_{\pi^-}$ bins, the RMS of $\Delta\phi^*_{\pi^-} = 40°$ bins, is set to the final systematic uncertainty of the structure functions, and is shown as black bar for each data point in Fig. 6.12. The average of systematic uncertainties over Q^2 and $cos\theta^*_{\pi^-}$ for the structure functions that are shown in Fig. 6.12 is 11.17% in the $W = 1.2125$ GeV bin.

Chapter 7

Summary and Conclusions

The JLab CLAS "e1e" experiment provides data to extract the differential cross sections of the process $\gamma^* n(p) \to p\pi^-(p)$, which is π^- electroproduction off the neutron in the deuterium, with in the corresponding kinematic coverage $W = 1.1 - 1.9$ GeV and $Q^2 = 0.4 - 1.0$ GeV^2. The experimental data were analyzed in such a way that all stages of this analysis were processed through a series of data consistent tests and cross-checks to provide reliable measured results. The reliability of the absolute normalization was confirmed by the agreement between the measured inclusive cross sections and the available world-data's parameterization results.

The existing $\gamma^* n \to p\pi^-$ event generator was modified to include the spectator (proton) information based on the CD-Bonn potential [28] to simulate the real quasi-free process. With this method, the exclusive quasi-free process is isolated successfully as demonstrated by the comparison of the spectator momentum distribution of simulation with the measured data, and the kinematical final-state-interaction contribution factor R_{FSI} is extracted directly from the experimental data according to the ratio between the exclusive quasi-free and full cross sections. The kinematical final state interaction contributions in π^- electroproduction is on average about $10\% - 20\%$ for the above kinematic coverage. Furthermore, we quantify that the influence of off-shell effects on the final cross section is marginal.

These are the first results for the full exclusive and quasi-free electroproduction cross sections off the bound neutron in the above mentioned kinematic region. These cross sections provide input for a combined analysis of pion electroproduction off the

free proton, the bound proton, and the bound neutron under the same experimental conditions, which is a unique way to extract in the experimentally best possible way information about the off-shell and final-state-interaction effects in deuterium that must be considered in order to extract the free neutron information. These cross sections enrich the database for further development of the reaction theory for exclusive reactions off nucleons bound in deuterium.

Additionally, the associated unpolarized structure functions $\sigma_T + \epsilon\sigma_L$, σ_{TT}, and σ_{TL} have been extracted from the $\phi^*_{\pi^-}$ dependence of the differential cross sections with appropriate systematic uncertainty estimates.

The statistics for the $\gamma^* n(p) \to p\pi^-(p)$ channel is limited due to the short experiment time and the relatively low detector acceptance for the π^- particle. In order to get even better fit results in both the very forward and the very backward polar and azimuthal angles of π^-, particularly in the higher resonance region, it would be valuable to run further deuterium target experiments with the upgraded CLAS12 detector, at Q^2 up to 11 GeV^2. This would also allow us to improve our knowledge of the Q^2 evolution of the transition form factors off the bound nucleon system, and would ultimately grant access to the isospin-dependent structure of baryons.

Bibliography

[1] GSIM, http://nuclear.unh.edu/~maurik/Gsim/.

[2] "e1e" 2 GeV run analysis, https://www.jlab.org/Hall-B/secure/e1/markov/2GeV/newDesign/simulation/simulation.html.

[3] Simutcl, https://userweb.jlab.org/~tianye/cook.

[4] SAID, http://gwdac.phys.gwu.edu/.

[5] Datatcl, https://userweb.jlab.org/~tianye/cook.

[6] CLAS Online BOS Bank Viewer, http://clasweb.jlab.org/bos/browsebos.php.

[7] Golden Run List, https://userweb.jlab.org/~tianye/e1e_analysis/good_file_list.

[8] MAID, http://portal.kph.uni-mainz.de/MAID//.

[9] CVS, https://clasweb.jlab.org/wiki/index.php/Previous_Main_Page.

[10] FFREAD card definitions, http://cnr2.kent.edu/e895/eosg/eosg_manual/node60.html.

[11] genev, https://clasweb.jlab.org/wiki/index.php/CLAS_Offline.

[12] M. Osipenko, personal communications.

[13] A Abdel-Rehim, C Alexandrou, M Constantinou, P Dimopoulos, R Frezzotti, K Hadjiyiannakou, K Jansen, Ch Kallidonis, B Kostrzewa, G Koutsou, et al., *Nucleon and pion structure with lattice qcd simulations at physical value of the pion mass*, Physical Review D **92** (2015), no. 11, 114513.

[14] G. Adams et al., *The CLAS Cherenkov detector*, Nucl. Instrum. Meth. **A465** (2001), 414–427.

[15] M Amarian, Geram Asryan, Kevin Beard, Will Brooks, Volker Burkert, Tom Carstens, Alan Coleman, Raphael Yuri Efremenko, Hovanes Egiyan, Kim Egiyan, et al., *The clas forward electromagnetic calorimeter*, (2001).

[16] R. A. Arndt, W. J. Briscoe, I. I. Strakovsky, and R. L. Workman, *Partial-Wave Analysis of Single-Pion Production Reactions*, AIP Conf. Proc. **904** (2007), 269–275.

[17] CJ Bebek, CN Brown, M Herzlinger, Stephen D Holmes, CA Lichtenstein, FM Pipkin, S Raither, and LK Sisterson, *Determination of the pion form factor up to $Q^2 = 4\ GeV^2$ from single-charged-pion electroproduction*, Physical Review D **13** (1976), no. 1, 25.

[18] CJ Bebek, CN Brown, SD Holmes, RV Kline, FM Pipkin, S Raither, LK Sisterson, A Browman, KM Hanson, D Larson, et al., *Electroproduction of single pions at low ε and a measurement of the pion form factor up to $Q^2 = 10\ GeV^2$*, Physical Review D **17** (1978), no. 7, 1693.

[19] VD Burkert and T-SH Lee, *Electromagnetic meson production in the nucleon resonance region*, International Journal of Modern Physics E **13** (2004), no. 06, 1035–1111.

[20] Simon Capstick and Nathan Isgur, *Baryons in a relativized quark model with chromodynamics*, Physical Review D **34** (1986), no. 9, 2809.

[21] GF Chew, ML Goldberger, FE Low, and Yoichiro Nambu, *Application of dispersion relations to low-energy meson-nucleon scattering*, Physical Review **106** (1957), no. 6, 1337.

[22] JB Cladis, WN Hess, and BJ Moyer, *Nucleon momentum distributions in deuterium and carbon inferred from proton scattering*, Physical Review **87** (1952), no. 3, 425.

[23] R. E. Cutkosky, C. P. Forsyth, R. E. Hendrick, and R. L. Kelly, *Pion Nucleon Partial Wave Amplitudes*, Phys. Rev. **D20** (1979), 2839.

[24] RM Davidson and Nimai C Mukhopadhyay, *Model-independent determination of K-matrix poles and residues in the Δ (1232) region from the multipole data for pion photoproduction*, Physical Review D **42** (1990), no. 1, 20.

[25] D Drechsel, O Hanstein, SS Kamalov, and L Tiator, *A unitary isobar model for pion photo− and electroproduction on the proton up to 1 GeV*, Nuclear Physics A **645** (1999), no. 1, 145–174.

[26] D Drechsel, SS Kamalov, and L Tiator, *Unitary isobar model−MAID2007*, The European Physical Journal A **34** (2007), no. 1, 69–97.

[27] K.S. Egiyan, *Determination of electron energy cut due to the clas ec threshold*, CLAS Note 1999–007, Jefferson Laboratory.

[28] DR Entem and R Machleidt, *Accurate charge-dependent nucleon-nucleon potential at fourth order of chiral perturbation theory*, Physical Review C **68** (2003), no. 4, 041001.

[29] J. Distelbrink M. Eckhausec H. Egiyanc L. Elouadrhirid J. Ficenece M. Guidal E.S. Smitha, T. Carstensa et al., *The time-of-flight system for clas*, Nuclear Instruments and Methods in Physics Research Section A: Accelerators, Spectrometers, Detectors and Associated Equipment **432** (1999), no. 2–3, 265–298.

[30] G. Fedotov, *Personal communications*.

[31] Christian S. Fischer, Stanislav Kubrak, and Richard Williams, *Mass spectra and Regge trajectories of light mesons in the Bethe-Salpeter approach*, Eur. Phys. J. **A50** (2014), 126.

[32] Kubrak Stanislav Williams Richard Fischer, Christian S., *Spectra of heavy mesons in the Bethe-Salpeter approach*, Eur. Phys. J. **A51** (2015), 10.

[33] David Gaskell, Abdellah Ahmidouch, Pawel Ambrozewicz, H Anklin, John Arrington, K Assamagan, Steven Avery, Kevin Bailey, Oliver K Baker, Shelton Beedoe, et al., *Longitudinal Electroproduction of Charged Pions from H_1, H_2, and He_3*, Physical review letters **87** (2001), no. 20, 202301.

[34] R Gilman, M Bernheim, M Brussel, J Cheminaud, J-F Danel, J-P Didelez, M-A Duval, G Fournier, R Frascaria, RJ Holt, et al., *Forward-angle charged-pion electroproduction in the deuteron*, Physical review letters **64** (1990), no. 6, 622.

[35] Rajan Gupta, *Introduction to lattice qcd*, arXiv preprint hep-lat/9807028 (1998).

[36] Stephan Hartmann, *Models and stories in hadron physics*, Models as mediators: Perspectives on natural and social science **52** (1999), 326.

[37] Walter Heupel, Gernot Eichmann, and Christian S. Fischer, *Tetraquark Bound States in a Bethe-Salpeter Approach*, Phys. Lett. **B718** (2012), 545–549.

[38] Popovici Carina Gomez-Rocha Maria Krassnigg Hilger, Thomas and Andreas, *Spectra of heavy quarkonia in a Bethe-Salpeter-equation approach*, Phys. Rev. **D91** (2015), no. 3, 034013.

[39] GM Huber, HP Blok, Cornel Butuceanu, David Gaskell, Tanja Horn, DJ Mack, David Abbott, Konrad Aniol, Heinz Anklin, Christopher Armstrong, et al., *Separated Response Function Ratios in Exclusive, Forward $\pi^{\pm}$ Electroproduction*, Physical review letters **112** (2014), no. 18, 182501.

[40] S. S. Kamalov, D. Drechsel, L. Tiator, and S. N. Yang, *Multipole analysis for pion photoproduction with MAID and dynamical models*, 2nd International Workshop on the Physics of Excited Nucleons (NSTAR 2001) Mainz, Germany, March 7-10, 2001, 2001, pp. 197–202.

[41] SP Klevansky, *The nambu-jona-lasinio model of quantum chromodynamics*, Reviews of Modern Physics **64** (1992), no. 3, 649.

[42] M Lacombe, B Loiseau, R Vinh Mau, J Cote, P Pires, and R De Tourreil, *Parametrization of the deuteron wave function of the paris nn potential*, Physics Letters B **101** (1981), 139–140.

[43] Derek Bruce Leinweber, Anthony William Thomas, Kazuo Tsushima, and Stewart Victor Wright, *Baryon masses from lattice QCD: Beyond the perturbative chiral regime*, Phys. Rev. **D61** (2000), 074502.

[44] Nikolay Markov, *Single π^0 electroproduction off the proton in the resonance region*, Ph.D. thesis, UNIVERSITY OF CONNECTICUT, 2012.

[45] N. Mathur, Y. Chen, S. J. Dong, Terrence Draper, I. Horvath, F. X. Lee, K. F. Liu, and J. B. Zhang, *Roper resonance and S(11)(1535) from lattice QCD*, Phys. Lett. **B605** (2005), 137–143.

[46] Bernhard A Mecking, G Adams, S Ahmad, E Anciant, M Anghinolfi, B Asavapibhop, G Asryan, G Audit, T Auger, H Avakian, et al., *The cebaf large acceptance spectrometer (clas)*, Nuclear Instruments and Methods in Physics Research Section A: Accelerators, Spectrometers, Detectors and Associated Equipment **503** (2003), no. 3, 513–553.

[47] Carman D.S. Mestayer, M.D. et al., *The clas drift chamber system*, Nuclear Instruments and Methods in Physics Research A **449** (2000), 81–111.

[48] Luke W Mo and Yung-Su Tsai, *Radiative Corrections to Elastic and Inelastic ep and up Scattering*, Reviews of Modern Physics **41** (1969), no. 1, 205.

[49] JV Morris, DC Darvill, M Davenport, F Foster, G Gughes, J Wright, J Allison, B Dickinson, S Hill, M Ibbotson, et al., *Forward electroproduction of charged pions from deuterons at* $Q^2 = 1.0(GeV\backslash c)^2$, Physics Letters B **86** (1979), no. 2, 211–214.

[50] T Muta, *Foundations of quantum chromodynamics; an introduction to perturbative methods in gauge theories*, World Scientific, 1987.

[51] R. Niyazov and L. B. Weinstein, *Fiducial Cut For Positive Hadrons in CLAS/E2 data at 4.4 GeV*, CLAS Note 2001–013, Jefferson Laboratory.

[52] KA Olive, K Agashe, C Amsler, M Antonelli, J-F Arguin, DM Asner, H Baer, HR Band, RM Barnett, T Basaglia, et al., *Review of particle physics particle data group*, Chinese Physics C **38** (2014), no. EPFL-REVIEW-203959, 090001.

[53] M. Osipenko, *Matching between the electron candidate track and the cherenkov counter hit*, CLAS Note 2004–020, Jefferson Laboratory.

[54] M Osipenko, G Ricco, S Simula, M Battaglieri, M Ripani, G Adams, P Ambrozewicz, M Anghinolfi, B Asavapibhop, G Asryan, et al., *Measurement of the deuteron structure function f 2 in the resonance region and evaluation of its moments*, Physical Review C **73** (2006), no. 4, 045205.

[55] K. Park, *Kinematics corrections for clas*, CLAS Note 2003–012, Jefferson Laboratory.

[56] Klaus; Scholz-Christoph; Zetsche Rrank Povh, Bogdan; Rith, *Particles and nuclei; an introduction to the physical concepts*, Springer, 2008.

[57] M. Procura, B. U. Musch, T. Wollenweber, T. R. Hemmert, and W. Weise, *Nucleon mass: From lattice QCD to the chiral limit*, Phys. Rev. **D73** (2006), 114510.

[58] Alan Steven Raskin and T William Donnelly, *Polarization in coincidence electron scattering from nuclei*, Annals of Physics **191** (1989), no. 1, 78–142.

[59] Bogdan Povh Klaus Rith and Christoph Scholz Frank Zetsche, *Particles and nuclei*.

[60] Craig D Roberts and Anthony G Williams, *Dyson-schwinger equations and their application to hadronic physics*, Progress in Particle and Nuclear Physics **33** (1994), 477–575.

[61] Helios Sanchis-Alepuz, Christian S Fischer, Christian Kellermann, and Lorenz von Smekal, *Glueballs from the bethe-salpeter equation*, Physical Review D **92** (2015), no. 3, 034001.

[62] Helios Sanchis-Alepuz and Richard Williams, *Hadronic observables from dyson–schwinger and bethe–salpeter equations*, Journal of Physics: Conference Series, vol. 631, IOP Publishing, 2015, p. 012064.

[63] Jorge Segovia, Chen Chen, Ian C. Cloët, Craig D. Roberts, Sebastian M. Schmidt, and Shaolong Wan, *Elastic and Transition Form Factors of the* $\Delta(1232)$, Few Body Syst. **55** (2014), 1–33.

[64] J Wright, DC Darvill, M Davenport, F Foster, G Hughes, JV Morris, J Allison, B Dickinson, S Hill, M Ibbotson, et al., *Electroproduction of single charged pions from deuterons at* $Q^2 \sim 0.5(GeV\backslash c)^2$, Nuclear Physics B **181** (1981), no. 3, 403–420.

Appendix A

Parameter Tables

Table A.1: Parameters of pion θ versus p cut functions.

Sector	Position	C_0	C_1	C_2	C_3	C_4
1	upper	96.090	8.000	0.472	0.250	0.117
	lower	86.090	8.000	0.472	0.250	0.117
2	upper	38.152	3.699×10^{-5}	5.408×10^{-6}	1.812×10^{-7}	
	lower	33.652	3.699×10^{-5}	5.408×10^{-6}	1.812×10^{-7}	
3	upper	116.152	3.699×10^{-5}	5.408×10^{-6}	0.1	1.812×10^{-7}
	lower	107.152	3.699×10^{-5}	5.408×10^{-6}	0.08	1.812×10^{-7}
4	upper	113.152	3.699×10^{-5}	5.408×10^{-6}	0.15	1.812×10^{-7}
5-1	upper	118.152	6.699×10^{-5}	5.408×10^{-6}	0.2	1.812×10^{-7}
5-2	upper	108.152	3.699×10^{-5}	5.408×10^{-6}	0.2	1.812×10^{-7}
	lower	96.152	3.699×10^{-5}	5.408×10^{-6}	0.03	1.812×10^{-7}
5-3	upper	39.652	3.699×10^{-5}	5.408×10^{-6}	0.01	1.812×10^{-7}
	lower	35.652	3.699×10^{-5}	5.408×10^{-6}	0.01	1.812×10^{-7}
6	upper	106.152	3.699×10^{-5}	5.408×10^{-6}	0.15	1.812×10^{-7}

Table A.2: Parameters of proton θ versus p cut functions.

Sector	Position	C_0	C_1	C_2	C_3	C_4
2	upper	26.509	-116.557	175.167	-64.472	
	lower	26.509	-116.557	175.167	-64.572	
5-1	upper	88.042	-0.321	0.070	-46.934	
	lower	87.094	-0.371	0.065	-50.990	
5-2	upper	31.248	-135.817	198.038	-65.168	0.045
	lower	31.248	-135.817	198.038	-69.468	-0.010

Table A.3: ΔT shift parameters.

Sector	Counter	Δt_1 (ns)	Δt_2 (ns)	Δt_3 (ns)	Δt_4 (ns)	Δt_5 (ns)
1	25	0.34				
	36	-0.36				
	43	-0.04				
	41	3.63	0.18	-2.96		
	42	-0.08	-2.14			
	45	4.72	3.16	0.32	-3.04	
	46	-0.03	-1.02	-2.15	-5.82	
	47	5.97	5.00	0.22		
2	24	1.18				
	22	0.09				
	27	-0.46				
	29	-0.37				
	36	-0.46				
	37	0.25				
	40	2.90	-0.10	-2.74	-7.17	
	41	8.40	7.34	4.10	3.05	-1.80
	42	4.78	0.45			
	43	10.81	8.22	6.94		
	44	6.69	3.93			
	45	5.30	0.25			
	46	8.05	0.85			
	47	0.11	-1.66			
3	11	0.34				
	23	0.21				
	24	-0.33				
	25	3.42				
	30	-0.16				
	35	-0.40				
	38	-0.53				
	36	-0.18				
	40	-0.10	-3.95			
	41	-0.05	-0.86			
	42	-2.03	-5.50			
	43	-0.50	-3.60			
	44	-8.19	-10.52			
	46	-0.60	-1.44	-3.35		
	47	4.62	2.00	-0.61		

Table A.4: ΔT shift parameters continued.

Sector	Counter	Δt_1 (ns)	Δt_2 (ns)	Δt_3 (ns)	Δt_4 (ns)
4	22	0.08			
	23	-0.35			
	25	-0.37			
	26	-0.27			
	27	-0.48			
	37	-0.42			
	38	-0.53			
	39	4.24			
	40	-0.21			
	41	0.59			
	42	2.95	0.04		
	43	2.99	1.29	-0.99	
	44	-0.12			
	45	0.07			
	46	1.19	0.17		
	47	0.04			
5	22	0.14			
	24	0.01			
	25	0.08			
	37	0.43			
	40	4.65	1.44		
	41	-0.44			
	42	4.23	1.17	0.28	-1.86
	43	2.37	0.46		
	44	0.76	-0.73		
	45	0.08			
	46	-2.11			
	47	-2.06	-4.10		
6	25	-2.11			
	31	1.55			
	40	3.90	0.05		
	43	-1.77			
	44	1.37	-0.06		
	45	3.69	0.10		
	47	5.26	2.63	0.85	

Table A.5: Parameters of the proton momentum correction function.

parameter	value
C_0	-2.01369×10^{-2}
C_1	2.36456×10^{-4}
C_2	2.18450×10^{-6}
C_3	1.29756×10^{-2}
C_4	-2.00838×10^{-4}
C_5	1.88744×10^{-6}
C_6	1.03155×10^{-2}
C_7	-7.19808×10^{-5}
C_8	6.11292×10^{-7}

Table A.6: Parameters of pion θ versus ϕ cut functions.

	parameter	P_0	P_1	P_2
data	C_{0max}	25.1028	-0.248504	-0.470204
	C_{0min}	-25.1039	0.249551	0.470333
	C_2	20.4540	2.52675	3.34473
	C_1	0.255487		
simulation	C_{0max}	27.0012	-0.741629	-0.723387
	C_{0min}	-27.5001	0.777486	0.734897
	C_2	14.1899	0.999445	2.84491
	C_1	0.135487		

Table A.7: Parameters of proton θ versus ϕ cut functions.

sector	function	P_0	P_1	P_2
1	ϕ_{max}	24.2559	0.0840516	-9.00173
	ϕ_{min}	-24.3303	0.1096713	-8.85532
2	ϕ_{max}	83.1846	0.0967659	0.376712
	ϕ_{min}	36.5613	0.129967	-7.20855
3	ϕ_{max}	144.4382	0.0895825	10.7034
	ϕ_{min}	95.0490	0.0955602	6.03828
4	ϕ_{max}	203.271	0.11877	6.32992
	ϕ_{min}	155.694	0.090633	11.05086
5	ϕ_{max}	264.817	0.112822	10.7241
	ϕ_{min}	215.618	0.122742	4.34678
6	ϕ_{max}	323.471	0.113954	10.9227
	ϕ_{min}	275.005	0.0729742	24.2907